



DISTRIBUTION STATEMENT A

Approved for public release
Distribution Unlimited

**THEORETICAL MODELING OF LINEAR
ABSORPTION COEFFICIENTS IN Si/Si_{1-x}Ge_x
MULTIPLE QUANTUM WELL PHOTODETECTORS**

THESIS

Kevin D. Greene, Captain, USAF

AFIT/ENP/GAP/96D-06

19970519 026

[DTIC QUALITY INSPECTED 3]

DEPARTMENT OF THE AIR FORCE
AIR UNIVERSITY
AIR FORCE INSTITUTE OF TECHNOLOGY

Wright-Patterson Air Force Base, Ohio

accompanying .zip file contains a number of documents which should be printed in following order:

leaf.doc
lepg.doc
pter1.doc
pter2.doc
pter3.doc
pter4.doc
endx.doc
lio.doc
a.doc

files needed to decompress the .zip file are included as well.

AFIT/ENP/GAP/96D-06

THEORETICAL MODELING OF LINEAR ABSORPTION COEFFICIENTS IN

Si/Si_{1-x}Ge_x MULTIPLE QUANTUM WELL PHOTODETECTORS

THESIS

Kevin D. Greene, Captain, USAF

AFIT/ENP/GAP/96D

DTIC QUALITY INSPECTED 3

Approved for public release; distribution unlimited

AFIT/ENP/GAP/96D-06

THEORETICAL MODELING OF LINEAR ABSORPTION COEFFICIENTS IN
Si/Si_{1-x}Ge_x MULTIPLE QUANTUM WELL PHOTODETECTORS

THESIS

Presented to the Faculty of the Graduate School of Engineering
Air Education and Training Command
In Partial Fulfillment of the Requirements for the Degree of
Master of Science in Applied Physics

Kevin D. Greene, B.S.

Captain, USAF

October 1996

Approved for public release; distribution unlimited

AFIT/ENP/GAP/96D-06

THEORETICAL MODELING OF LINEAR ABSORPTION COEFFICIENTS IN
Si/Si_{1-x}Ge_x MULTIPLE QUANTUM WELL PHOTODETECTORS

Kevin D. Greene, B.S.
Captain, USAF

Approved:



David Weeks
Chairman, Advisory Committee

19 Nov 96



Robert Hengehold
Member, Advisory Committee

19 Nov 96



Frank Szmulowicz
Member, Advisory Committee

19 Nov. 96

Acknowledgments

The most important participant in this thesis is my Lord and Savior, Jesus Christ. Without His strength, guidance, and patience I would be unable to accomplish anything of substance. The Lord strengthened me when I doubted myself, provided solutions when I could see none, and provided me with a purpose for my life and studies. In a real sense, this paper should bear His name as co-author, and He again deserves my thanks.

I wish to thank my family: Lisa, Kristin and Kennan. Their patience with me throughout the last year has been outstanding. Lisa has not only been patient with my absences, but helped to assemble and edit the thesis.

My advisor, Dr. David Weeks not only kept me on track throughout this project, but encouraged me whenever I expressed doubt. Dr. Weeks answered my many questions with patience and good cheer.

Finally, I would like to thank Capt. Rob Pope for his assistance, encouragement, advice, and friendship. Without him this project would have been much less interesting and I would have spent much more time expending energy exploring dead ends.

Table of Contents

	Page
Approval Page	ii
Acknowledgments	iii
List of Figures	vi
List of Tables	xi
List of Symbols	xii
Abstract	xiv
 I. INTRODUCTION	 I-1
A. Background	I-2
1. Properties of Silicon and Germanium	I-2
2. Silicon and Germanium Alloys	I-5
B. Infrared (IR) Detector Technology	I-6
1. Intrinsic Photodetectors	I-8
2. Extrinsic Photodetectors	I-8
3. Free Carrier Photodetectors	I-10
a. Internal Photo-emission (IP) Photodetectors	I-10
b. Heterojunction Internal Photoemission Photodetectors	I-10
4. Multiple Quantum Well Photodetectors	I-12
C. SiGe MQW Device Developments	I-15
1. Experimental Data	I-15
2. History of Theoretical Developments	I-16
 II. THEORY DEVELOPMENT	 II-1
A. Introduction and Organization	II-1
B. Development of the Hamiltonian in the Bulk Semiconductor	II-1
1. General Form of the Bulk Hamiltonian	II-10
2. Coordinate Systems and Relationship to the Crystal Lattice	II-12
3. Spin-Orbit Interaction	II-13
4. Strain Induced Perturbation	II-15
C. Envelope Function Approximation and Boundary Value Problem	II-20
1. Overview of the Envelope Function Approximation	II-20
2. Numerical Difficulties in the Determination of the MQW	

Band Structure.....	II-24
D. Calculation of Linear Absorption Coefficients	II-29
1. Subband Occupation Levels.....	II-29
2. Determination of the Density of States (DOS).....	II-31
3. Calculation of Inter-subband Momentum Matrix Elements	II-35
4. Bound to Bound Absorption Coefficients.....	II-38
5. Exchange Interaction.....	II-44
III. RESULTS AND DISCUSSION	III-1
A. Calculation of Momentum Matrix Elements.....	III-1
B. Linear Absorption Coefficients Derived via the Delta Function Approximation	III-8
C. Linear Absorption Coefficients Derived via the Lorentzian Approximation	III-14
D. Recommendations and Summary.....	III-25
APPENDIX A. Derivation of Finite Depth Quantum Well Energy Levels..	A-1
APPENDIX B. Coordinate Systems.....	B-1
BIBLIOGRAPHY	BIB-1
VITA	VITA-1

List of Figures

Figure	Page
I-1. Direct Bandgap Transition	I-3
I-2. Indirect Bandgap Transition	I-4
I-3. Tetrahedral Bonding Structure	I-4
I-4. Diamond Lattice Structure	I-5
I-5. Spectral D* for Some Commercially Available Materials.....	I-9
I-6 Structure of the IP or HIP Photodetector.....	I-11
I-7 Band Structure of the IP Photodetector and the HIP Photodetector.....	I-11
I-8 Typical MQW Structure with Band Structure.....	I-13
I-9 Absorbance Spectra for Si[110]/Si _{0.70} Ge _{0.30} , 30 Å Wide Well MQW Structure with 15 Periods.....	I-16
II-1. Energy bands formed from the eigenvalues of $H=H'$ for Si[110], x=0.30.	II-18
II-2. Energy bands formed from the eigenvalues of $H=H'+H_{so}$ for Si[110], x=0.30.	II-19
II-3. Energy bands formed from the eigenvalues of $H=H'+H_{so}+H_{strain}$ for Si[110], x=0.30.....	II-19
II-4. Dispersion Relations for the [110] substrate orientation, 30 Å well width, and 30% Ge composition ($k_{ }$ is in the k_x direction).....	II-21
II-5. Heavy Hole w_i 's vs $k_{ }$ for the [110] substrate orientation, 30 Å well width, and 30% Ge composition ($k_{ }$ is in the k_x direction).	II-23
II-6. Heavy Hole bandweights vs $k_{ }$ for the [110] substrate orientation, 30 Å well width, and 30% Ge composition ($k_{ }$ is in the k_x direction).	II-23

II-7.	Band structure of a 30 Å / 30% Ge quantum well structure in a direction 45° between k_x and k_y showing an enlarged instability region.....	II-25
II-8.	Band structure of a 30 Å / 30% Ge quantum well structure in the k_x direction showing instability region.	II-26
II-9.	Bandweights w_i for the HH1 band of the 30 Å / 30% Ge quantum well in the k_x direction, showing the smoothness of the bandweights outside of the instability region identified in figure II-7.	II-27
II-10.	Bandweights w_i for the LH1 band of the 30 Å / 30% Ge quantum well for 45° between the k_x and k_y directions, showing the instability in the band weights throughout the range of $k_{ }$	II-27
II-11.	Smoothed plot of the band structure of a 30 Å / 30% Ge quantum well structure in the k_x direction.....	II-29
II-12.	Fermi-Dirac distribution function for a Fermi energy of -0.12 eV, at temperatures of 1 K, 77 K, and 300 K.....	II-31
II-13	Density of states vs energy, [110] substrate orientation, $L = 30$ Å , 30% Ge.	II-33
II-14	Integrated density of states for [110] substrate, $L=30$ Å , 30% Ge composition.	II-34
II-15	P_x momentum matrix elements for transitions from the HH1 Band to higher levels for the Si[110]/ 30 Å / 30% Ge case.....	II-38
II-16	Linear absorption coefficient vs energy (eV) for pure z polarization. No magnification of smaller peaks is performed.....	II-41
II-17	Linear absorption coefficient vs energy produced by integrating a Lorentzian fit to all possible transitions. Absorption coefficient is for normally polarized light. Exchange interaction is included.	II-43
III-1.	P_x^2 vs $k_{ }$ for transitions from the HH1 band.....	III-3
III-2.	P_x^2 vs $k_{ }$ for transitions from the LH1 band.	III-4

III-3.	P_x^2 vs $k_{ }$ for transitions from the HH2 band.....	III-4
III-4.	P_y^2 vs $k_{ }$ for transitions from the HH1 band.....	III-5
III-5.	P_y^2 vs $k_{ }$ for transitions from the LH1 band.	III-5
III-6.	P_y^2 vs $k_{ }$ for transitions from the HH2 band.....	III-6
III-7.	P_z^2 vs $k_{ }$ for transitions from the HH1 band.....	III-6
III-8.	P_z^2 vs $k_{ }$ for transitions from the LH1 band.	III-7
III-9.	P_z^2 vs $k_{ }$ for transitions from the HH2 band.....	III-7
III-10.	Absorption coefficient peaks for \hat{z} polarization component, present in non-normally incident radiation. In practice, this spectrum will also be accompanied by \hat{x} or \hat{y} contributions.	III-9
III-11.	Absorption coefficient peaks for the \hat{z} polarization component, present in non-normally incident radiation, scale expanded to show more details of the lower magnitude peaks.....	III-10
III-12.	Absorption coefficient peaks for the \hat{x} component of incident radiation.....	III-10
III-13.	Absorption coefficient peaks for the \hat{x} component of incident radiation, scale expanded to show details of lower magnitude peaks.....	III-11
III-14.	Absorption coefficient peaks for the \hat{y} component of incident radiation.....	III-11
III-15.	Absorption coefficient peaks for the \hat{y} component of incident radiation, scale expanded to show detail of lower magnitude peaks.....	III-12
III-16.	Absorption coefficient ($\alpha(E)$) for normal incidence compared with experimental data.	III-13
III-17.	Absorption coefficient ($\alpha(E)$) for normal incidence compared with experimental data.	III-13

III-18.	Energy band differences between HH1 and higher lying bands. Note that locations where $\Delta E = \hbar\omega$ are not unique in many of the bands so that transitions may occur for several values of $k_{ }$	III-15
III-19.	Lorentzian function for a value of $\hbar\omega=.04$ eV for the HH1-LH1 band transition shown in figure III-24.	III-16
III-20.	Linear absorption coefficient for pure x polarization.	III-17
III-21.	Linear absorption coefficient for pure y polarization.	III-17
III-22.	Linear absorption coefficient for pure z polarization.	III-18
III-23.	Linear absorption coefficient for parallel incident radiation.	III-19
III-24.	Linear absorption coefficient for normally incident radiation.	III-20
III-25.	Linear absorption coefficient for parallel incident radiation, absorption coefficient scale applies only to the experimental absorptance values.	III-20
III-26.	Linear absorption coefficient for normally incident radiation, absorption coefficient scale applies only to the experimental absorptance values.	III-21
III-27.	Calculated absorption coefficients and experimental absorption data versus wavelength. Values are shown for parallel incident radiation.	III-22
III-28.	Calculated absorption coefficients and experimental absorption data versus wavelength. Values are shown for normally incident radiation.	III-23
A-1.	Potential well coordinate system and geometry.	A-1
A-2.	Determinant of M for a square well of depth 5 au and width of 3 au.	A-5
A-3.	Determinant of M for the unsimplified and simplified cases.	A-5
A-4.	Det(M) for the case of a square well of depth 2 au and width of 1 au.	A-7

A-5.	Bound State wave functions for a well of depth 2 au and width of 2 au.	A-8
B-1.	MQW Coordinate Axes.	B-1
B-2.	Normal Incidence.	B-2
B-3.	Parallel Incidence.	B-2

List of Tables

Table	Page
I-1. Physical Properties of Si and Ge	I-5
II-1 Euler Angles (θ and ϕ) for Coordinate Rotation.....	II-12
III-1. Band Transitions Allowed for the Fermi Levels Considered.....	III-2

List of Symbols

\AA	Angstrom (10^{-10} m)
λ	Wavelength
Γ	Lorentzian Line Broadening Parameter
ΔE	Energy Difference
$\alpha(\omega)$	Absorption Coefficient (function of wavelength)
ϵ_f	Fermi Energy
γ_i	Luttinger Coefficients
η	Quantum Efficiency
μm	microns (10^{-6} m)
AFIT	Air Force Institute of Technology
au	Atomic Units
c.p.	Cyclic Permutation
D^*	Detectivity
D_i	Deformation Potential
E	Energy
EFA	Envelope Function Approximation
eV	Electron Volts
$f(\epsilon)$	Fermi-Dirac Distribution Function
Ge	Germanium
HH	Heavy Hole
HIP	Heterojunction Internal Photoemission

H_{so}	Spin Orbit Hamiltonian
H_{strain}	Strain Hamiltonian
H_{tot}	Total Hamiltonian
I_6	Identity Matrix
IP	Internal Photoemission
IR	Infra-Red
K	Kelvin
k	wave vector
$k_{ }$	wave vector parallel to well plane
L	Well Width
LH	Light Hole
LK	Luttinger-Kohn
MBE	Molecular Beam Epitaxy
MQW	Multiple Quantum Well
p	Momentum
QW	Quantum Well
QWIP	Quantum Well Infrared Photodetector
Si	Silicon
SiGe	Silicon Germanium
SO	Split-Off Hole
$T(k)$	Boost Operator
$w_{N,v}$	EFA Band Weight

Abstract

Si/Si_{1-x}Ge_x MQW Infrared Photodetectors offer the promise of normal incidence photodetection tunable over the range of 3-12 μm wavelength range at temperatures above 40 K. This system is attractive because the Si_{1-x}Ge_x offers greater compatibility with existing Si based signal processing circuitry.

Band structures, momentum matrix elements and linear absorption coefficients are computed using a Luttinger-Kohn **k•p** analysis for Si/ Si_{1-x}Ge_x quantum wells grown in the [110] direction. The absorption coefficient as a function of energy and wavelength is calculated by two methods: a delta function fit to intersubband transitions, and a Lorentzian fit to intersubband transitions. Calculations were performed for parallel as well as normally incident radiation and the resulting absorption spectra are in good agreement with experimental observations.

THEORETICAL MODELING OF LINEAR ABSORPTION COEFFICIENTS IN Si/Si_{1-x}Ge_x MULTIPLE QUANTUM WELL PHOTODETECTORS

Chapter I. Introduction

The Si[110]/Si_{1-x}Ge_x multiple quantum well (MQW) system is of interest because it offers the promise of normal incidence radiation detection in the 8-12 μm range at operating temperatures well above the 20-30 K operating temperatures of existing photon (quantum) detectors. Normal incidence absorption and photoresponse will allow simpler detector design without the requirement for complicated input couplings. This system has not been previously examined due to the difficulty of reliably fabricating the strained-layer SiGe alloys comprising the system. In recent years methods of fabricating these structures via molecular beam epitaxy and chemical vapor deposition have been developed, making theoretical and experimental studies of the system's characteristics both timely and possible¹.

This project focuses on modeling a Si[110]/Si_{1-x}Ge_x MQW system to develop inter-subband absorption coefficients. This is achieved through use of $\vec{k} \cdot \vec{p}$ theory and the envelope function approximation (EFA) approach to model the bound state eigenfunctions. Eigenfunctions in the bulk semiconductor are obtained through the application of $\vec{k} \cdot \vec{p}$ theory, which also provides the approximate band structure near the

Brillouin zone center. The EFA eigenfunctions are the eigenfunctions of the bound states of the quantum well and are developed by applying boundary conditions at the heterojunction interface to yield linear combinations of the bulk eigenfunctions. The boundary conditions specify the continuity of the eigenfunctions and their derivatives at the heterojunction between barrier and well regions. The momentum matrix elements for transitions between bound states are then computed using the EFA eigenfunctions and used to determine the strengths of intersubband transitions, which are proportional to the absorption coefficients for a given wavelength and polarization of the incident radiation^{2,3}. The development of absorption coefficients for Si[110]/Si_{1-x}Ge_x is not found in the literature and is an original contribution.

Section A. Background

Properties of Silicon and Germanium.

Silicon and germanium are both familiar and well characterized materials that have been used in solid state devices for many years. Due to their familiarity, their physical characteristics have been accurately measured and are tabulated in many sources⁴. Unfortunately, neither silicon nor germanium are good elements for detection purposes. One of the main reasons for this is that they are indirect bandgap semiconductors, so the minima of the conduction band is not located at the same spot in k space as the maxima of the valence bands⁴. This means that low energy transitions must be phonon assisted in order to occur, thus the probability of such transitions occurring is lowered. This is shown schematically in figures I-1 and I-2⁵.

Physically, both Si and Ge belong to the group IVb on the periodic table, possessing partially filled 3p and 4p shells (respectively) with 2 electrons⁶. The four empty spots in the p shell can be thought of as causing these elements to form covalent tetrahedral bonds, shown in figure I-3. The tetrahedral bonding arrangements of Ge and Si lead them to form lattices of the diamond structure (shown in figure I-4⁷), with lattice cells of dimensions 5.42 Å for Si and 5.62 Å for Ge⁸. Table I-1 lists some physical constants for Si and Ge.

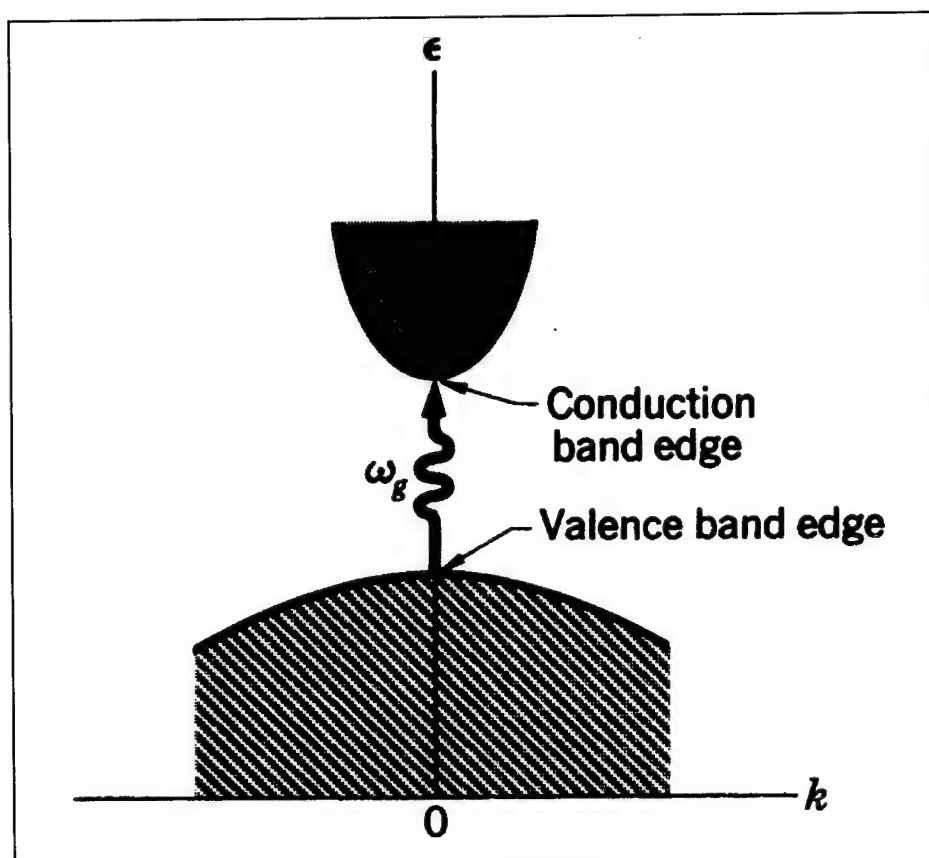


Figure I-1. Direct bandgap transition. (After Ref. 5)

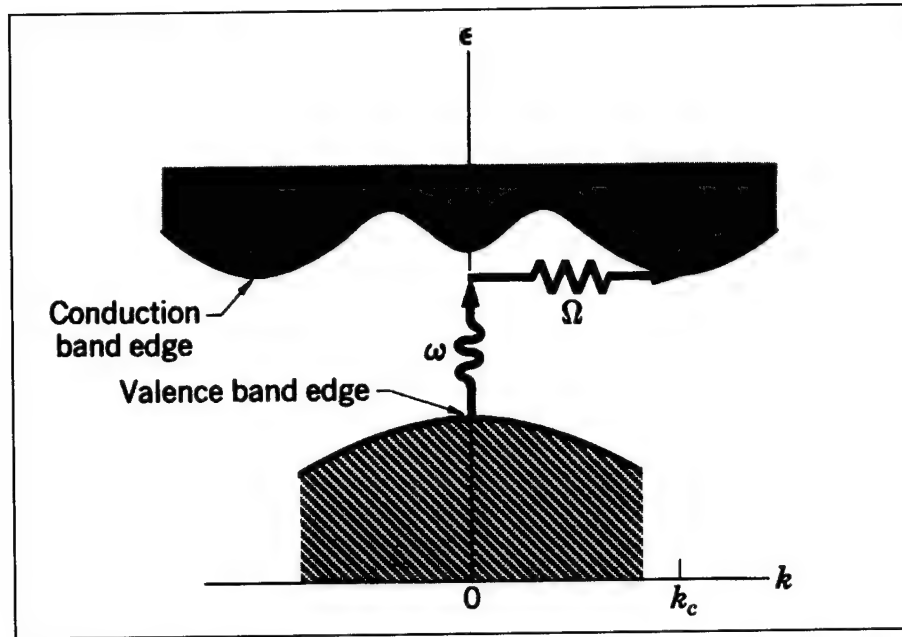


Figure I-2. Indirect band gap transition. Photon transitions are labeled by ω and phonon transitions by Ω . The phonon transition shown is purely schematic in nature, as the horizontal ($\Delta\epsilon = 0$) transition is not realistic. (After Ref. 5)

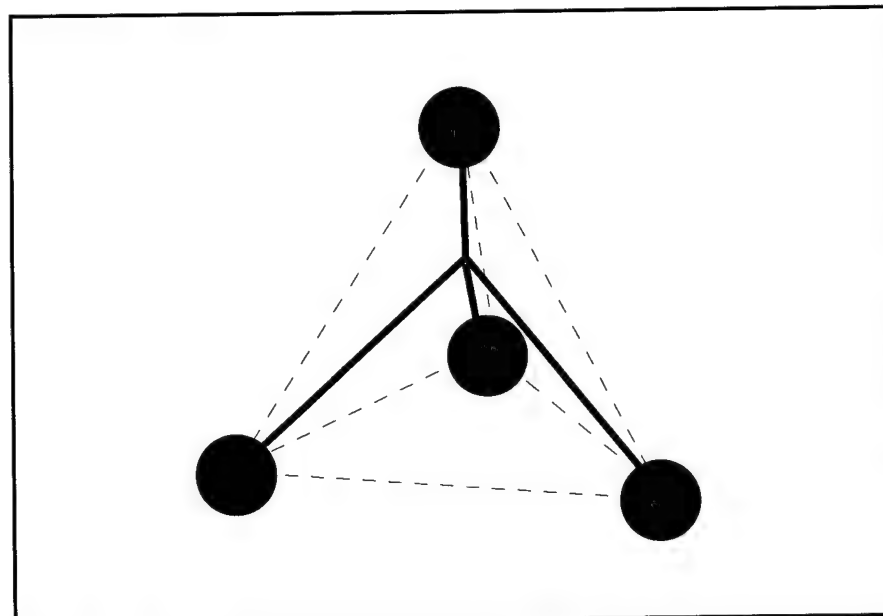


Figure I-3. Tetrahedral bonding structure.

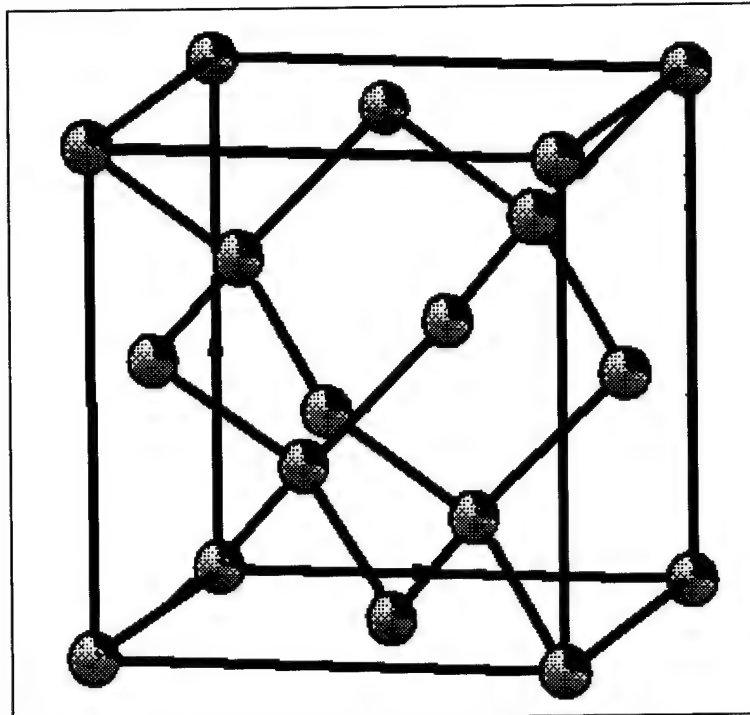


Figure I-4. Diamond lattice structure (After Ref. 7)

Table I-1. Physical Properties of Si and Ge^{8,9}

Material	Structure	Lattice Cell Edge	Mobility (electrons)	Mobility (holes)	Intrinsic Bandgap
Silicon	Diamond	5.42 Å	1,350*	480*	1.11 ⁺
Germanium	Diamond	5.62 Å	3,900*	1,900*	.67 ⁺

* Mobilities at 300K, in cm²/volt-sec

⁺ Resistivity at 300K, in ohm-cm

Silicon and Germanium Alloys.

The bulk Si_xGe_{1-x} (the variable x represents the percentage Ge composition) system has been studied since the 1950s by various groups¹⁰. The properties of the bulk material have been characterized to include the absorption properties, hydrostatic deformation potential, and deformation potentials under uniaxial strain to determine the

structure of the band gap as a function of the germanium composition. The usefulness of a $\text{Si}_x\text{Ge}_{1-x}$ device comes from the fact that the bandgap in this material is in the near-IR range where optical relay systems comprised of silica-glass waveguides are most efficient¹⁰. This region of efficient operation occurs in the 1.3 μm to 1.5 μm range, above the fundamental bandgap of silicon. Germanium is capable of operation in this regime, but cooling is required to overcome thermal effects.

After the band gap of $\text{Si}_x\text{Ge}_{1-x}$ was determined, attempts were made in the early 1970s to explore the behavior of thin layers of this material. The difficulty of producing thin epilayers of sufficient quality thwarted experimentalist's efforts at that time. It was not until 1985 that the first functional devices were constructed from this material, allowing serious efforts at experimental characterization of MQW structures to proceed.

$\text{Si}_x\text{Ge}_{1-x}$ alloys are produced by strained growth when a heterojunction with pure silicon is present, since the differing lattice constants of Si and $\text{Si}_{1-x}\text{Ge}_x$ must "match" at the heterojunction. This strain produces changes in the band structure of this material from the band structure of an unstrained alloy with similar physical parameters⁷. This change has been included in these computations and is discussed in detail in chapter II. The strained nature of this crystalline structure is the primary source of difficulties in growing high quality thin layers of the type required to produce effective quantum well structures.

Section B. Infrared (IR) Detector Technology

All IR detectors in use are either thermal or photon detectors. These differ in the fundamental detection mode used. Thermal detectors work by inducing heating via

absorption of IR radiation and measuring the temperature induced change in some physical property of the system (resistance, capacitance, etc.). Thermal detectors are further broken down into:

- a) bolometers, which exhibit a change in electrical resistance;
- b) Thermocouples/Thermopiles, which operate on the photovoltaic effect;
- c) Thermopneumatics, which measure an increase in the pressure of a closed chamber, caused by heating of the enclosed gasses due to the temperature rise of the sample; and
- d) Pyroelectrics, which measure the signal voltage generated by a rise in the surface charge of a heated element.¹¹

Thermal detectors, operating via temperature fluctuations, have the disadvantage of being slow and requiring cool down time between detections. Typically, many incident photons are required to raise the temperature by a measurable amount. Despite the drawbacks of thermal systems, research continues to develop low cost, room temperature arrays fabricated with Si pyroelectric detectors. With further development, these systems be used widely due to their simplicity and low cost¹².

Quantum detectors, on the other hand, measure the absorption of a single photon by triggering some quantum event that is then detected. Quantum detectors offer fast response times and greater sensitivity, but typically require cooling to 80° K or lower. Detectors of this sort include intrinsic photon detectors, extrinsic (doped) photon detectors, free carrier detectors, and quantum well structure detectors.

Intrinsic Photodetectors.

Ternary alloy photodetectors, which are intrinsic photon detectors, are constructed of a bulk semiconductor, which is usually an alloy comprised of group II and group VI elements. The bandgaps in these materials are tailored for the desired application by varying the composition percentages of the elements in the alloy. These detectors include $\text{InAs}_{1-x}\text{Sb}_x$, $\text{Hg}_{1-x}\text{Zn}_x\text{Te}$, $\text{Hg}_{1-x}\text{Mn}_x\text{Te}$, and $\text{Hg}_{1-x}\text{Cd}_x\text{Te}$. Currently $\text{Hg}_{1-x}\text{Cd}_x\text{Te}$, known as “merc-cad-telluride” detectors, are the dominant intrinsic detectors available for use in the three to 14 μm region¹. These detector alloys feature a direct bandgap, providing a correspondingly large quantum efficiency, as no phonon interaction is required to allow detection. These detectors tend to have large absorption coefficients and large detectivities (D^*) over a wide range of temperatures and over a fairly wide range of wavelengths (approximately 1.5 to 15 μm). When compared to free carrier and extrinsic photodetectors, thermal noise effects are small. The major problem with these detectors is the continued inability to produce large, high quality arrays. Many of these materials are also highly toxic which makes fabrication more difficult and more expensive¹. A chart showing detector detectivity levels for many of these systems is shown in figure I-5¹³.

Extrinsic Photodetectors.

Extrinsic photodetectors are comprised of a bulk material (often Si) doped with an acceptor. Boron, the most commonly used dopant, is a trivalent acceptor impurity with an ionization energy of 0.045 eV in Si^{14} . This value of energy leads to a lower bound on detectable wavelength of 1.2 μm . Like the intrinsic photodetector described previously,

detection of radiation occurs in the bulk material (in this case the impurities in the bulk material make detection possible), which makes the

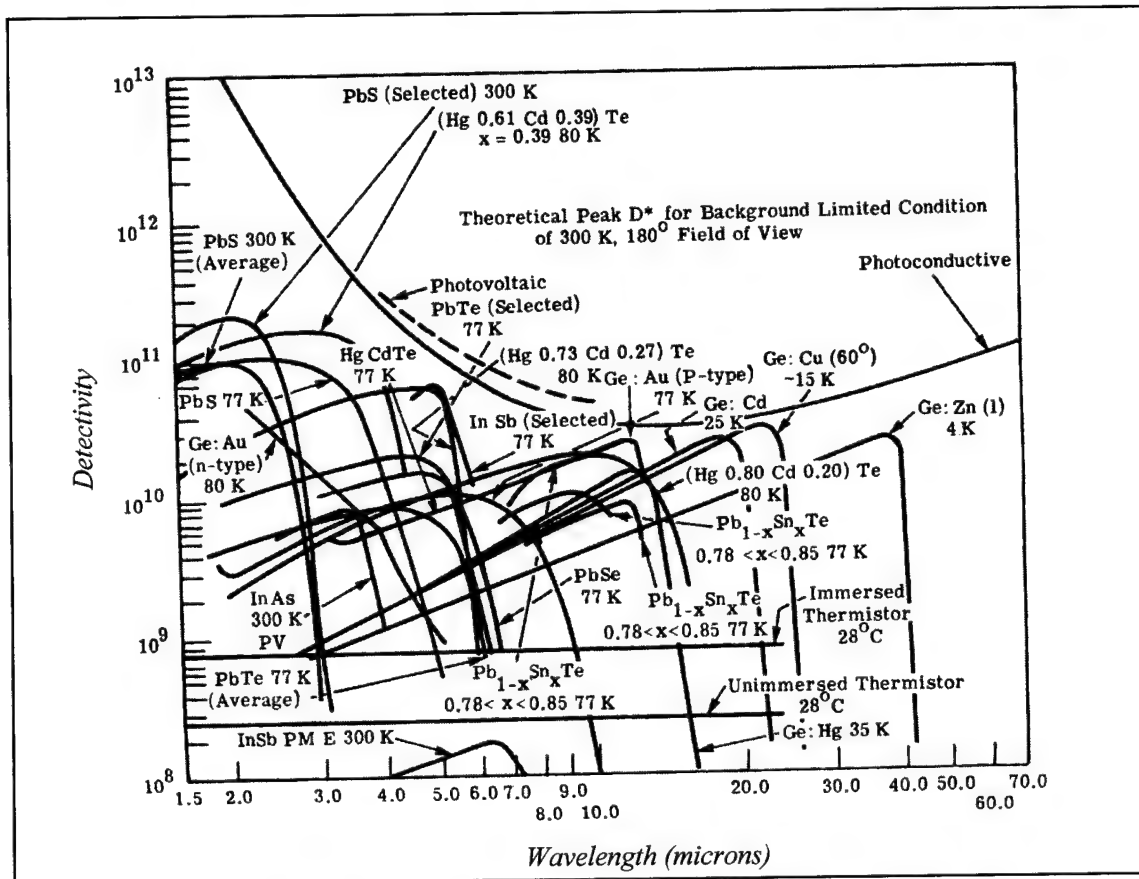


Figure I-5. Spectral D^* for some commercially available materials. (After Ref. 13)

production and development simpler and therefore more efficient. Since the material that detection takes place in is silicon, these detectors are easily integrated with the associated Si circuitry in a monolithic device, increasing the reliability of the resultant detector. The use of bulk Si also means that such detectors can be made with the superior uniformity required for many applications.

Unfortunately, extrinsic Si photodetectors also contain a number of drawbacks. Cooling of such systems to low temperatures is required. A larger drawback lies in the mode of detection, since the only variable parameters are the doping level and dopant

substance. Hence these detectors are not easily tailored for operation over a wide range of wavelength regions¹⁵.

To escape some of the drawbacks of the bulk detectors discussed above, some sort of structure is built into the detector, allowing the variation of design parameters to optimize the detector for a given task. While this approach expands detector capabilities and provides flexibility in the design, it makes the production and design more complex and the detector difficult to produce.

Free Carrier Detectors.

Internal Photo-emission (IP) Photodetectors.

Free carrier (or Internal Photo-emission) photodetectors are based on the principle of photoemission observed in metals since the turn of the century. When a metal is illuminated by light of sufficient wavelength (above a material dependent cutoff frequency) electrons are emitted by the material. The free carrier detector uses such electrons, emitted from an embedded metal contact, to generate the signal after being injected into the conduction band of the semiconductor detector. The most advanced detector technology of this class is the metal silicide Schottky-barrier detector.¹⁶

Heterojunction Internal Photoemission Photodetectors.

Another variety of free carrier photodetector is the Heterojunction Internal Photoemission detector (HIP). This architecture varies from that of the IP detector discussed above in that the metal emitter is replaced by an acceptor doped region which forms a junction with a semiconductor material. The presence of the acceptor region allows holes to be excited in the doped region and swept into the undoped semiconductor region. Devices of this sort fabricated from p⁺SiGe/Si have demonstrated detection in

the 2 to 10 μm range with quantum efficiencies on the order of 4%.¹⁵ Figure I-6 shows the structure of the IP and HIP photodetectors and figure I-7 depicts the band structure for these detectors.

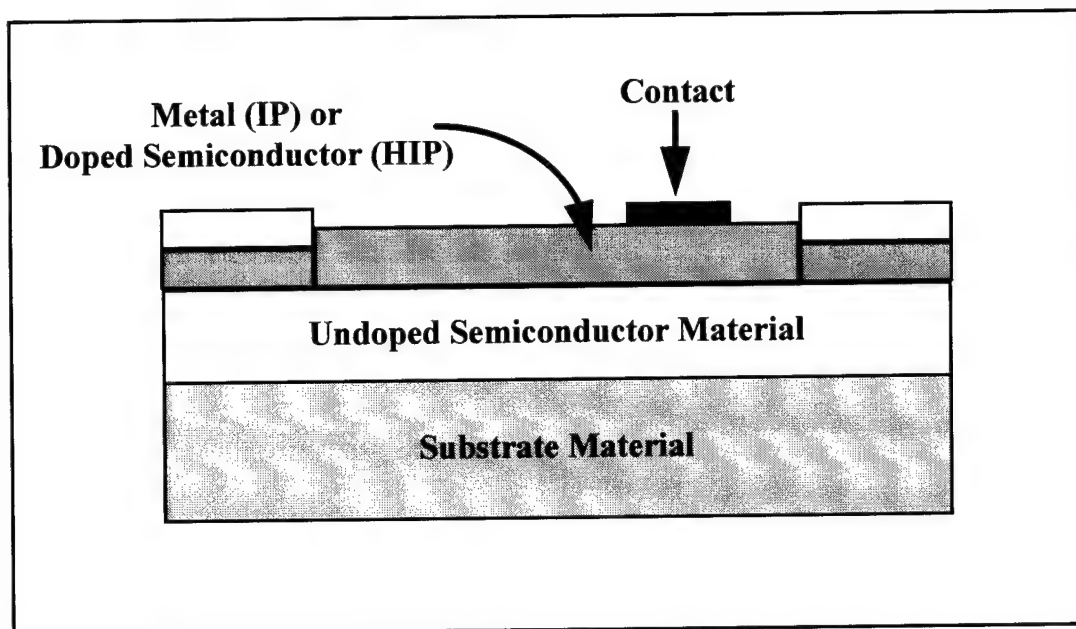


Figure I-6. Structure of the IP or HIP photodetector. The use of a metal instead of a semiconductor material to provide the carriers distinguishes the IP from the HIP detector.

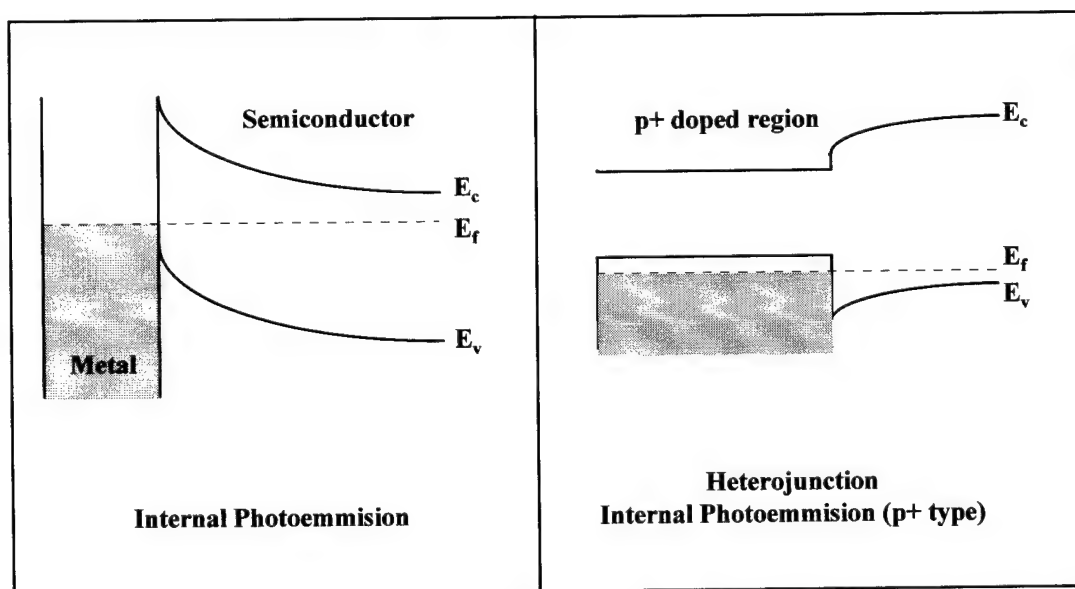


Figure I-7. Band Structure of the IP photodetector and the HIP photodetector. The band structure for the HIP is for a p^+ doped emitter region.

The free carrier detectors feature some degree of spectral discrimination which is achieved by changing the height of the barrier, good uniformity, and reproducibility (since they utilize mature technologies) which are promising with respect to focal plane array applications¹. The drawbacks of the IP detectors are limited spectral response, as band-gaps can only be changed by a finite degree to discriminate between wavelengths, 1% or lower quantum efficiency, and a required trade off in wavelength response versus thermal noise (the barrier must be larger to limit thermal generation bleed over into the conduction band, but this makes the maximum λ go down). The HIP structure suffers from similar disadvantages while having higher quantum efficiencies.¹⁶

Multiple Quantum Well Photodetectors.

It is hoped that the next class of photodetectors, quantum well photodetectors, will remedy some of the shortcomings of the preceding detection systems. The quantum well system offers normal incidence absorption and flexibility of design (many parameters can be adjusted).

A MQW structure is formed by placing alternating layers of different semiconductor materials upon a substrate material. The Si/ $\text{Si}_{1-x}\text{Ge}_x$ MQW structure is formed by alternating layers of $\text{Si}_{1-x}\text{Ge}_x$ alloy (known as the well region) and Si (the barrier region) upon a Si substrate. The differences in bulk band structure between $\text{Si}_{1-x}\text{Ge}_x$ and Si cause an offset in the band structure at the barrier-well heterojunction. Boundary conditions are imposed on the eigenfunctions of the holes, based on the band offsets, and produce bound states within the well. In the formation of bound states, the MQW structure is analogous to the potential well problem that is solved graphically in most elementary quantum mechanics texts.

The quantum well structure is of interest because it serves to localize electron wavefunctions within the well, which can be controlled through the design of the well structure. The structure of the energy bands can be adjusted by changing the percentage of Ge in the well region (x) and the width of the well (L). It is thus possible to tailor the detector to a specific wavelength region through the choice of well design parameters (x and L). A typical quantum well design with the band structure is shown in figure I-8. The band structure of figure I-8 shows the value at the Brillouin zone center of a single band of the bulk band structure.

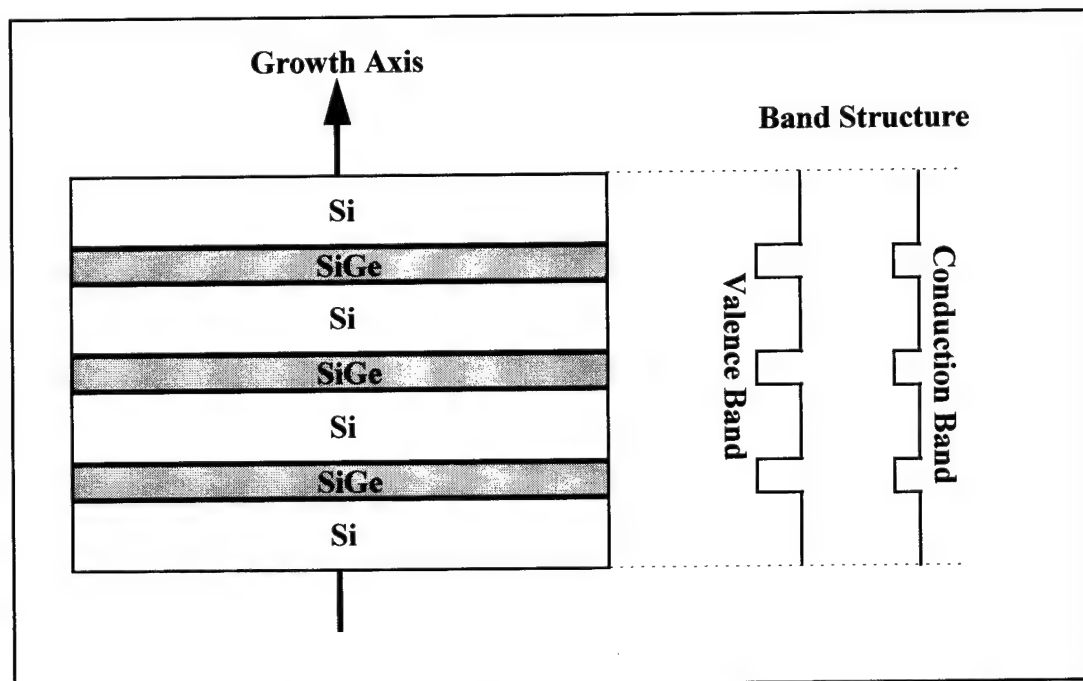


Figure I-8. Typical MQW structure with band structure. The relative sizes of the barrier and well regions are not shown to scale. Typically the barrier regions will be much larger than the well regions for a MQW structure.

The spacing between well regions can be varied when the structure is deposited, with a distinction being drawn between MQW structures where the localized wave functions of particles in adjacent wells do not overlap, and a superlattice where there

exists overlap of the wavefunctions. In a superlattice, the wavefunction overlap of the bound states causes the energy levels of the quantum well structures to broaden and form a series of new band structures known as a mini-bands¹⁷. This approach is used in the design of solid state lasers as well as IR detectors.

The most common deposition technique used to produce MQW devices, Molecular Beam Epitaxy (MBE), is essentially the process of depositing kinetically liberated atoms from isolated sources onto a substrate held in a vacuum chamber¹⁸. The source materials, Si and Ge, are loaded into separate, thermally isolated chambers known as effusion chambers and heated to a high temperature at a low pressure to remove atoms/molecules from the source kinetically. The open ends of the effusion chambers are pointed at the substrate, which is also heated and placed in an ultra-high vacuum. The beam is controlled by shutters placed in front of the effusion chambers which can typically operate at rates which allow the deposition of single atom/molecule layers. In addition to this binary control, the particle flux is changed by changing the source temperature. Using this process, extremely thin, high quality epitaxial layers can be deposited. A similar process known as Chemical Vapor Deposition (CVD) has also been in use to produce these structures since 1987¹⁸.

Effective masses in silicon are higher than those of other materials used in the fabrication of MQW structures to date, so the probability of electrons or holes tunneling through the barrier regions and producing unwanted leakage current is diminished. MQW detectors are reported to offer the promise of high quantum efficiencies ($\eta \approx 0.1$ or greater) and high detectivities ($D_\lambda^* \approx 10^{10} \sqrt{\text{Hz}}/\text{W}$ and greater)¹⁹.

The remainder of this thesis will focus solely on the Si/Si_{1-x}Ge_x MQW structure and the behavior of MQW photodetectors. Many of the details concerning the theoretical operation of the MQW are covered in chapter II, Theory Development. For detailed experimental data regarding the material characteristics of Si/Si_{1-x}Ge_x, including photoresponse and absorption data for a wide range of substrate orientations and well geometries, the reader is referred to Capt. Micheal Gregg's doctoral dissertation.²⁰

Section C. SiGe MQW Device Developments

Experimental Data.

Experimental data characterizing absorbance and photoresponse in various SiGe MQW structures, including data for the Si [110] substrate orientation, has been acquired by M. Gregg of the AFIT Applied Physics Department²⁰. This data will be used as a basis by which to gauge the accuracy of all theoretical results. Experimental data is widely available for MQW structures on Si[001] substrates, but the only existing data on Si[110] MQW structures is that of M. Gregg. The [110] substrate orientation is of interest because this substrate orientation may offer normal incidence absorption in *n*-type MQW detectors and may enhance normal incidence absorption in *p*-type MQW devices²⁰. The [110] substrate system is also of interest because no theoretical calculations are present in the literature for absorption coefficients of devices based on this substrate orientation. The experimental data is available to verify theoretical predictions of device characteristics and perhaps validate some of the underlying assumptions and methods used in making those predictions. The experimental absorption profiles for the system to be modeled are presented in figure I-9²⁰.

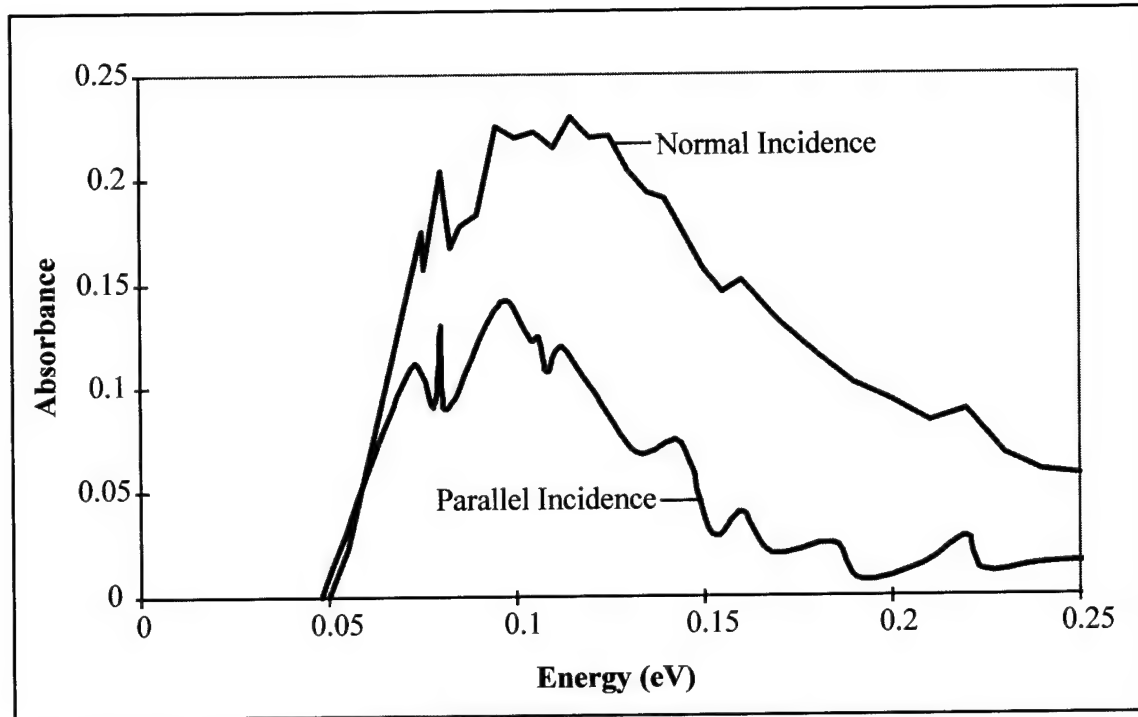


Figure I-9. Absorbance spectra for a Si[110]/Si_{0.70}Ge_{0.30}, 30 Å wide well MQW structure with 15 periods. Sample grown by MBE at 550° C. (After Ref. 20)

History of Theoretical Developments.

Theoretical modeling of semiconductor band structure has its roots in the work of Luttinger and Kohn^{21,22} in the 1950's in developing $\vec{k} \cdot \vec{p}$ theory, the application of effective mass theory to explain the results of cyclotron resonance measurements in semiconductors with complicated band structures and developing the general form of the Hamiltonian for the semiconductor. Luttinger and Kohn's paper is considered the seminal work on this topic. Hiroshi Hasegawa²³ continued the development of $\vec{k} \cdot \vec{p}$ theory in the 1960's, expressing a general form of the Hamiltonian incorporating the $\vec{k} \cdot \vec{p}$ approximation and the effects of strain, but this was limited to the [001] substrate orientation. Bits and pieces of the theory were added through the mid 1980's by various theorists^{2,24-27} and the modeling of quantum well structures began as the capability to

produce them was developed in the early 1980s^{3,7,28,29,30}. Several theorists developed methods of approximating, or solving exactly over limited regimes, the band structure of these devices. Perhaps most important to this study are the works of Szmulowicz and Brown³ and M. Gregg's doctoral dissertation²⁰. Szmulowicz adapted the $\vec{k} \cdot \vec{p}$ approach to model the GaAs/Al_xGa_{1-x}As MQW structure to determine bound-to-bound and bound-to-continuum linear absorption coefficients in this structure.

M. Gregg models the Si/Si_{1-x}Ge_x MQW structure for a variety of substrate orientations and computes the momentum matrix elements for transitions among valence states. M. Gregg has modeled the MQW valence subbands via the EFA method and has provided the form of the subbands and the momentum matrix elements that are required to model the absorption coefficients. It is upon this foundation that the formulation of the bound-to-bound absorption coefficients of this project will proceed.

Chapter II. Theory Development

Section A. Introduction and Organization

A more complete theoretical description of the Si[110]/Si_{1-x}Ge_x MQW system is developed in the following two chapters. This description is based upon three major developmental steps:

- (1) Determine an approximate Hamiltonian for bulk Si and Si_{1-x}Ge_x derived from the $\vec{k} \cdot \vec{p}$ theory of Luttinger and Kohn²¹,
- (3) Use MQW boundary conditions and the envelope function approximation (EFA) formalism to obtain the bound state eigenfunctions in the growth direction of the well,
- (4) Determine the linear absorption coefficients as a function of wavelength using the bound state eigenfunctions.

A solution to the simple, one dimensional square well problem is also developed in Appendix A to provide an analogy to the method of solution used for the MQW problem.

Section B. Development of the Hamiltonian in the Bulk Semiconductor

An approximate form of the Hamiltonian for the bulk semiconductor must be known before the hole eigenfunctions can be calculated. The total Hamiltonian in the bulk material is comprised of a number of terms:

- (1) a term due to the kinetic energy of the holes,
- (2) a term due to the periodic potential due to the lattice,

(3) a term due to the spin-orbit interaction, and

(4) a term due to the effects of strained growth (in the SiGe alloy).

The terms listed above are the only effects that this study will treat. Terms representing other physical interactions such as coupling of the conduction and valence bands and electron-electron interactions are not included in the Hamiltonian and are assumed to be much smaller in magnitude than the terms considered.

The first task in developing the total bulk Hamiltonian, H_1 , is to examine the contribution due to the presence of the periodic potential of the lattice and the momentum of the particle itself. This can be done through the framework of the $\vec{k} \cdot \vec{p}$ theory developed by Luttinger and Kohn in the 1950's.²¹

The Hamiltonian describing the behavior of the holes in the bulk semiconductor is

$$H = \frac{p^2}{2m} + V(\mathbf{r}) \quad (1)$$

where $V(\mathbf{r})$ has the periodicity of the lattice. The hole eigenvalues and eigenvectors are obtained by representing the Hamiltonian of equation 1 in a basis given by Luttinger and Kohn²¹.

The basis that H will be represented in is developed by first considering Bloch's theorem. Bloch's theorem states that the hole eigenfunction in the solid is expressible as a plane wave times a function possessing the periodicity of the lattice, given by

$$\Psi_{n\mathbf{k}}(\mathbf{r}) = e^{i\mathbf{k} \cdot \mathbf{r}} \cdot u_{n\mathbf{k}}(\mathbf{r}) \quad (2)$$

where n is a band label and \mathbf{k} is the wavevector within the first Brillouin zone of the crystal²¹. The $u_{n\mathbf{k}}(\mathbf{r})$ are functions which have the periodicity of the lattice. The cell periodic parts of the eigenfunctions may be expanded in Fourier series to yield

$$\Psi_{n\mathbf{k}}(\mathbf{r}) = e^{i\mathbf{k}\cdot\mathbf{r}} \cdot \sum_m B_m^n(\mathbf{k}) e^{-i\mathbf{k}_m\cdot\mathbf{r}}, \quad (3)$$

where the \mathbf{k}_m are reciprocal lattice vectors and the $B_m^n(\mathbf{k})$ are expansion coefficients. As shown by Luttinger and Kohn, the eigenfunction near Brillouin zone center may also be expressed as

$$\begin{aligned} \chi_{n\mathbf{k}}(\mathbf{r}) &= e^{i\mathbf{k}\cdot\mathbf{r}} \cdot u_{n0}(\mathbf{r}) \\ &= e^{i\mathbf{k}\cdot\mathbf{r}} \cdot \sum_m B_m^n(\mathbf{k}=0) e^{-i\mathbf{k}_m\cdot\mathbf{r}} \end{aligned} \quad (4)$$

In bra-ket notation, the eigenfunction of equation 3 is expressed as

$$|\Psi_{n\mathbf{k}}\rangle = \sum_m B_m^n(\mathbf{k}) |\mathbf{k} - \mathbf{k}_m\rangle \quad (5)$$

and equation 4 is expressed as

$$|n\mathbf{k}\rangle = \sum_m B_m^n(0) |\mathbf{k} - \mathbf{k}_m\rangle \quad (6)$$

The Luttinger-Kohn basis in equation 6 may be conveniently expressed as

$$|n\mathbf{k}\rangle = T(\mathbf{k}) |u_{n0}\rangle \quad (7)$$

where

$$|u_{n0}\rangle \equiv \sum_m B_m^n(0) |-\mathbf{k}_m\rangle \quad (8)$$

and $T(\mathbf{k})$ is the *boost operator*, $e^{i\mathbf{k}\cdot\hat{\mathbf{r}}}$, which will increase \mathbf{k} when applied to an eigenfunction.

The form of the matrix elements of the Hamiltonian will be determined next, using the Luttinger-Kohn basis. The matrix elements of the Hamiltonian

$$H_{n\mathbf{k},n'\mathbf{k}'} \equiv \langle n\mathbf{k} | \left(\frac{\hat{p}^2}{2m} + V(\mathbf{r}) \right) | n'\mathbf{k}' \rangle \quad (9)$$

are evaluated by using equation 6 and

$$\hat{\mathbf{p}} | n\mathbf{k} \rangle = \hbar \hat{\mathbf{k}} | n\mathbf{k} \rangle. \quad (10)$$

Equation 9 may be expressed as

$$H_{n\mathbf{k},n'\mathbf{k}'} = \langle n'\mathbf{k}' | \frac{\hat{p}^2}{2m} | n\mathbf{k} \rangle + \langle n'\mathbf{k}' | V(\mathbf{r}) | n\mathbf{k} \rangle \quad (11)$$

and each part evaluated by replacing $| n\mathbf{k} \rangle$ with the expression of equation 6. The first quantity on the right hand side of equation 11 is

$$\frac{1}{2m} \langle n'\mathbf{k}' | \hat{\mathbf{p}} \cdot (\hat{\mathbf{p}} | n\mathbf{k} \rangle) \quad (12)$$

where

$$\begin{aligned} \hat{\mathbf{p}} | n\mathbf{k} \rangle &= \hat{\mathbf{p}} \left(\sum_m B_m^n(0) | \mathbf{k} - \mathbf{k}_m \rangle \right) \\ &= \hbar \sum_m B_m^n(0) \hat{\mathbf{k}} | \mathbf{k} - \mathbf{k}_m \rangle \end{aligned} \quad (13)$$

The result of equation 13 is evaluated through the use of

$$\hat{\mathbf{k}} | \mathbf{k} \rangle = \mathbf{k} | \mathbf{k} \rangle, \quad (14)$$

so that

$$\hbar \sum_m B_m^n(0) \hat{\mathbf{k}} | \mathbf{k} - \mathbf{k}_m \rangle = \hbar \mathbf{k} \sum_m B_m^n(0) | \mathbf{k} - \mathbf{k}_m \rangle - \hbar \sum_m B_m^n(0) \mathbf{k}_m | \mathbf{k} - \mathbf{k}_m \rangle. \quad (15)$$

When equation 13 is evaluated using equation 15, the result is

$$\hat{\mathbf{p}}|n\mathbf{k}\rangle = \hbar\mathbf{k}|n\mathbf{k}\rangle - \hbar\sum_m B_m^n(0)\mathbf{k}_m|\mathbf{k} - \mathbf{k}_m\rangle. \quad (16)$$

The effect of the operator $\hat{\mathbf{p}}$ on the right hand side of equation 16 is

$$\begin{aligned} \hat{p}^2|n\mathbf{k}\rangle &= \hbar^2 k^2|n\mathbf{k}\rangle - 2\hbar^2\mathbf{k}\sum_m B_m^n(0)\mathbf{k}_m|\mathbf{k} - \mathbf{k}_m\rangle \\ &\quad + \hbar^2\sum_m B_m^n(0)\mathbf{k}_m^2|\mathbf{k} - \mathbf{k}_m\rangle. \end{aligned} \quad (17)$$

Equation 17 is re-expressed as

$$\hat{p}^2|n\mathbf{k}\rangle = \hbar^2 T(\mathbf{k})\left\{k^2|u_{n0}\rangle - 2\mathbf{k}\sum_m B_m^n(0)\mathbf{k}_m|-\mathbf{k}_m\rangle + \sum_m B_m^n(0)\mathbf{k}_m^2|-\mathbf{k}_m\rangle\right\} \quad (18)$$

Remembering that $\hat{\mathbf{k}}|\mathbf{k}\rangle = \mathbf{k}|\mathbf{k}\rangle$, the above equation can be simplified to

$$\hat{p}^2|n\mathbf{k}\rangle = \hbar^2 T(\mathbf{k})\left\{k^2|u_{n0}\rangle - 2\mathbf{k}\hat{\mathbf{k}}\sum_m B_m^n(0)|-\mathbf{k}_m\rangle + \hat{\mathbf{k}}^2\sum_m B_m^n(0)|-\mathbf{k}_m\rangle\right\}, \quad (19)$$

or, letting $\hat{\mathbf{p}} = \hbar\hat{\mathbf{k}}$ and simplifying,

$$\hat{p}^2|n\mathbf{k}\rangle = T(\mathbf{k})\left\{\frac{\hbar^2 k^2}{2m}|u_{n0}\rangle + \frac{\hbar\mathbf{k}}{m}\cdot\hat{\mathbf{p}}|u_{n0}\rangle + \frac{p^2}{2m}|u_{n0}\rangle\right\}. \quad (20)$$

Note the appearance of the $\mathbf{k} \cdot \hat{\mathbf{p}}$ term from which the theory earned its moniker. Using the result of equation 20, matrix elements of the Hamiltonian in equation 1 are given by

$$\langle n'\mathbf{k}'|H|n\mathbf{k}\rangle = \langle u_{n0}|T^\dagger(\mathbf{k}')T(\mathbf{k})\left\{\frac{p^2}{2m} + V(\mathbf{r}) + \frac{\hbar}{m}\mathbf{k} \cdot \hat{\mathbf{p}} + \frac{\hbar^2 k^2}{2m}\right\}|u_{n0}\rangle. \quad (21)$$

The symbol T^\dagger is used above to represent the Hermitian adjoint of the boost operator and $T^\dagger(\mathbf{k}')T(\mathbf{k})$ is given by

$$T^\dagger(\mathbf{k}')T(\mathbf{k}) = e^{i(\mathbf{k}-\mathbf{k}')\hat{\mathbf{r}}} = T(\mathbf{k} - \mathbf{k}') \quad (22)$$

by the definition of the boost operator.

Matrix elements given by the first term in equation 21 are

$$\begin{aligned}\langle u_{n'0} | T^\dagger(\mathbf{k}') T(\mathbf{k}) H | u_{n0} \rangle &= E_{n0} \langle u_{n'0} | T^\dagger(\mathbf{k}') T(\mathbf{k}) | u_{n0} \rangle, \\ &= E_{n0} \langle n' \mathbf{k}' | n \mathbf{k} \rangle,\end{aligned}\quad (23)$$

where $H = p^2/2m + V(r)$ and E_{n0} is the zone center energy of the band. Only diagonal matrix elements are non-zero since the basis vectors $|n\mathbf{k}\rangle$ form a complete orthonormal set²¹,

$$\langle n' \mathbf{k}' | n \mathbf{k} \rangle = \delta_{nn'} \delta(\mathbf{k} - \mathbf{k}'). \quad (24)$$

The energy E_{n0} represents the energy of the band at zone center. Since this study focuses on intra-subband transitions, the absolute magnitudes of the energies of the subbands are irrelevant and only the differences between subband energies are important. As a result, the zero point of the energy is typically chosen so that E_{n0} is zero. The third term in equation 21 is given by

$$\begin{aligned}\langle u_{n'0} | T^\dagger(\mathbf{k}') T(\mathbf{k}) \frac{\hbar^2 k^2}{2m} | u_{n0} \rangle &= \frac{\hbar^2 k^2}{2m} \langle n' \mathbf{k}' | n \mathbf{k} \rangle \\ &= \frac{\hbar^2 k^2}{2m} \delta_{nn'} \delta(\mathbf{k} - \mathbf{k}'),\end{aligned}\quad (25)$$

and is also nonzero only for diagonal matrix elements. The two diagonal terms of equations 23 and 25 are grouped together and represented by the symbol H_0 .

The second term in equation 21 is evaluated as

$$\begin{aligned}\langle u_{n'0} | T(\mathbf{k} - \mathbf{k}') \frac{\hbar \mathbf{k}}{m} \hat{\mathbf{p}} | u_{n0} \rangle &= \frac{\hbar \mathbf{k}}{m} \sum_{m, m'} B_m^n(0) B_{m'}^{n'}(0) \langle -\mathbf{k}_{m'} | T(\mathbf{k} - \mathbf{k}') \hat{\mathbf{p}} | -\mathbf{k}_m \rangle \\ &= \frac{\hbar \mathbf{k}}{m} \left((-\hbar) \sum_{m, m'} B_{m'}^{n'}(0) B_m^n(0) \mathbf{k}_m \langle \mathbf{k}' - \mathbf{k}_m | \mathbf{k} - \mathbf{k}_m \rangle \right).\end{aligned}\quad (26)$$

Using the orthogonality of the basis functions, equation 26 is expressed as

$$\langle u_{n'0} | T(\mathbf{k} - \mathbf{k}') \frac{\hbar \mathbf{k}}{m} \hat{\mathbf{p}} | u_{n0} \rangle = \frac{-\hbar^2 \mathbf{k}}{m} \sum_{m,m'} B_{m'}^{n'}(0) B_m^n(0) \mathbf{k}_m \delta(\mathbf{k}' - \mathbf{k}_{m'} - \mathbf{k} + \mathbf{k}_m). \quad (27)$$

The delta function in equation 27 can be simplified somewhat by examining the geometry of the reciprocal lattice. Due to the fact that the wave vector lies in the first Brillouin

zone, \mathbf{k}' and \mathbf{k} must lie between $-\frac{\pi}{a}$ and $\frac{\pi}{a}$. The difference between the reciprocal

lattice vectors $\mathbf{k}_{m'} - \mathbf{k}_m$ is defined to be a reciprocal lattice vector $\mathbf{K}_{m-m'}$. In order for

$\mathbf{K}_{m-m'}$ to be in the first Brillouin zone, m' must equal m and thus

$$\delta(\mathbf{k}' - \mathbf{k} - \mathbf{K}_{m-m'}) = \delta(\mathbf{k}' - \mathbf{k}) \delta_{m'm}. \quad (28)$$

The matrix elements given by equation 27 are then given by

$$\langle u_{n'0} | T(\mathbf{k} - \mathbf{k}') \frac{\hbar \mathbf{k}}{m} \hat{\mathbf{p}} | u_{n0} \rangle = \frac{\hbar}{m} \mathbf{k} \cdot \mathbf{p}_{nn'} \delta(\mathbf{k}' - \mathbf{k}), \quad (29)$$

where inter-band momentum matrix elements are defined as

$$\mathbf{p}_{nn'} \equiv -\hbar \sum_{m,m'} B_{m'}^{n'}(0) B_m^n(0). \quad (30)$$

Using the results of equations 23, 25, and 29 the matrix elements of the Hamiltonian of equation 21 are given by

$$\begin{aligned} \langle n'k' | H | nk \rangle = & \left(E_{n0} + \frac{\hbar^2 k^2}{2m} \right) \delta_{nn'} \delta(\mathbf{k}' - \mathbf{k}) \\ & + \left(\frac{\hbar \mathbf{k}}{m} \mathbf{p}_{nn'} \right) \delta(\mathbf{k}' - \mathbf{k}). \end{aligned} \quad (31)$$

The second term of equation 31 is not diagonalized in the $|n\mathbf{k}\rangle$ basis, so a unitary transformation of the Hamiltonian H is performed in order to diagonalize H to second order in \mathbf{k} .

Defining a new basis set,

$$|\delta_{nk}\rangle = e^{\zeta} |n\mathbf{k}\rangle, \quad (32)$$

ζ may be chosen so that H is diagonalized. The matrix elements of the Hamiltonian H' are given by

$$\langle \delta_{n'k'} | H | \delta_{nk} \rangle = \langle n'k' | e^{-\zeta} H e^{\zeta} | n\mathbf{k} \rangle \quad (33)$$

where H is diagonal in the $|\delta_{nk}\rangle$ basis. The term within the bra-ket on the right hand side can be expanded via the expansion of the exponent in Taylor Series, yielding

$$e^{-\zeta} H e^{\zeta} = \left(1 - \zeta + \frac{\zeta^2}{2} + \dots \right) \cdot (H_0 + H_{k,p}) \cdot \left(1 + \zeta + \frac{\zeta^2}{2} + \dots \right) \quad (34)$$

which when expanded yields

$$e^{-\zeta} H e^{\zeta} = H_0 + H_{k,p} + [H_0, \zeta] + [H_{k,p}, \zeta] + \frac{1}{2} [[H_0, \zeta], \zeta] + \dots \quad (35)$$

where the brackets are commutator notation and

$$H_{k,p} \equiv T^\dagger(\mathbf{k}) \left(\frac{\hbar}{m} \mathbf{k} \cdot \hat{\mathbf{p}} \right) T(\mathbf{k}) \quad (36)$$

in the $|n\mathbf{k}\rangle$ basis.

The value of ζ is selected such that $H_{k,p} = -[H_0, \zeta]$, which cancels two of the terms of

equation 35. Ignoring the higher order terms (in ς) of equation 35 leads to

$$H' = H_0 + \frac{1}{2} H_{k,p} \cdot \varsigma - \frac{1}{2} \varsigma \cdot H_{k,p}. \quad (37)$$

Evaluating the expectation value of $H_{k,p}$ via the use of completeness and the relationship

$H_{k,p} = -[H_0, \varsigma]$ leads to the following expression for the matrix elements of $H_{k,p}$

$$\langle n' \mathbf{k}' | H_{k,p} | n \mathbf{k} \rangle = \left(E_{n'0} + \frac{\hbar^2 k'^2}{2m} \right) \langle n' \mathbf{k}' | \varsigma | n \mathbf{k} \rangle - \left(E_{n0} + \frac{\hbar^2 k^2}{2m} \right) \langle n' \mathbf{k}' | \varsigma | n \mathbf{k} \rangle. \quad (38)$$

This expression is equal to the matrix elements derived in equation 29, providing a means of solving for ς

$$\langle n' \mathbf{k}' | \varsigma | n \mathbf{k} \rangle = \frac{\frac{\hbar \mathbf{k}}{m} P_{n'n} \delta(\mathbf{k}' - \mathbf{k})}{(E_{n'} - E_n)} \quad (39)$$

so that the value of ς has been determined as a function of $P_{n'n}$ in the non-degenerate case.

This expression can be used then to evaluate the matrix elements of the Hamiltonian, which is our principal goal,

$$\langle n' \mathbf{k}' | H | n \mathbf{k} \rangle = \langle n' \mathbf{k}' | H_0 | n \mathbf{k} \rangle + \frac{1}{2} \langle n' \mathbf{k}' | H_{k,p} \varsigma | n \mathbf{k} \rangle - \frac{1}{2} \langle n' \mathbf{k}' | \varsigma H_{k,p} | n \mathbf{k} \rangle \quad (40)$$

and when equation 40 is evaluated via the expressions developed in equations 31 and 38,

the result is (to second order in \mathbf{k})

$$\langle n' \mathbf{k}' | H | n \mathbf{k} \rangle = \left(E_{n0} + \frac{\hbar^2 k^2}{2m} + \frac{k^2}{m^2} \sum_{n''} \frac{\mathbf{p}_{nn''} \mathbf{p}_{n''n}}{(E_n - E_{n''})} \right) \delta(k' - k). \quad (41)$$

Equation 41 provides diagonal matrix elements of the non-degenerate Hamiltonian in

terms of $\mathbf{p}_{n''n}$ and \bar{k} .

The valence subbands which this project focus on are degenerate, so the formulation of equation 41 is inappropriate in the current case and degenerate perturbation theory must be applied. The analysis in the degenerate case leads to a block diagonal form of the bulk Hamiltonian, which can be expressed in terms of a linear combination of angular momentum operators^{21,23}. The expansion coefficients of these linear combinations are composed of experimentally determined parameters (the Luttinger parameters, γ_i) and powers of \mathbf{k} . The expression of the Hamiltonian given by Hasegawa²³ is the one which will be used in this study.

General Form of the Bulk Hamiltonian.

The form of the Hamiltonian given by Hasegawa is

$$H' = \frac{-\hbar^2}{2m_0} \left\{ 2\gamma_1 (k_{xx} + k_{yy} + k_{zz}) I_6 - 12\gamma_2 \left[\left(L_x^2 - \frac{1}{3} L^2 \right) \cdot k_x + c.p. \right] - 24\gamma_3 \left[\left(L_x \cdot L_y \right) k_{xy} + c.p. \right] \right\} \quad (42)$$

where $k_{\alpha\beta} = \frac{1}{2} (k_\alpha^* k_\beta + k_\beta^* k_\alpha)$, $c.p.$ stands for cyclic permutations with respect to x, y, and z, I_6 is the 6×6 identity matrix, $H' = H_0 + H_{kp}$, and γ_1 , γ_2 , and γ_3 are the Luttinger parameters, which are material dependent. Equation 42 produces a 6×6 matrix based on group theory concepts that are beyond the scope of this project. At present, the best available method of determining these parameters (and all other material dependent, experimentally determined parameters) in the SiGe alloy is to interpolate between the values given for Si and for Ge, based on x the Ge percentage of the alloy.

The angular momentum matrices here are given in the $|l m_l s m_s \mathbf{k}\rangle$ basis where the quantum numbers used are those of the atomic 3p state: $l=(1)$, $m_l=(-1,0,1)$, $s=(\frac{1}{2})$, and $m_s=(\frac{1}{2}, -\frac{1}{2})$. The angular momentum matrices are given by

$$L_x = \frac{1}{\sqrt{2}} \begin{pmatrix} 0 & 0 & 1 & 0 & 0 & 0 \\ 0 & 0 & 0 & 1 & 0 & 0 \\ 1 & 0 & 0 & 0 & 1 & 0 \\ 0 & 1 & 0 & 0 & 0 & 1 \\ 0 & 0 & 1 & 0 & 0 & 0 \\ 0 & 0 & 0 & 1 & 0 & 0 \end{pmatrix}, \quad (43)$$

$$L_y = \frac{i}{\sqrt{2}} \begin{pmatrix} 0 & 0 & -1 & 0 & 0 & 0 \\ 0 & 0 & 0 & -1 & 0 & 0 \\ 1 & 0 & 0 & 0 & -1 & 0 \\ 0 & 1 & 0 & 0 & 0 & -1 \\ 0 & 0 & 1 & 0 & 0 & 0 \\ 0 & 0 & 0 & 1 & 0 & 0 \end{pmatrix}, \quad (44)$$

$$L_z = \begin{pmatrix} 1 & 0 & 0 & 0 & 0 & 0 \\ 0 & 1 & 0 & 0 & 0 & 0 \\ 0 & 0 & 0 & 0 & 0 & 0 \\ 0 & 0 & 0 & 0 & 0 & 0 \\ 0 & 0 & 0 & 0 & -1 & 0 \\ 0 & 0 & 0 & 0 & 0 & -1 \end{pmatrix}, \quad (45)$$

and

$$L^2 = 2 \begin{pmatrix} 1 & 0 & 0 & 0 & 0 & 0 \\ 0 & 1 & 0 & 0 & 0 & 0 \\ 0 & 0 & 1 & 0 & 0 & 0 \\ 0 & 0 & 0 & 1 & 0 & 0 \\ 0 & 0 & 0 & 0 & 1 & 0 \\ 0 & 0 & 0 & 0 & 0 & 1 \end{pmatrix}. \quad (46)$$

The eigenvalues of the 6×6 Hamiltonian matrix given by equation 42 provide dispersion relations for the bulk material ($E(\mathbf{k})$), which at this point are degenerate at $\mathbf{k}=0$ and are parabolic in form, as shown in figure II-1, page II-19.

Coordinate Systems and Relationship to Crystal Lattice.

The expression of equation 42 is valid only for a specific lattice orientation and the values of L and \vec{k} must be rotated into a coordinate system that is consistent with the particular crystal orientation to be examined. This is accomplished using a rotation matrix,

$$R = \begin{bmatrix} \cos\theta\cos\varphi & -\sin\varphi & \sin\theta\cos\varphi \\ \cos\theta\sin\varphi & \cos\varphi & \sin\theta\sin\varphi \\ -\sin\theta & 0 & \cos\theta \end{bmatrix} \quad (47)$$

where the required rotations are given by

$$\begin{bmatrix} L_{x'} \\ L_{y'} \\ L_{z'} \end{bmatrix} = R \cdot \begin{bmatrix} L_x \\ L_y \\ L_z \end{bmatrix} \quad (48)$$

$$\begin{bmatrix} k_{x'} \\ k_{y'} \\ k_{z'} \end{bmatrix} = R \cdot \begin{bmatrix} k_x \\ k_y \\ k_z \end{bmatrix} \quad (49)$$

and the values of θ and φ are shown in table II-1 for the [001], [110], and [111] substrate orientations.

Table II-1.
Euler Angles (θ and φ) for Coordinate Rotation

Z Axis Direction	Theta (θ)	Psi (φ)
[001]	0	$\pi/4$
[110]	$\pi/2$	$\pi/4$
[111]	$\cos^{-1}(1/\sqrt{3})$	$\pi/4$

Spin-Orbit Interaction.

The interaction between the spin and the orbital angular momentum of the holes will affect the energy values of the holes in the bulk semiconductor. The spin orbit interaction is easily represented in the $|j m_j\rangle$ basis, where it is diagonal. The Hamiltonian, H_{so} , that describes the spin-orbit interaction is

$$H_{so} = \begin{pmatrix} 0 & 0 & 0 & 0 & 0 & 0 \\ 0 & 0 & 0 & 0 & 0 & 0 \\ 0 & 0 & 0 & 0 & 0 & 0 \\ 0 & 0 & 0 & 0 & 0 & 0 \\ 0 & 0 & 0 & 0 & -\Delta & 0 \\ 0 & 0 & 0 & 0 & 0 & -\Delta \end{pmatrix} \quad (50)$$

in the $|j m_j\rangle$ basis, where Δ is the spin-orbit energy, an experimentally determined parameter. In order to use the spin-orbit interaction Hamiltonian in the $|j m_j\rangle$ basis, the Hamiltonian of equation 44 must also be represented in the $|j m_j\rangle$ basis (remember that H' is currently represented in the $|l, m_l, s, m_s\rangle$ basis). This may be done by either transforming matrix representations of the angular momentum operators via a unitary transformation using the Clebsch-Gordon coefficients or by using an equivalent transformation (differing by a phase factor) developed by Luttinger and Kohn²¹,

$$LK = \begin{pmatrix} -1 & 0 & 0 & 0 & 0 & 0 \\ 0 & -i\sqrt{\frac{1}{3}} & 0 & 0 & -\sqrt{\frac{2}{3}} & 0 \\ 0 & -i\sqrt{\frac{2}{3}} & 0 & 0 & \sqrt{\frac{1}{3}} & 0 \\ 0 & 0 & \sqrt{\frac{2}{3}} & 0 & 0 & i\sqrt{\frac{1}{3}} \\ 0 & 0 & \sqrt{\frac{1}{3}} & 0 & 0 & -i\sqrt{\frac{2}{3}} \\ 0 & 0 & 0 & i & 0 & 0 \end{pmatrix}. \quad (51)$$

When this transformation to the $|j, m_j\rangle$ basis is performed, the spin-orbit Hamiltonian may be added to the Hamiltonian H . This results in a new Hamiltonian

$$H = H_0 + H_{k.p} + H_{so}, \quad (52)$$

where

$$H = \begin{pmatrix} hh & \alpha & \beta & 0 & \frac{i\alpha}{\sqrt{2}} & -i\beta\sqrt{2} \\ \alpha^* & lh & 0 & \beta & \frac{i\delta}{\sqrt{2}} & i\alpha\sqrt{\frac{3}{2}} \\ \beta^* & 0 & lh & -\alpha & -i\alpha^*\sqrt{\frac{3}{2}} & \frac{i\delta^*}{\sqrt{2}} \\ 0 & \beta^* & -\alpha^* & hh & -i\beta^*\sqrt{2} & \frac{-i\alpha^*}{\sqrt{2}} \\ \frac{-i\alpha^*}{\sqrt{2}} & \frac{-i\delta^*}{\sqrt{2}} & i\alpha\sqrt{\frac{3}{2}} & i\beta\sqrt{2} & so - \Delta & 0 \\ i\beta^*\sqrt{2} & -i\alpha^*\sqrt{\frac{3}{2}} & \frac{-i\delta}{\sqrt{2}} & \frac{i\alpha}{\sqrt{2}} & 0 & so - \Delta \end{pmatrix}. \quad (53)$$

Matrix elements (except the $-\Delta$ terms) in equation 53 are calculated by using equations 42 through 47 and transforming to the $|j, m_j\rangle$ representation via the unitary transformation given in equation 51. The terms that make up H , in the case of the [110] substrate orientation, are given in equations 54 through 59.

$$\begin{aligned}
 hh &= \gamma_1(k_x^2 + k_y^2 + k_z^2) + \gamma_2(k_x^2 + k_y^2 - 2k_z^2) \\
 lh &= \gamma_1(k_x^2 + k_y^2 + k_z^2) - \gamma_2(k_x^2 + k_y^2 - 2k_z^2) \\
 so &= \gamma_1(k_x^2 + k_y^2 + k_z^2) \\
 \alpha &= -2i\sqrt{3}(k_x - ik_y)k_z\gamma_3 \\
 \beta &= \sqrt{3}\gamma_2(k_x^2 - k_y^2) - 2i\gamma_3k_xk_y \\
 \delta &= lh - hh
 \end{aligned} \tag{54-59}$$

The eigenvalues of H form three subbands with two different values at zone center, a set corresponding to the $j=3/2$ states (which is quadruply degenerate at zone center) and a separate set for $j=1/2$ (doubly degenerate at zone center). The two subbands that are quadruply degenerate at subband center are known as the heavy hole and light hole subbands and the remaining set is known as the split-off subband. These names derive from the effective mass of the subbands, and from the fact that the lower subband is split off from the top two subbands.

Strain Induced Perturbation.

The band structure resulting from the eigenvalues of H (given by equation 52) may be further refined, by including strain terms resulting from the accommodation of the Si and Ge atoms into the same lattice. As discussed in Chapter I, Si and Ge each have different lattice constants, so when the two elements are combined into a single lattice with Si and Ge interspersed at random intervals and grown upon a Si substrate lattice, the

resulting lattice will be distorted or will have lattice defects in the vicinity of the boundary layer²⁰. This strain will serve to alter the energy band structure, removing the fourfold zone center degeneracy and moving the light or heavy hole subbands to lower energy (depending on the nature of the strain, either compressing or decompressing the lattice respectively), so that the resulting structure will feature distinct heavy, light and split-off subbands at zone center.

The form of the strain Hamiltonian may also be expressed in terms of the angular momentum matrices. Matrix elements are calculated using experimentally determined deformation potentials, and the applicable strain components. The deformation potentials are written as D_i where i is equal to 0, 1 or 2, and depend on the material composition.²³

The strain Hamiltonian, given by Kleiner and Roth²⁶ is

$$H_{strain} = \begin{pmatrix} e_1 + e_2 & 0 & e_3 & 0 & 0 & -i\sqrt{2}e_3 \\ 0 & e_1 - e_2 & 0 & e_3 & -i\sqrt{2}e_2 & 0 \\ e_3 & 0 & e_1 - e_2 & 0 & 0 & -i\sqrt{2}e_2 \\ 0 & e_3 & 0 & e_1 + e_2 & -i\sqrt{2}e_3 & 0 \\ 0 & i\sqrt{2}e_2 & 0 & i\sqrt{2}e_3 & e_1 & 0 \\ i\sqrt{2}e_3 & 0 & i\sqrt{2}e_2 & 0 & 0 & e_1 \end{pmatrix} \quad (60)$$

where

$$\begin{aligned} e_1 &= D_1(2e_{xx} + e_{zz}) \\ e_2 &= -D_2 \frac{(e_{zz} - e_{xx})}{3} + D_3 \frac{e_{xy}}{2} \\ e_3 &= -D_2 \frac{(e_{xx} - e_{zz})}{\sqrt{3}} + D_3 \frac{e_{xy}}{2\sqrt{3}}, \end{aligned} \quad (61)$$

and the strain components, $e_{\alpha\beta}$, are defined as

$$e_{\alpha\beta} = \begin{cases} \frac{\partial u_{\alpha}}{\partial x_{\beta}} + \frac{\partial u_{\beta}}{\partial x_{\alpha}} & (\alpha \neq \beta) \\ \frac{\partial u_{\alpha}}{\partial x_{\alpha}} & (\alpha = \beta) \end{cases} \quad (62)$$

where u_{α} is the α component of the displacement vector \vec{u} and x_{α} is a component of the position vector²³. Both \vec{u} and \vec{x} are defined with respect to a unit cell within the lattice, so the $e_{\alpha\beta}$ terms quantify the relative amounts by which the unit cells are distorted from their unstrained positions in the various dimensions of the cell.

As with the spin-orbit Hamiltonian, the strain Hamiltonian (H_{strain}) will be added to the existing Hamiltonian to arrive at the total Hamiltonian

$$H_{\text{total}} = H_0 + H_{k \cdot p} + H_{so} + H_{\text{strain}}. \quad (63)$$

The eigenvalues of H_{total} , $E = E_{\lambda}(\mathbf{k})$, form 3 subbands (labeled by $\lambda = \text{HH, LH, and SO}$) that are each doubly degenerate and are distinct at zone center. These eigenvalues will be used throughout the rest of this work to describe the dispersion relations in the bulk solid.

The total Hamiltonian now consists of three terms, all of which are expressed as matrix representations in the $|j, m_j\rangle$ basis:

- (1) the contribution from $H' = H_0 + H_{k \cdot p}$,
- (2) a term that introduces the spin-orbit correction, H_{so} , and
- (3) a refinement to include the effects of strain on the total Hamiltonian, H_{strain} .

All of the above terms are added to obtain the final form of the Hamiltonian (for the current study), H_{total} . The band structures resulting from the inclusion of these terms are shown in figures II-1 through II-3. Figure II-1 shows the eigenvalues of the Hamiltonian

$H=H_0+H_{kp}$, the eigenvalues of $H=H_0+H_{kp}+H_{so}$ are shown in figure II-2, and figure II-3 presents the eigenvalues of H_{total} .

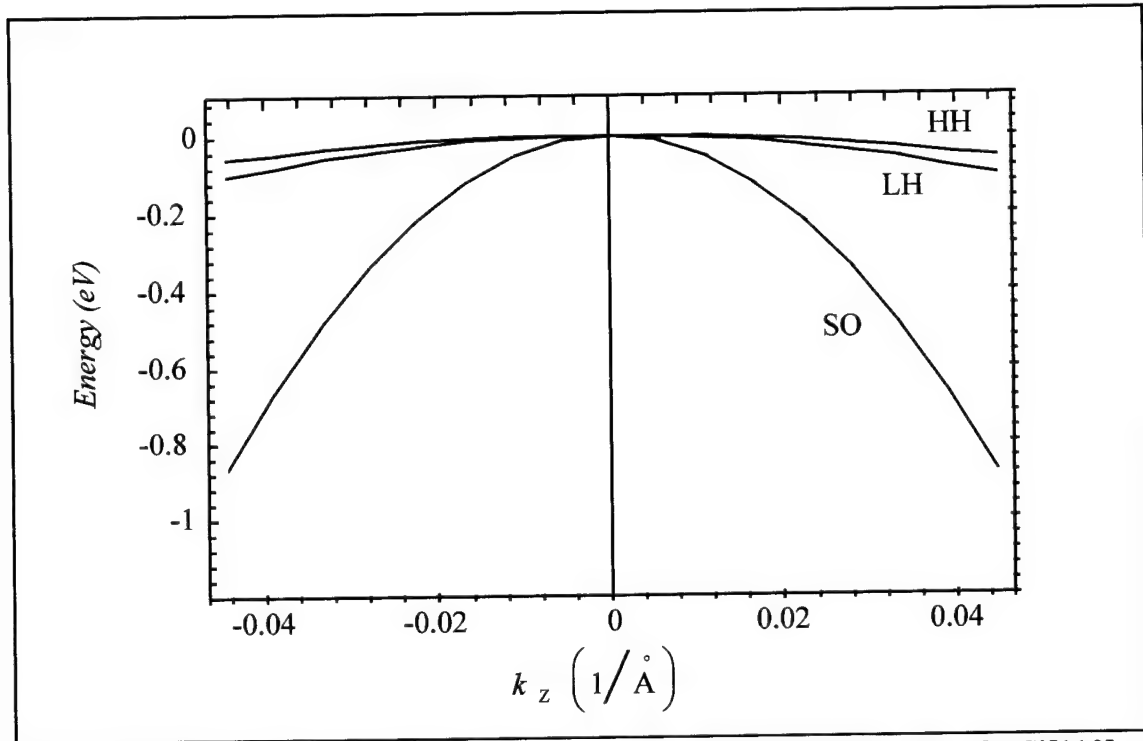


Figure II-1. Energy subbands formed from the eigenvalues of $H=H_0+H_{kp}$ for Si[110], $x=0.30$. Subbands are all degenerate at zone center.

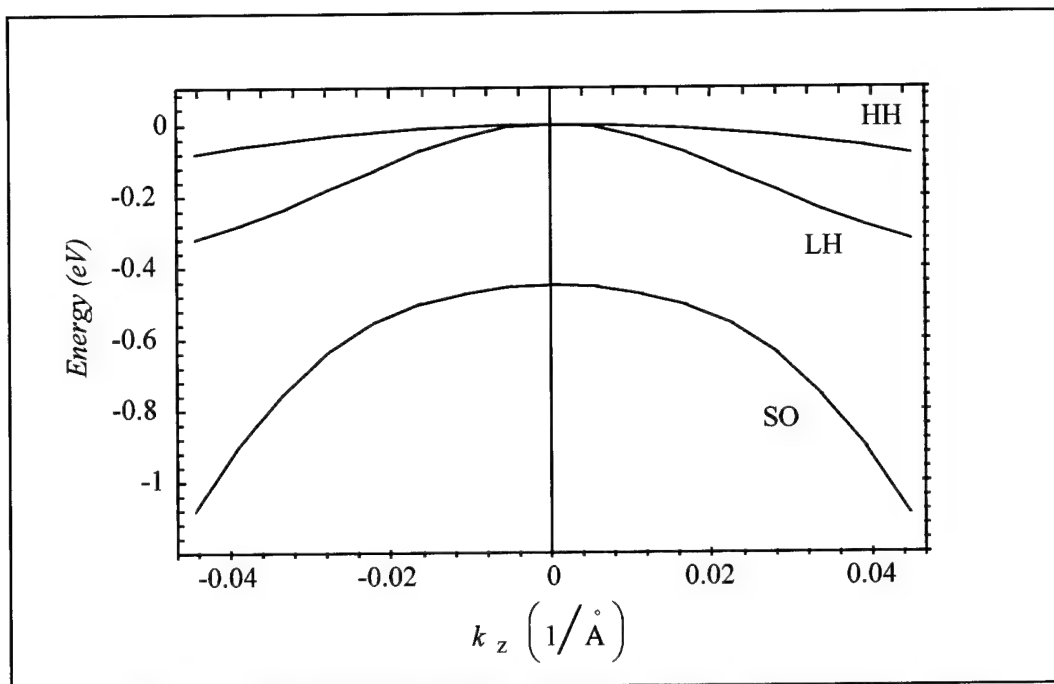


Figure II-2. Energy subbands formed from the eigenvalues of $H=H_0+H_{kp}+H_{so}$ for Si[110], $x=0.30$. The zone center degeneracy has been partially lifted by the spin-orbit correction.

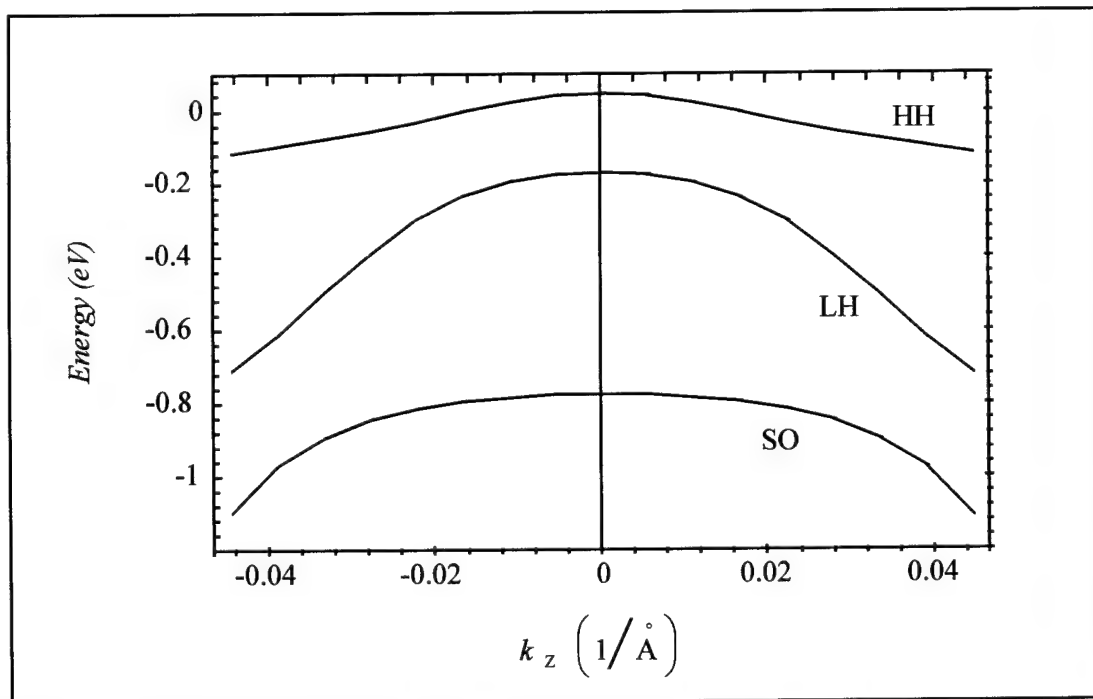


Figure II-3. Energy bands formed from the eigenvalues of $H=H'+H_{so}+H_{strain}$ for Si[110], $x=0.30$. Subbands are all distinct.

Section C. Envelope Function Approximation and Boundary Value Problem

Overview of the Envelope Function Approximation.

The Envelope Function Approximation (EFA) involves forming a linear combination of the plane waves corresponding to each bulk Hamiltonian subband (having the characteristic value of k_z that derives from the energy value of the subband for a particular $k_{||}$). Subband weights, $w_{N,v}(k_{||})$, quantifies the relative contribution of each subband at a particular value of $k_{||}$. The EFA wavefunctions are given by²

$$|N, k_{||}\rangle = \sum_{v=1}^6 \sum_{k_z} F_v(N k_{||}, k_z) \cdot |v, \mathbf{k}\rangle, \quad (64)$$

where v is an index which runs through the $|j, m_j\rangle$ basis states, N is a subband index that labels the EFA bound states, $k_{||}$ is the wave vector in the plane of the well, and k_z is the wave vector normal to the well. The summation over k_z includes all of the subbands in the bulk material. The boundary conditions at the barrier-well heterojunction and the bulk barrier and well eigenstates are used to determine the values of the expansion coefficients $w_{N,v}(k_{||}) \equiv \sum_v F_v(N k_{||}, k_z)$, where N is the subband index and v is the same index as in equation 64.

More details for calculating the $|N k_{||}\rangle$ via the use of the quantum well boundary conditions, are given by M. Gregg²⁰ or F. Szmulowicz et al³. Mathematica programs provided by M. Gregg calculate the EFA wavefunctions used in this thesis.

The EFA wavefunctions then can be thought of simply as linear combinations of the bulk eigenfunctions that satisfy the boundary conditions at the well edges. These values determine the composition of each of the EFA eigenfunctions in terms of the constituent bulk eigenfunctions. The composition of the EFA energy subbands will be seen to be important because of the effect this will have on intersubband transition strengths and the corresponding absorption coefficients. The dispersion relations resulting from these EFA calculations for a specific case are shown in figure II-4.

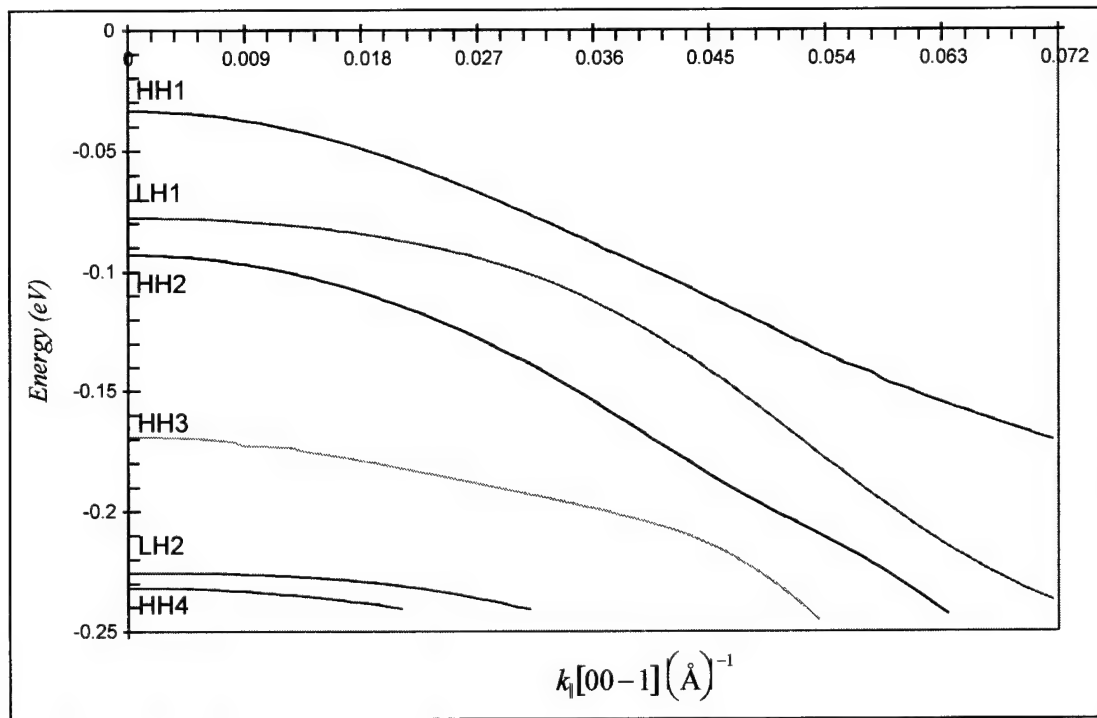


Figure II-4. Dispersion Relations for the [110] substrate orientation, 30 Å well width, and 30% Ge composition (k_{\parallel} is in the k_x direction).

The label given to an EFA energy subband corresponds to which of the bulk eigenfunctions make the largest contribution to the EFA eigenfunction at zone center.

The bandweights, $w_{N,\sqrt{k_{\parallel}}}$, vary with k_{\parallel} and thus a subband that is predominantly heavy

hole like at zone center may become a predominantly light hole or split off hole subband away from zone center. Therefore, to avoid confusion the subband label is determined by the subband makeup at zone center. The bandweights for the HH1 subband of figure II-4 are shown in figures II-5 and II-6. Figure II-5 plots the 6 $w_{N,\nu}(k_{||})$ values corresponding all of the degenerate bulk eigenfunctions, and figure II-6 shows the heavy, light, and split-off band weights (formed from summing the appropriate $w_{N,\nu}(k_{||})$). The areas in figures II-5 and II-6 where the bandweights are not smoothly varying functions are areas of numerical instability, which will be discussed more fully in a following section. An important point illustrated by these figures is that the subbands have mixed character at zone center in the [110] substrate orientation, whereas the subbands are predominantly composed of a single type at zone center for [001] orientations.

The band weights shown in figures II-5 and II-6 are normalized to unity,

$$\langle Nk_{||} | Nk_{||} \rangle = \sum_{\nu=1}^6 w_{N,\nu}(k_{||}) = 1. \quad (65)$$

The band weight plots (II-5 and II-6) illustrate that there are significant contributions to the EFA energy subband from all three bulk energy subbands for the [110] substrate orientation throughout the range of $k_{||}$.

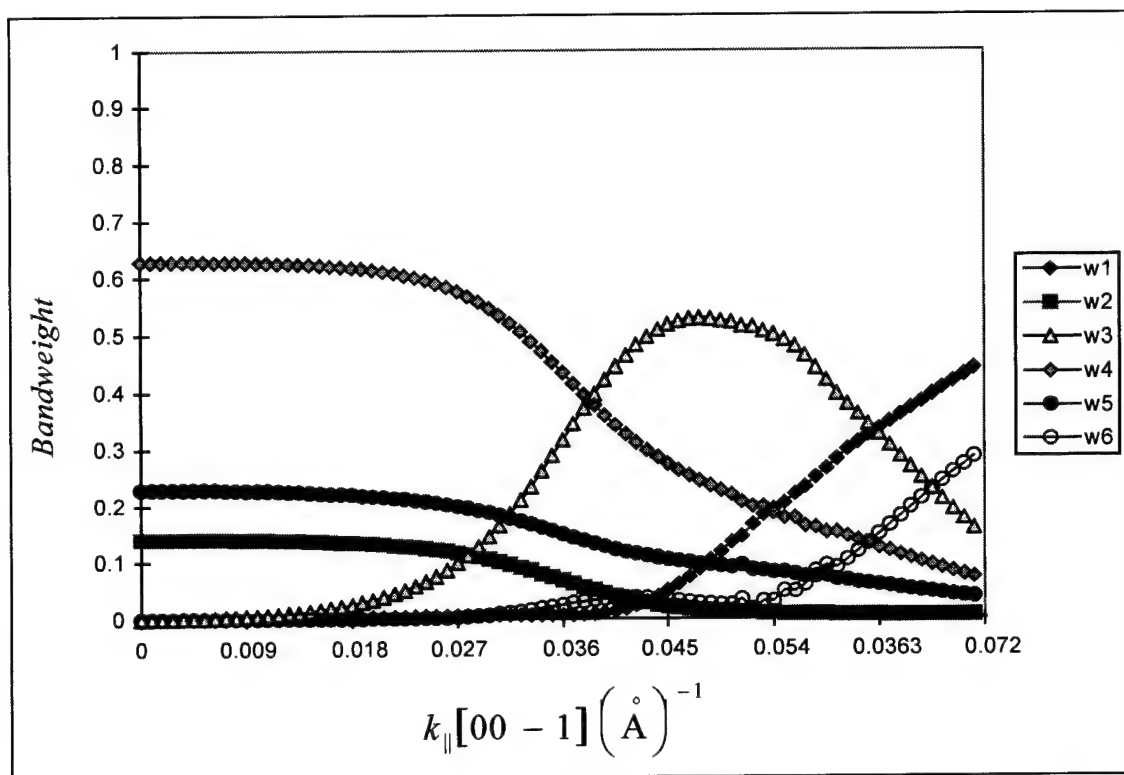


Figure II-5. HH1 subband w_i 's vs k_{\parallel} for the $[110]$ substrate orientation, 30 Å well width, and 30% Ge composition (k_{\parallel} is in the k_x direction).

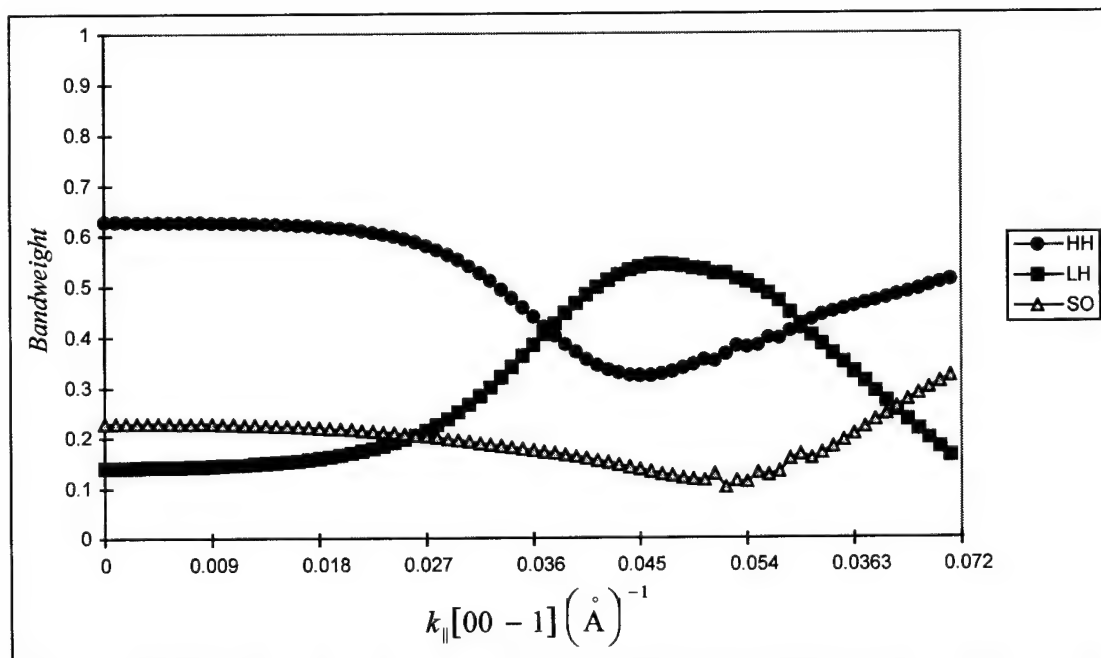


Figure II-6. HH1 bandweights vs k_{\parallel} for the $[110]$ substrate orientation, 30 Å well width, and 30% Ge composition (k_{\parallel} is in the k_x direction).

Numerical Difficulties in the Determination of the MQW Band Structure

Band structures along k space directions that do not fall along an axis of symmetry such as $k[001]$ or $k[00-1]$ tend to be difficult to determine computationally. The reason for this difficulty is that the method used to determine EFA energy subband values is to compute the determinant of a 12×12 matrix that arises from the boundary conditions in the EFA approach and find the value of E which sets this determinant to zero, utilizing the *FindRoot* utility in *Mathematica*. The weakness of this approach is that any inaccuracy in computing the elements of the 12×12 matrix will be greatly magnified in the process of calculating the determinant.

While the energy eigenvalues resulting from this process are acceptable along the $[00-1]$ direction, where the 12×12 matrix is sparsely populated due to the fact that k_y is constrained to be zero, the process becomes more unstable when applied along directions between $[00-1]$ and $[-110]$. Energy eigenvalues for this direction showed large regions of instability, especially away from zone center. This is illustrated in figure II-7.

Many instances of false subband structures and spurious roots were found in the vicinity of the correct energy subbands. In every case, these false solutions would merge with the stable subband structure soon after they appeared. Unfortunately, at the point where the spurious roots diverge from the valid roots, the root finder would tend to become unstable and track both solutions alternately. The false roots in these regions of instability were confined to regions near the valid eigenvalues. This instability is illustrated in figure II-8.

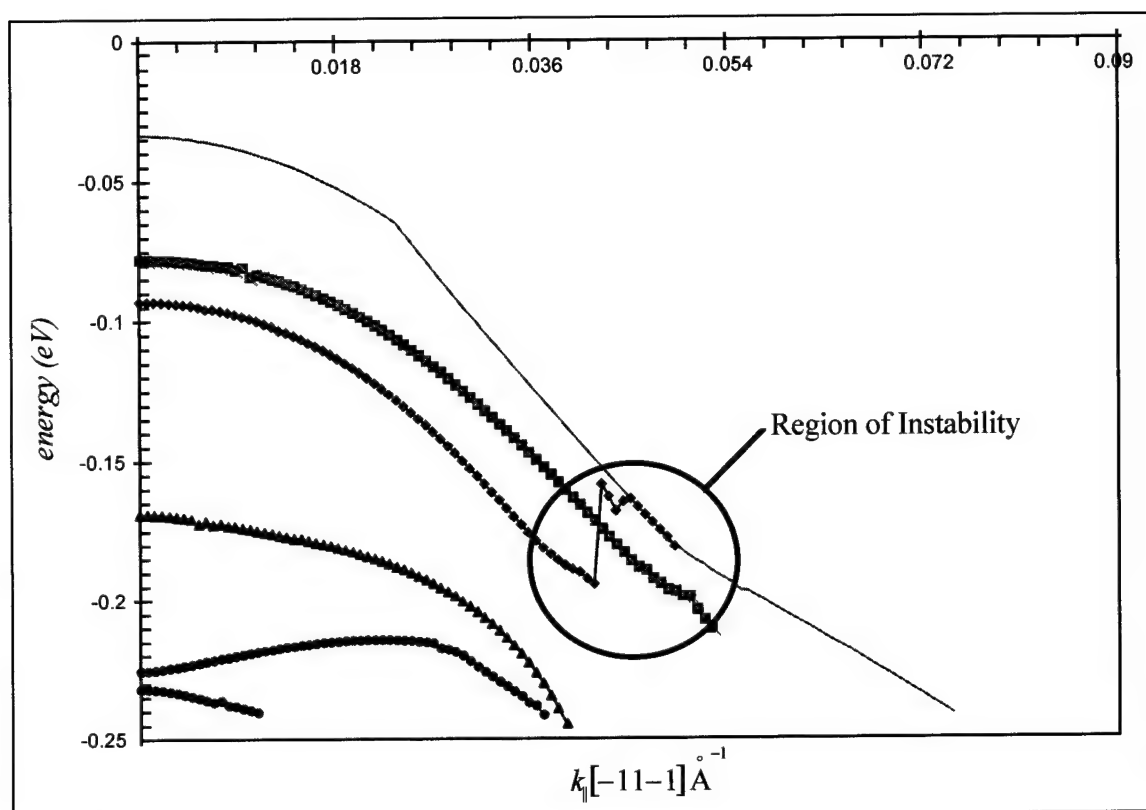


Figure II-7. Band structure of a 30 Å / 30% Ge quantum well structure in a direction 45° between k_x and k_y showing an enlarged instability region. Symbols indicate locations of discrete data points produced by the calculations. The top subband symbols are not shown to emphasize that the third subband solution incorrectly collapses to the values of the top subband.

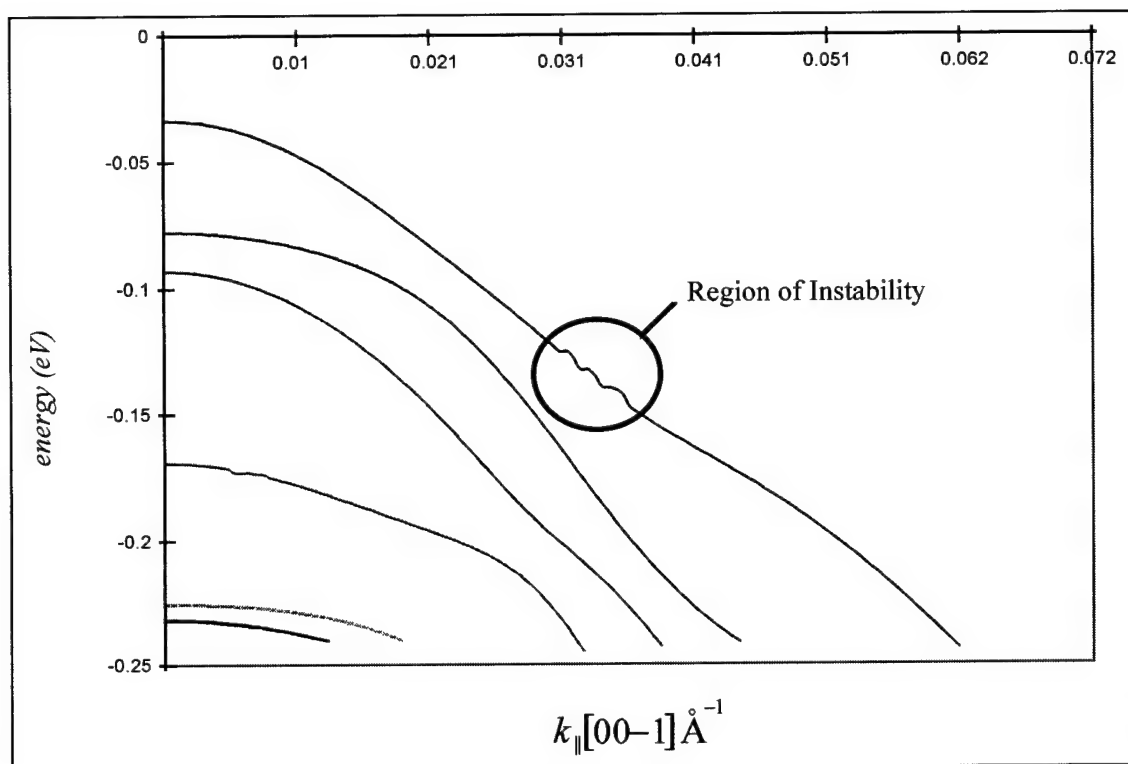


Figure II-8. Band structure of a 30 Å / 30% Ge quantum well structure in the k_x direction showing instability region.

Instability in the band structure is not always evident through visual examination of the band structure plots. In many cases, the scale of the instability is small enough that fluctuations occur on the order of 1 part in 1000 (on the order of 10^{-4} eV). This is not enough instability to become apparent with the subband calculations themselves, but it will become more pronounced when the energy eigenvalues are used in calculations such as band weight and momentum matrix element calculations that are more sensitive to fluctuations in the eigenstates. An example of the discontinuities in the bandweights for the k_x direction, shown in figure II-9, displays the isolated nature of the instability when the $k[00-1]$ direction is considered. Figure II-10 shows the instabilities in the bandweights

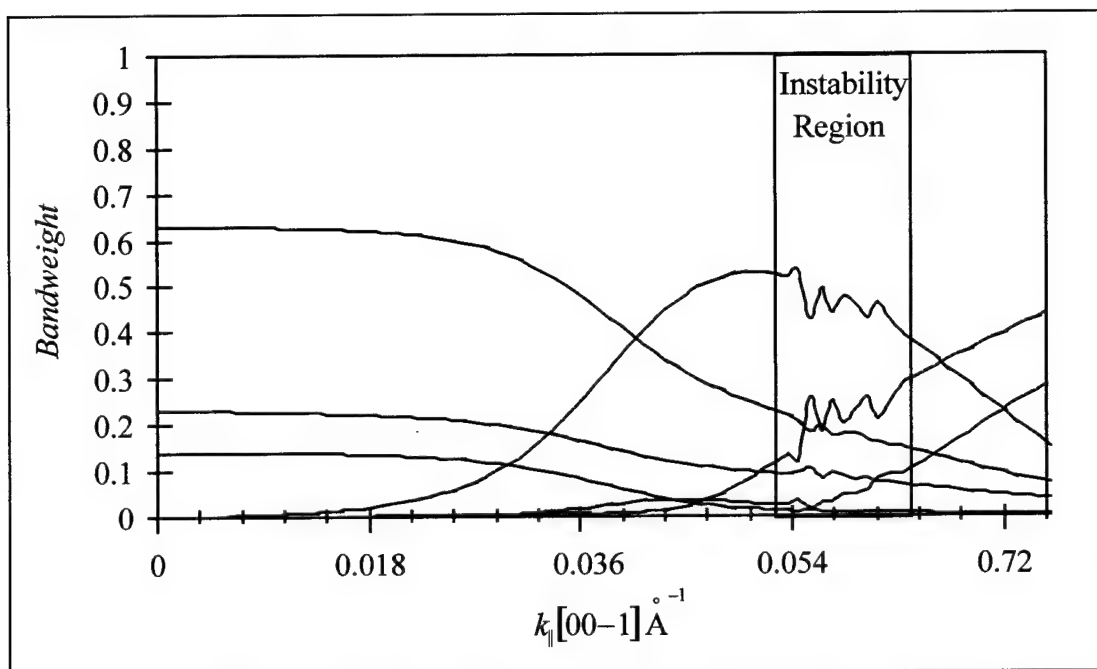


Figure II-9. Bandweights w_i for the HH1 subband of the 30 Å / 30% Ge quantum well in the k_x direction, showing the smoothness of the bandweights outside of the instability region identified in figure II-7.

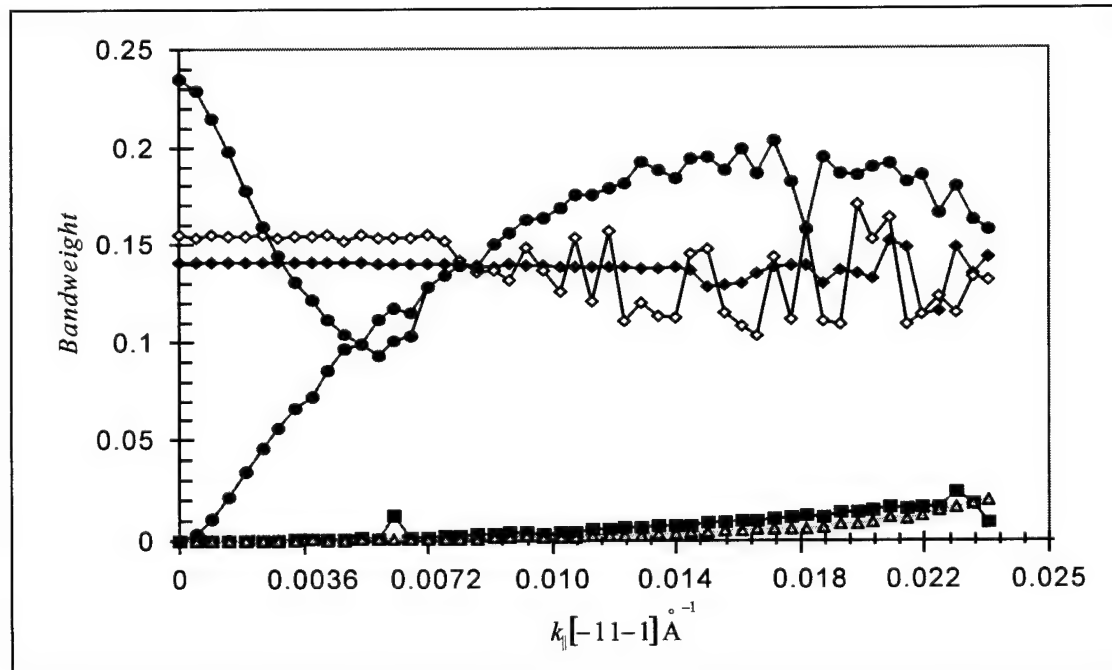


Figure II-10. Bandweights w_i for the LH1 subband of the 30 Å / 30% Ge quantum well for 45° between the k_x and k_y directions, showing the instability in the bandweights throughout the range of $k_{||}$.

throughout the range of $k_{||}$ for the $[-11-1]$ direction. Note that the instabilities in figure II-10 are much more widespread.

The methodology for treating the problem of band structure instability was to trace the valid solutions back to where the solution bifurcated, which often resulted in the root finder following only the correct solutions. When a large number was inserted into the 12×12 matrix before the determinant was taken, the value of the determinant could also be used to determine the validity of the root, as spurious roots tended to have much larger values of the determinant at the specified energy value than the valid roots.

The methods of the previous paragraph discarded the majority of the false roots and the remaining spurious roots were found to be localized and were not far removed from the true roots. The nature of the error in the roots is determined by examining the calculated band weights. Errors that caused isolated instabilities in the band weights and momentum matrix elements were corrected by hand to obtain smoothly varying momentum matrix elements.

It is apparent from figures II-7 through II-10 that the subbands are far less stable off of the k_x axis. This instability also manifests itself in the momentum matrix elements, which are used directly in the absorption coefficient calculations. For this reason, the subbands used for all of the calculations in this thesis were along the k_x direction and localized regions of instability were corrected by hand. The smoothed band structure is shown in figure II-11.

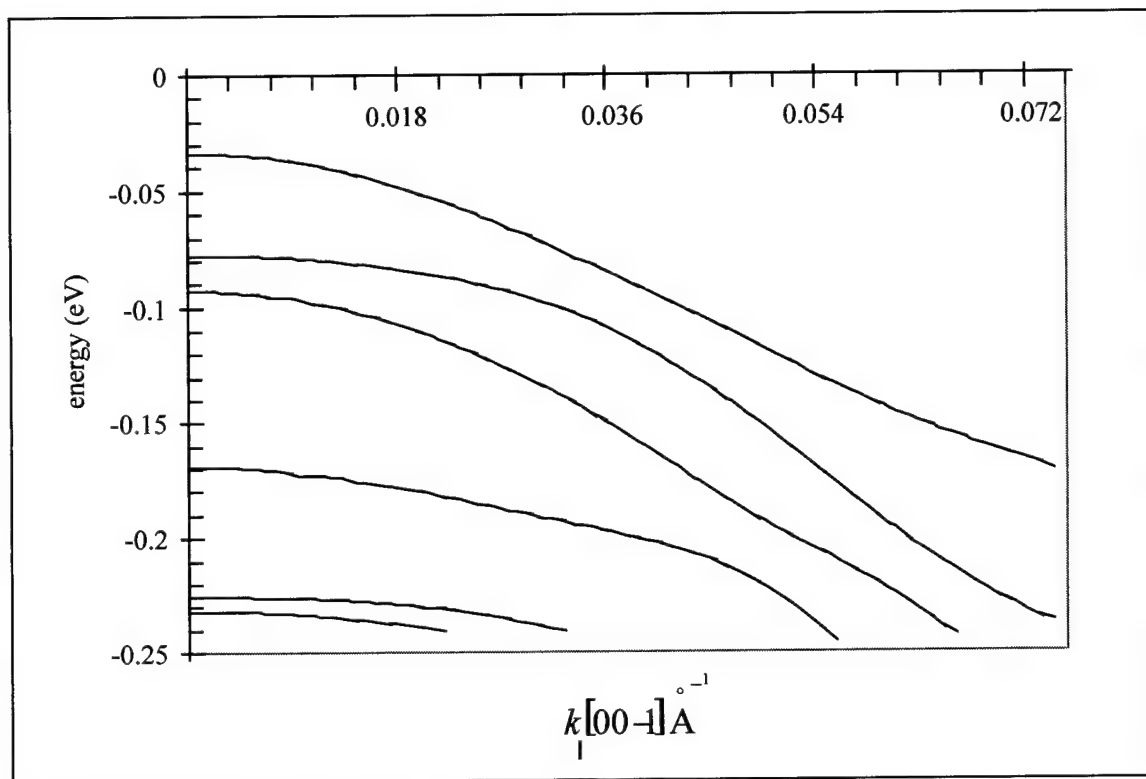


Figure II-11. Smoothed plot of the band structure of a 30 Å / 30% Ge quantum well structure in the k_x direction.

Section D. Calculations of Linear Absorption Coefficients

Subband Occupation Levels.

The subbands represented in figure II-11 are solutions of the eigenvalue equation as determined by the boundary conditions at the barrier-well heterojunction. As such, they are values of energy at which a bound state *may* exist. Several factors will determine if a particular state is in fact occupied by a hole (ie, not occupied by an electron): temperature, doping levels, and the form of the band structure.

The temperature will determine the occupation of a subband via the Fermi-Dirac

distribution function,

$$N(\epsilon)d\epsilon = f(\epsilon)g(\epsilon)d\epsilon = \frac{g(\epsilon)d\epsilon}{1 + e^{(\epsilon - \epsilon_f)/kT}}, \quad (66)$$

where ϵ is energy and $g(\epsilon)$ is the density of states. This yields a occupation value for the band structure as a function of energy. In the present case it is assumed that temperatures involved are low enough that the Fermi-Dirac distribution function may be approximated by a step function. This implies that all states with energies lower than the Fermi energy are completely occupied, and higher lying states are completely vacant. This assumption will become important because transitions may only be made between occupied and unoccupied states, at a single value of $k_{||}$, as phonon assisted transitions will not be considered. The nature of the Fermi-Dirac distribution function is shown in figure II-12.

It is apparent from figure II-12 that the approximation of the Fermi-Dirac distribution function with a step function is acceptable at low temperatures (0-77 K) but may introduce some inaccuracies as room temperature is approached. The experimental data which is to be compared against the results of this project falls within this low temperature regime.

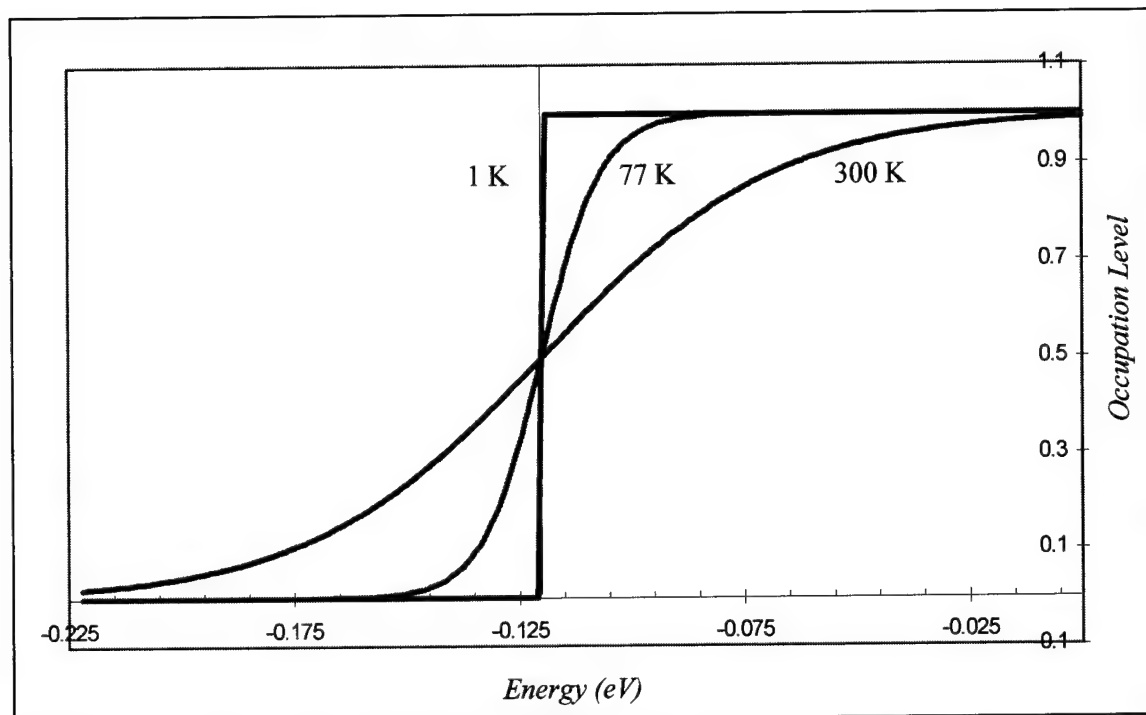


Figure II-12. Fermi-Dirac distribution function for a Fermi energy of -0.12 eV, at temperatures of 1 K, 77 K, and 300 K. Chemical potential not assumed to be a function of temperature.

Determination of the Density of States (DOS).

It is necessary to determine the density of states values using the quantum well band structure in order to determine the fermi energy and the resulting occupation profiles for each subband. The assumption is made that all of the dopant atoms are completely ionized and thus the fermi level will be fixed at the energy where the integrated density of states (integrated over the energy) is equal to the number of dopant atoms. The first step in determining the fermi level is the determination of the density of states $g(\varepsilon)$.

The density of states can be defined in terms of either energy or \mathbf{k} , and is given by

$$g(\varepsilon)d\varepsilon = g(k_{\parallel})dk_{\parallel}$$

$$g(\varepsilon) = \frac{k_0}{\left(\frac{d\varepsilon}{dk}\right)\bigg|_{k=k_0}} \quad (67)$$

where k_0 is the value of k_{\parallel} where the derivative of the energy subband is to be evaluated.

When multiple subbands are considered for the DOS calculation, the total DOS ($g(\varepsilon)$) for a particular value of ε is calculated by summing the contributions from all of the subbands that span that ε value

$$g(\varepsilon) = \sum_v \frac{k_0^v}{\left(\frac{d\varepsilon}{dk}\right)\bigg|_{k=k_0^v}}, \quad (68)$$

where v is an index running over all of the subbands that intersect the value of energy (ε), and k_0^v is the value of k_{\parallel} where the v th subband has the energy value ε . As an example, for the band structure shown in figure II-11, the HH1 subband contributes to the DOS between energies of approximately -0.0335 eV and -0.24 eV, the LH1 subband contributes between -0.079 eV and -0.24 eV, and the HH2 subband contributes between -0.092 eV and -0.24 eV. The -0.24 eV energy cutoff is the well depth for this particular well.

Since the energy subbands are flat at zone center, the density of states must go to infinity whenever the value of energy used in $g(E)$ coincides with the top of a subband. This behavior is known as a *Van Hove singularity*, and is expected when calculating the density of states. A plot of the density of states is shown in figure II-13 for a typical case.

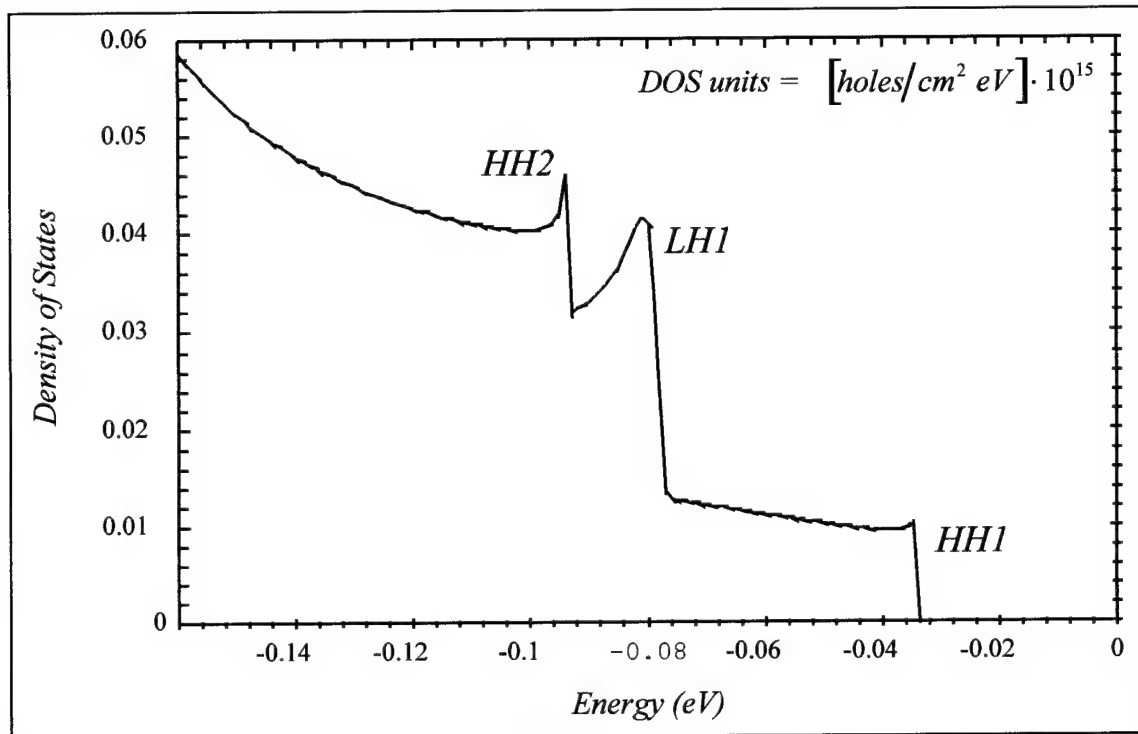


Figure II-13. Density of states vs energy, [110] substrate orientation, $L = 30 \text{ \AA}$, 30% Ge. Van Hove singularities at the energy values where HH1, LH1, and HH2 subband edges occur do not go to infinity due to numerical reasons.

The contribution of each of the energy subbands (HH1, LH1, and HH2), as well as the appearance of the Van Hove singularities at the top of each subband, is shown in figure II-13. The addition of each subband creates the step-function like increase bearing the subband's label. The density of states can be calculated down to an energy equal to the well depth, including all of the subbands; however, this is not necessary since it will be shown that the integrated density of states will equal the maximum number of holes well above the point where the HH3 subband begins.

Once the density of states as a function of energy is calculated, it must be integrated over the range of energies under investigation. This integration will yield the total number of available states at each energy value, shown in figure II-14.

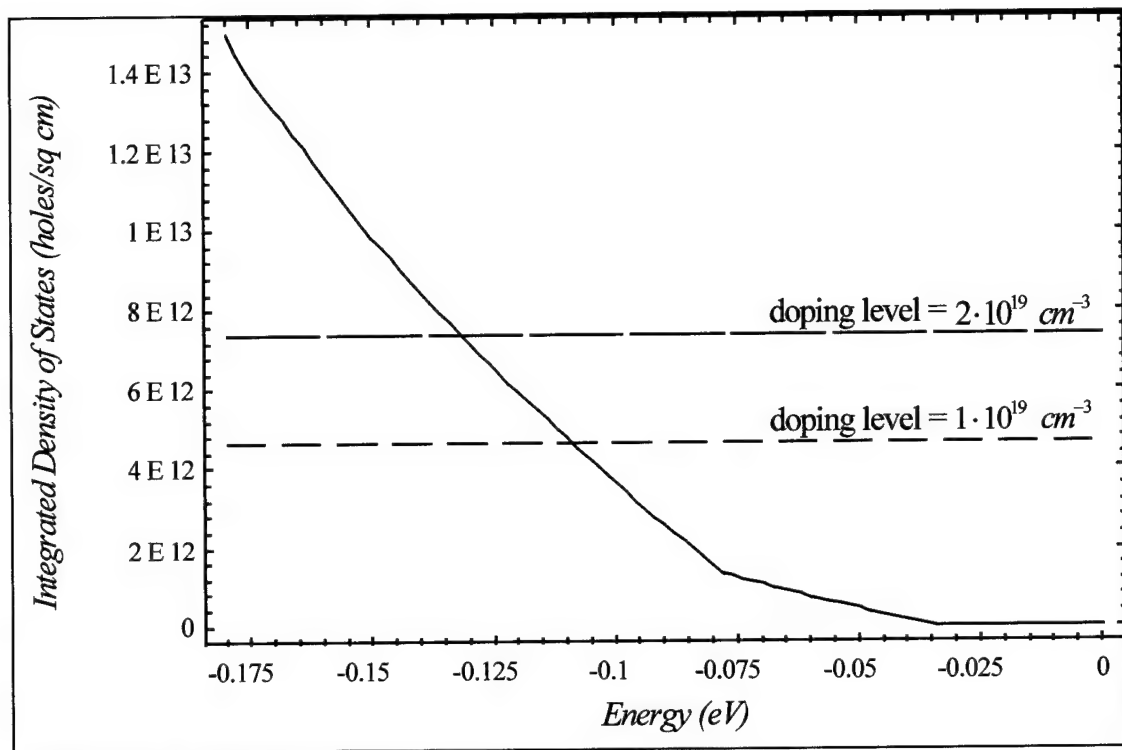


Figure II-14. Integrated density of states for [110] substrate, $L=30 \text{ \AA}$, 30% Ge composition. Total numbers of dopant holes are shown for two doping levels.

The points where the total number of dopant holes equals the integrated density of states are the Fermi levels for the applicable doping level. The assumption is made that below this energy all states are occupied and above this energy no states are populated. This value of energy corresponds to a different value of $k_{||}$ for each of the partially occupied subbands. This value of $k_{||}$ is the point at which the subband ceases to be populated, and is important in determining whether transitions will be made from the subband or to the subband, since transitions must originate in an occupied region of a subband and fill an unoccupied state in another subband. With wavefunctions, band structure, density of states values and Fermi levels calculated, it is possible to compute the

transition strengths between valence subbands and the corresponding absorption coefficients.

Calculation of Inter-subband Momentum Matrix Elements.

The derivation of the absorption coefficient for a system of one electron atoms interacting with a weak field is given by Bransden and Joachain³¹. An outline of the derivation is provided here to provide some insight into the source of the relationship between the momentum matrix elements and the absorption coefficients.

In the presence of electromagnetic radiation, the kinetic energy term of the Hamiltonian is modified as

$$\frac{p^2}{2m} \Rightarrow \frac{1}{2m}(\mathbf{p} - q\mathbf{A})^2 \quad (69)$$

where q is the charge of the particle and \mathbf{A} is the vector potential of the incident field. In the time dependent Schrödinger equation,

$$i\hbar \frac{\partial}{\partial t} \Psi(\mathbf{r}, t) = H \Psi(\mathbf{r}, t) \quad (70)$$

a new term will appear from the addition of the vector potential interaction,

$$i\hbar \frac{\partial}{\partial t} \Psi(\mathbf{r}, t) = \left(H_0 - \frac{i\hbar q}{m} \mathbf{A} \cdot \nabla + \frac{q^2}{2m} A^2 \right) \Psi(\mathbf{r}, t) \quad (71)$$

where H_0 is the Hamiltonian of equation 63. In the weak field approximation, the A^2 term is neglected and the $\mathbf{A} \cdot \nabla$ term is treated. Schrödinger's equation becomes,

$$i\hbar \frac{\partial}{\partial t} \Psi(\mathbf{r}, t) = \left(H_0 - \frac{i\hbar q}{m} \mathbf{A} \cdot \mathbf{P} \right) \Psi(\mathbf{r}, t), \quad (72)$$

and is solved using standard time dependent perturbation theory³¹, where the probability amplitude of the system to be in a state $|\Psi_b\rangle$ is given by

$$\begin{aligned} M_{Nk_{\parallel}, Mk_{\parallel}} &= \langle Nk_{\parallel} | e^{i\mathbf{k}\cdot\mathbf{r}} \hat{\varepsilon} \cdot \nabla | Mk_{\parallel} \rangle \\ &= \int \Psi_{Nk_{\parallel}}^*(\mathbf{r}) e^{i\mathbf{k}\cdot\mathbf{r}} \hat{\varepsilon} \cdot \nabla \Psi_{Mk_{\parallel}}^*(\mathbf{r}) d\mathbf{r} \end{aligned} \quad (73)$$

In equation 73, Mk_{\parallel} and Nk_{\parallel} are the final and initial states of the particle and ε is the polarization vector of the incident radiation. The transition rate for absorption is defined as the time derivative of the square of the probability of being in the state $|\Psi_b\rangle$, which is a function of M_{ba} . The absorption cross section is proportional to the transition rate and thus is proportional to $|M_{ba}|^2$.

The inter-subband momentum matrix elements are given by Szmulowicz as

$$\begin{aligned} \langle Nk_{\parallel} | \frac{\hbar}{m} \vec{\varepsilon} \cdot \vec{p} | Mk_{\parallel} \rangle &= \left(\frac{\hbar^2}{m} \right) \hat{\varepsilon} \cdot \sum_{vv'} \left\{ \int F_{N,v}^* P_{vv'} F_{M,v'} dz \right. \\ &\quad + \frac{1}{2} \int \left(-i \frac{d}{dz} (F_{N,v}) \right)^* Q_{vv'} F_{M,v'} dz \\ &\quad \left. + \frac{1}{2} \int F_{N,v}^* Q_{vv'} \left(-i \frac{d}{dz} (F_{M,v'}) \right) dz \right\} \end{aligned} \quad (74)$$

where

$$F_{N,v} = F_v(N k_{\parallel}, z), \quad (75)$$

is the v th component of the envelope function in the coordinate representation. The matrices P and Q are given by 6x6 matrices that are dependent upon both the substrate orientation and the polarization of the incident radiation²⁰.

The first integral of equation 74 is the overlap integral for direct coupling of like states such as HH- HH or LH-LH. The second and third integrals are the dipole coupling terms which couple dissimilar states, such as for LH-HH or HH-LH transitions. Since the subbands in the EFA are mixed the Q matrix elements will couple the various dissimilar components and the P matrix elements will couple the like state components, allowing strong transitions between states that would not be coupled as strongly for non-mixed subbands.

A plot of the momentum matrix elements as a function of $k_{||}$ is shown in figure II-15. The P_x momentum matrix elements for transitions from the HH1 subband are shown as an example of the form of the momentum matrix elements. Momentum matrix elements are calculated for P_x , P_y , and P_z components for transitions from all populated subbands and these results will be presented in Chapter III.

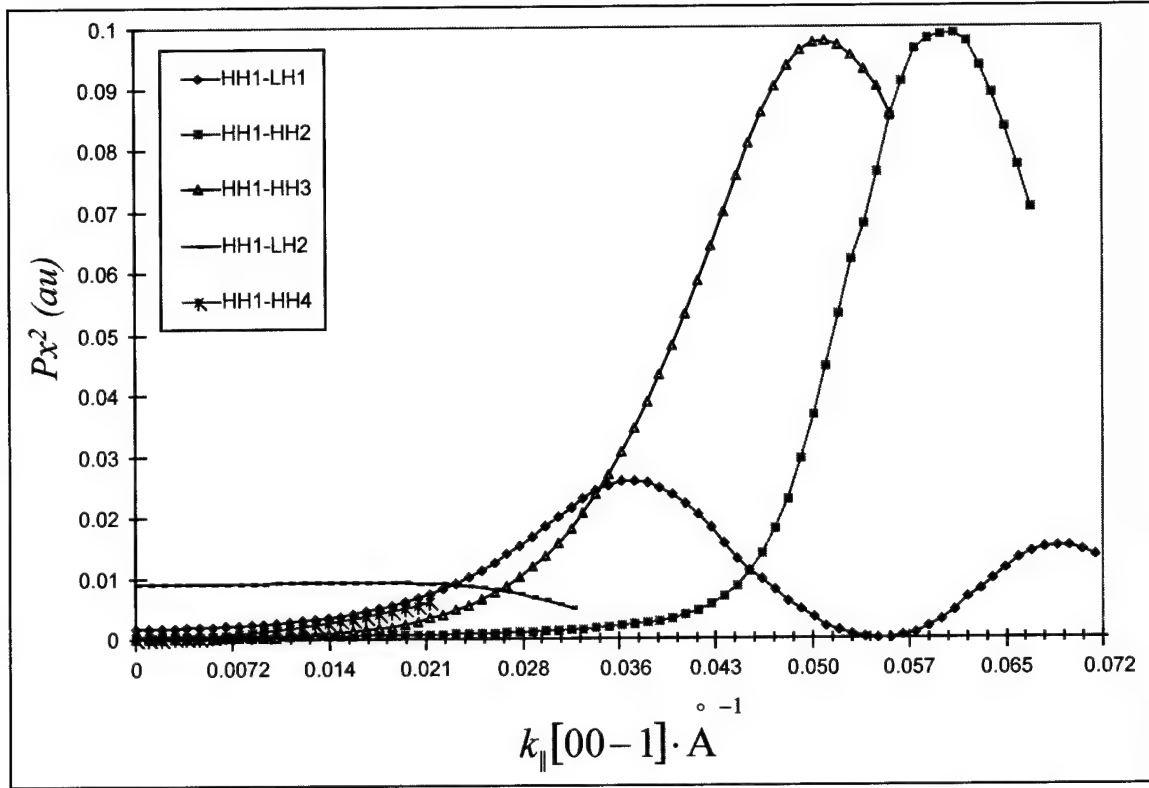


Figure II-15. P_x momentum matrix elements squared for transitions from the HH1 subband to higher levels for the Si[110]/ 30 Å / 30% Ge case.

Bound to Bound Absorption Coefficients.

With the momentum matrix elements, fermi levels, and energy band structure calculated, all of the elements required to perform the calculation of the absorption coefficient are present. The form of the linear absorption coefficient is given by Bastard³² as

$$\alpha(\omega) = \frac{4\pi e^2}{ncm_0\omega\Omega} \sum_{i,f} \frac{1}{m_0} \left| \hat{\epsilon} \cdot \vec{P}_{i,f} \right|^2 \delta(E_f - E_i - \hbar\omega) \times [f(E_i) - f(E_f)] \quad (76)$$

where Ω is the characteristic volume suitable to the problem (which will be replaced with the dimension of the well, L , the only length present in the problem), $\hat{\epsilon}$ is the polarization vector, $f(E)$ is the fermi occupation factor for a subband at energy E (not including the density of states), and $\vec{P}_{i,f} = P_x^{i,f} \hat{x} + P_y^{i,f} \hat{y} + P_z^{i,f} \hat{z}$ is the momentum vector for the transition between states i and f which is formed from the momentum matrix elements derived earlier.

Equation 76 is re-expressed by Szmulcowicz³ as

$$\alpha(\omega) = \frac{e^2}{n c m_0^2 \omega L} \cdot \int dk_{\parallel} \sum_{N,M} \left| \hat{\epsilon} \cdot \vec{P}_{NM}(k_{\parallel}) \right|^2 \delta(E_N(k_{\parallel}) - E_M(k_{\parallel}) - \hbar\omega) \quad (77)$$

where the subscripts N and M denote final and initial states, and the fermi factors are treated step functions and are not written out explicitly. The general form of the delta function is given by

$$\delta(f(x)) = \frac{\delta(x - x_0)}{\left(\frac{df(x)}{dx} \right)}, \quad (78)$$

in one dimension, which is used to re-express equation 77 (in three dimensions) as

$$\alpha(\omega) = \frac{2\pi e^2}{n c m_0^2 \omega L} \sum_{N,M} \frac{k_0 \left| \hat{\epsilon} \cdot \vec{P}_{NM}(k_0) \right|^2}{\left| \nabla(E_N - E_M) \right|}. \quad (79)$$

The factor of 2π in the numerator of equation 79 results from the azimuthal integral in k_{\parallel} space and the assumption that the transition probability is isotropic throughout a 2π rotation in k_{\parallel} space. The variable k_0 appearing in equation 79 is the value of k_{\parallel} that satisfies the delta function of equation 77.

Equation 77 must be evaluated only over the appropriate regions in k space where the initial state lies within a populated region of a subband and the final state lies in the unpopulated region of a higher lying subband. As each value of ω is examined, all possible transitions of energy $\Delta E = \hbar\omega$ must be identified and checked to insure that occupation levels of the subbands allow a transition. The value of $|\nabla(E_N - E_M)|$ must be calculated for every value of ΔE that is defined for the given ground and excited subbands. This process is accomplished by determining ΔE and $|\nabla(E_N - E_M)|$ as functions of $k_{||}$, and stepping over the values of $k_{||}$ corresponding to a populated ground state subband and an unpopulated excited state subband. The value of α must be calculated using the correct value of the momentum matrix element for the value of $k_{||}$ where ΔE occurs. The values of α for each ground-excited subband pair for each value of ΔE are summed to produce a value for $\alpha(\Delta E)$. A plot of $\alpha(E)$ is shown in figure II-16 for a pure \hat{z} polarization state.

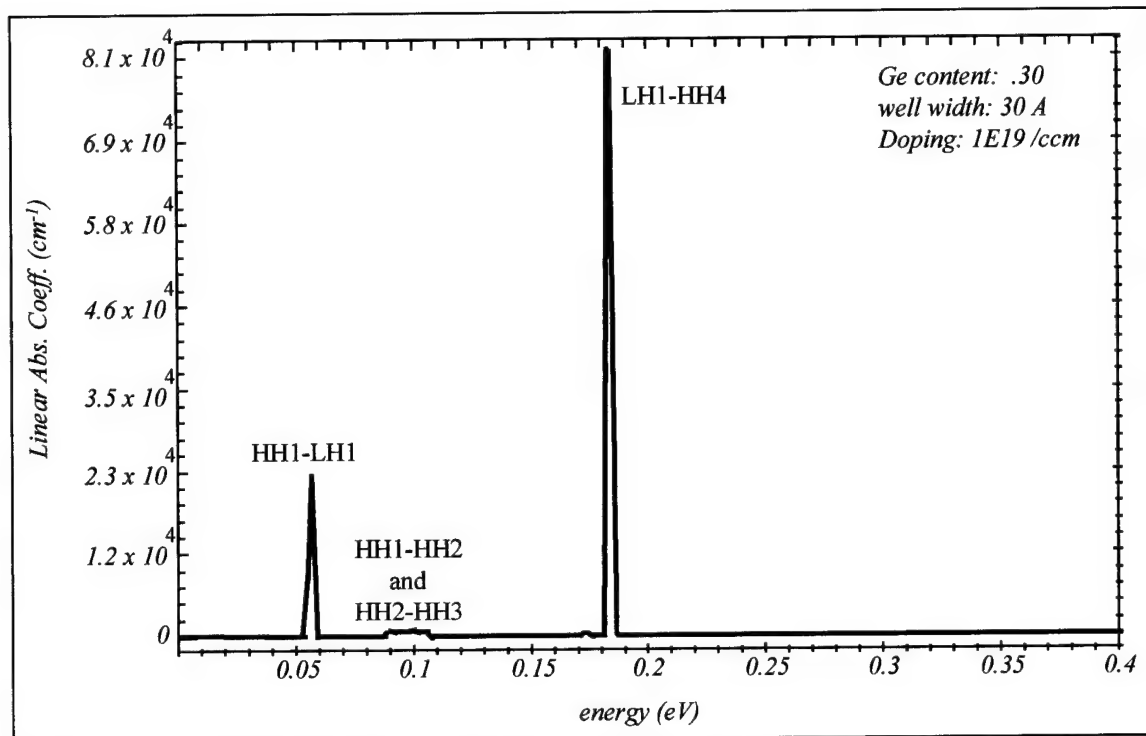


Figure II-16. Linear absorption coefficient vs energy (eV) for pure z polarization. No magnification of smaller peaks is performed. Absorption coefficients shown are obtained using the formula of equation 79.

An alternate method of calculating absorption coefficients arises by replacing the delta function in equation with the familiar Lorentzian distribution common in lifetime broadening approximations,

$$L(E) = \frac{\Delta E}{2\pi \left[(E - \Delta E_{NM})^2 + (\Delta E)^2 \right]} \quad (80)$$

where ΔE in this case is the FWHM of the energy spread around ΔE_{NM} , the energy difference between energy levels. When equation 80 is recast in a form applicable to the MQW problem, it becomes³⁰

$$L_{NM}(\omega, k_{\parallel}) = \frac{(\Gamma_{NM}(k_{\parallel})/2)}{\left[\left(E_N(k_{\parallel}) - E_M(k_{\parallel}) - \hbar\omega \right)^2 + \left(\Gamma_{NM}(k_{\parallel})/2 \right)^2 \right]} \quad (81)$$

which will remove the singularities inherent in the delta function approach, replacing them with a more physically meaningful line broadened behavior. In equation 81, $\Gamma_{NM}(k_{\parallel})$ is a line width parameter equal to the average scattering rate for the states $|Nk_{\parallel}\rangle$ and $|Mk_{\parallel}\rangle$ in the well². The value of $\Gamma_{NM}(k_{\parallel})$ for the GaAs/Al_xGa_{1-x}As system is reported by Chang and James² as a function that increases with energy and shows a step-like increase for each of the subbands. As an approximation to this behavior, a single value of $\Gamma_{NM}(k_{\parallel}) = 45$ meV is used for all calculations³⁰.

In order to implement an approach based upon the Lorentzian line broadening function, an integration in k space is required along the k_{\parallel} axis,

$$\alpha_{MN}(\omega) = \frac{2\pi e^2}{ncm_0^2 \omega L} \int_{k_{\parallel}} dk_{\parallel} \left[f_N(k_{\parallel}) - f_M(k_{\parallel}) \right] \cdot |\hat{\epsilon} \cdot \bar{P}_{MN}|^2 \times \frac{(\Gamma_{NM}(k_{\parallel})/2)}{\left[\left(E_N(k_{\parallel}) - E_M(k_{\parallel}) - \hbar\omega \right)^2 + \left(\Gamma_{NM}(k_{\parallel})/2 \right)^2 \right]} \quad (82)$$

where f_N and f_M are the fermi occupation factors of equation 66 (not including the density of states), and the assumption of azimuthal isotropy is still in place. The approach of equation 82 will permit a more refined calculation of absorption profile shapes as well as absorption coefficient magnitudes.

The calculation of the absorption coefficients using the expression of equation 82 involves determining the regions in k_{\parallel} space over which integration should be carried out.

The integration is carried out over regions that have a populated ground state and unpopulated excited state, as determined by the values of $k_{||}$ that correspond to the fermi levels calculated via the DOS calculation. For each value of $k_{||}$ that must be integrated over it is necessary to determine the ΔE between the ground and excited states and the value of $\Gamma_{NM}(k_{||})$ in order to compute the value of the Lorentzian at that point and contributions from the proper combinations of the polarization vector and the momentum matrix elements must be integrated as well. The integration over $k_{||}$ must be carried out for all values of E_0 , the energy corresponding to $\hbar\omega$ of the incident radiation, and the results stored along with the value of E_0 . An example of an absorption coefficient plot generated via equation 82 is shown in figure II-17.

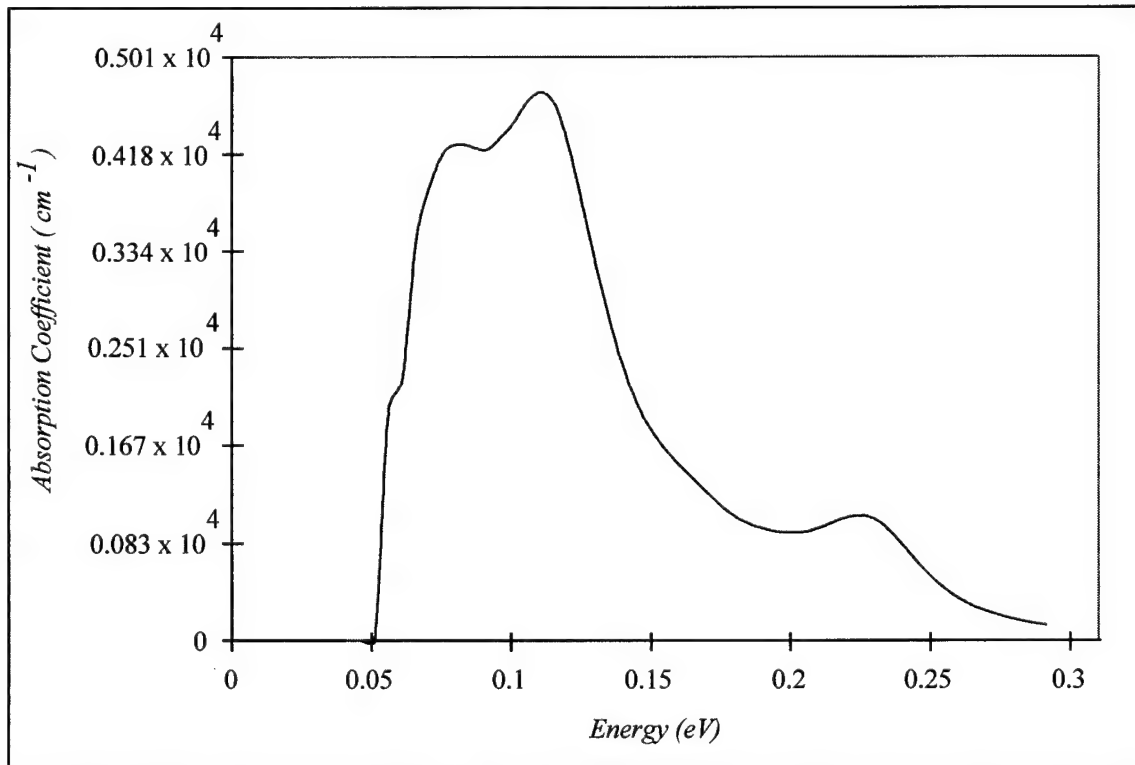


Figure II-17. Linear absorption coefficient vs energy produced by integrating a Lorentzian fit to all possible transitions. Absorption coefficient is for normally polarized light only. Exchange interaction is included.

Note that figure II-17 assumes light polarized in a single direction, which is not characteristic of any of the cases examined, but is meant merely to demonstrate some of the properties of the various methods of calculation. It should be noted that the magnitudes of the absorption coefficients, obtained via both the delta function and Lorentzian methods, match well with coefficients in the literature produced by similar methods applied to GaAs/Al_xGa_{1-x}As³ and Si/Si_{1-x}Ge_x³⁰ MQW structures.

Exchange Interaction.

The population of the lower lying subbands caused by the doping of the MQW sample produces an additional term referred to as the exchange interaction, which will change the energy level of the ground state subband. This term is due to the electromagnetic interaction between the carriers that populate the subbands, and will lower the energy of the ground state subbands from which inter-subband transitions are made, raising the energy difference between subbands. A detailed analysis of this interaction is carried out by Bandara and Coon²⁷, and the programs used to calculate this effect for this thesis are provided by M. Gregg²⁰. The addition of this effect, for the doping levels considered, brings the calculated peak positions closer to the experimental data.

The procedures described in chapter II must all be accomplished in order to arrive at an estimation of the linear absorption coefficients. This thesis project has resulted in the completion of absorption coefficient calculations for the Si [110] / Si_{1-x}Ge_x MQW system with x=.30 and well widths of 30 Å, and a variety of doping levels. These results

are easily applied to different well widths and Ge concentrations, as the mechanisms to calculate these cases are now in place. Chapter III describes presents the results of the calculations and experimental values for comparison and validation, along with some discussion of the approximations involved, and areas in which improvement of the model is desirable.

Chapter III. Results and Discussion

This chapter provides the results of calculations, using the various methods developed in chapter II, of the following quantities:

- (A) momentum matrix elements for transitions between the calculated well energy bands,
- (B) linear absorption coefficients calculated via equation 82 (the delta function formulation), and
- (C) linear absorption coefficients calculated via equation 87 (the Lorentzian distribution approximation).

Discussion of the relationship between calculated values and experimentally determined values or published theoretical results is included as well. Finally, recommendations for further investigation are included.

Section A. Calculation of Momentum Matrix Elements

Chapter II discussed the instability problem with respect to energy eigenvalues and bandweights. The problem of numerical instability also arises when the momentum matrix elements are calculated and the method of dealing with this instability is detailed below.

All of the instabilities encountered in analyzing the momentum matrix elements are found to be localized and the errors are of sufficiently small magnitude that the form of the momentum matrix elements can be easily discerned (see figure II-9). Indeed, many of the momentum matrix elements and bandweights show no discontinuities. In the cases that showed instabilities it is possible to simply correct the errant values by hand.

The correction of instabilities by hand is only possible where the form of the momentum matrix elements as a function of $k_{||}$ is obvious. Therefore this method is only used to correct the values along the $k_{||}[00-1]$ direction, as the values along other directions were not easily discernible in many cases. Visually correcting the errant values is the method used to obtain valid relations for the momentum matrix elements and only the smoothed values will be presented from this point forward.

Momentum matrix elements are calculated for the transitions shown in table III-1. The determination of the range of $k_{||}$ values over which inter-subband transitions may take place is based on the fermi level calculation outlined in chapter II. Fermi levels were calculated to be -0.108648 eV for the 10^{19} cm^{-3} doping level and -0.131457 eV for the $2 \cdot 10^{19} \text{ cm}^{-3}$ doping level.

TABLE III-1.
VALUES OF $k_{||}$ FOR ALLOWED BAND TRANSITIONS FOR
FERMI LEVELS CONSIDERED ($1 \cdot 10^{19} \text{ cm}^{-3}$, $2 \cdot 10^{19} \text{ cm}^{-3}$)

TRANSITION	$N_A = 1 \cdot 10^{19} \text{ cm}^{-3}$	$N_A = 2 \cdot 10^{19} \text{ cm}^{-3}$
HH1 \rightarrow LH1	(0.013 \rightarrow 0.016)	(0.0107 \rightarrow 0.0136)
HH1 \rightarrow HH2	(0.00833 \rightarrow 0.016)	(0.00592 \rightarrow 0.0136)
HH1 \rightarrow HH3	(0.0 \rightarrow 0.00944)	(0.0 \rightarrow 0.00944)
HH1 \rightarrow LH2	(0.0 \rightarrow 0.00694)	(0.0 \rightarrow 0.00694)
HH1 \rightarrow HH4	(0.0 \rightarrow 0.00611)	(0.0 \rightarrow 0.00611)
LH1 \rightarrow HH2	(0.00833 \rightarrow 0.013)	(0.00592 \rightarrow 0.0107)
LH1 \rightarrow HH3	(0.0 \rightarrow 0.00944)	(0.0 \rightarrow 0.00944)
LH1 \rightarrow LH2	(0.0 \rightarrow 0.00694)	(0.0 \rightarrow 0.00694)
LH1 \rightarrow HH4	(0.0 \rightarrow 0.00611)	(0.0 \rightarrow 0.00611)
HH2 \rightarrow HH3	(0.0 \rightarrow 0.00833)	(0.0 \rightarrow 0.00592)
HH2 \rightarrow LH2	(0.0 \rightarrow 0.00694)	(0.0 \rightarrow 0.00592)
HH2 \rightarrow HH4	(0.0 \rightarrow 0.00611)	(0.0 \rightarrow 0.00592)
* All values of $k_{ }$ are reported in units of \AA^{-1} .		

In order to save time, momentum matrix elements were calculated only in the $k_{||}$ regions in which transitions are allowed.

The momentum matrix elements for the various band transitions are shown in component form (P_x , P_y , and P_z) in the figures III-1 through III-9, for a Si[110]/Si₇₀Ge₃₀ well of 30 Å width. Note the magnitude of the P_x and P_y momentum matrix elements, which will determine the magnitude of the normal incidence absorption coefficients.

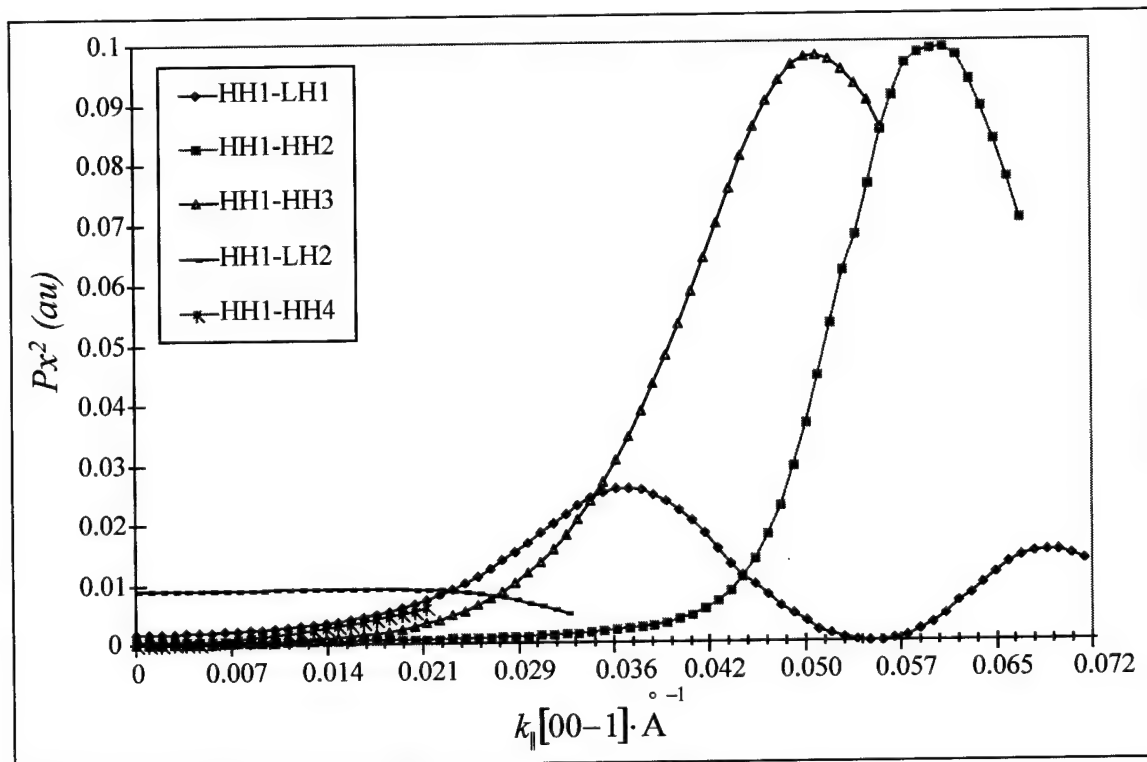


Figure III-1. P_x^2 vs $k_{||}$ for transitions from the HH1 band.

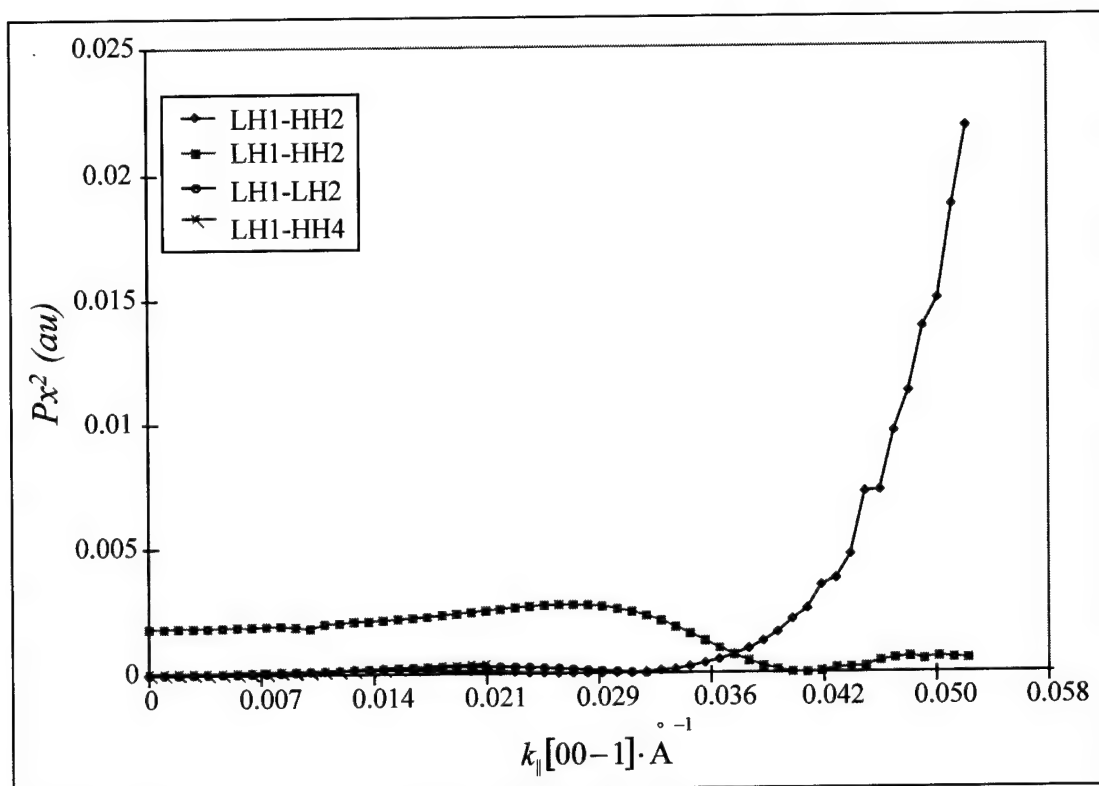


Figure III-2. P_x^2 vs k_{\parallel} for transitions from the LH1 band.

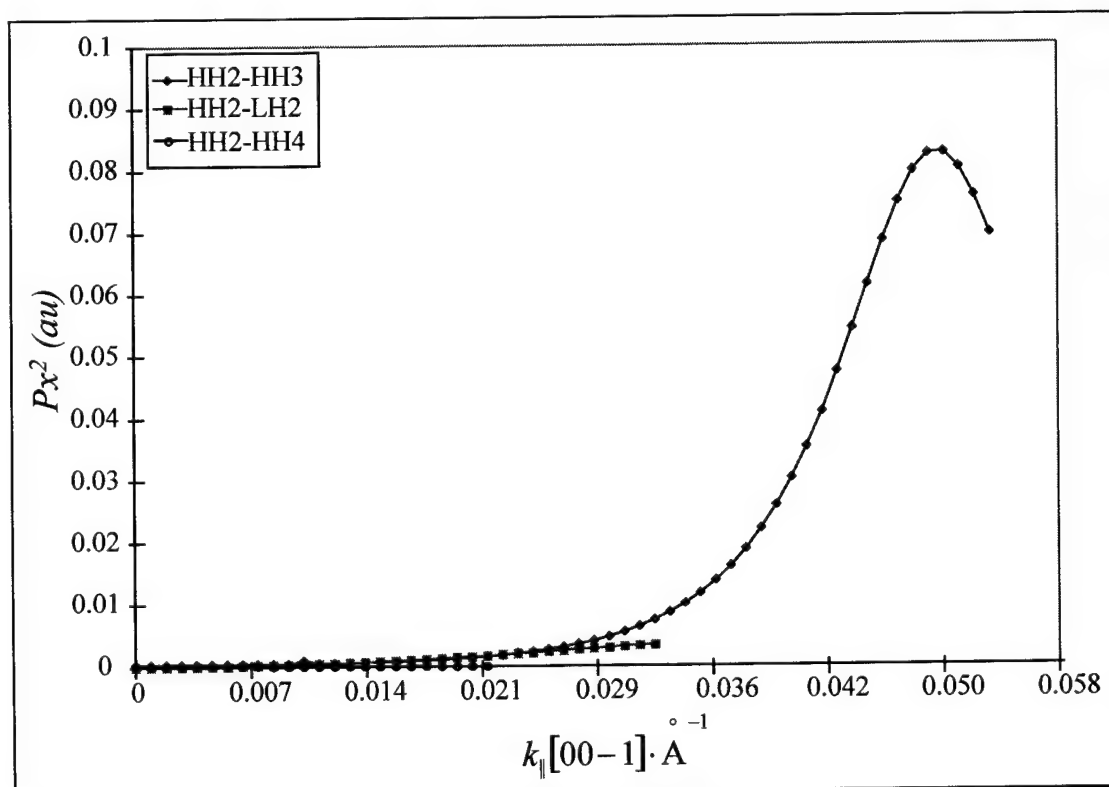


Figure III-3. P_x^2 vs k_{\parallel} for transitions from the HH2 band.

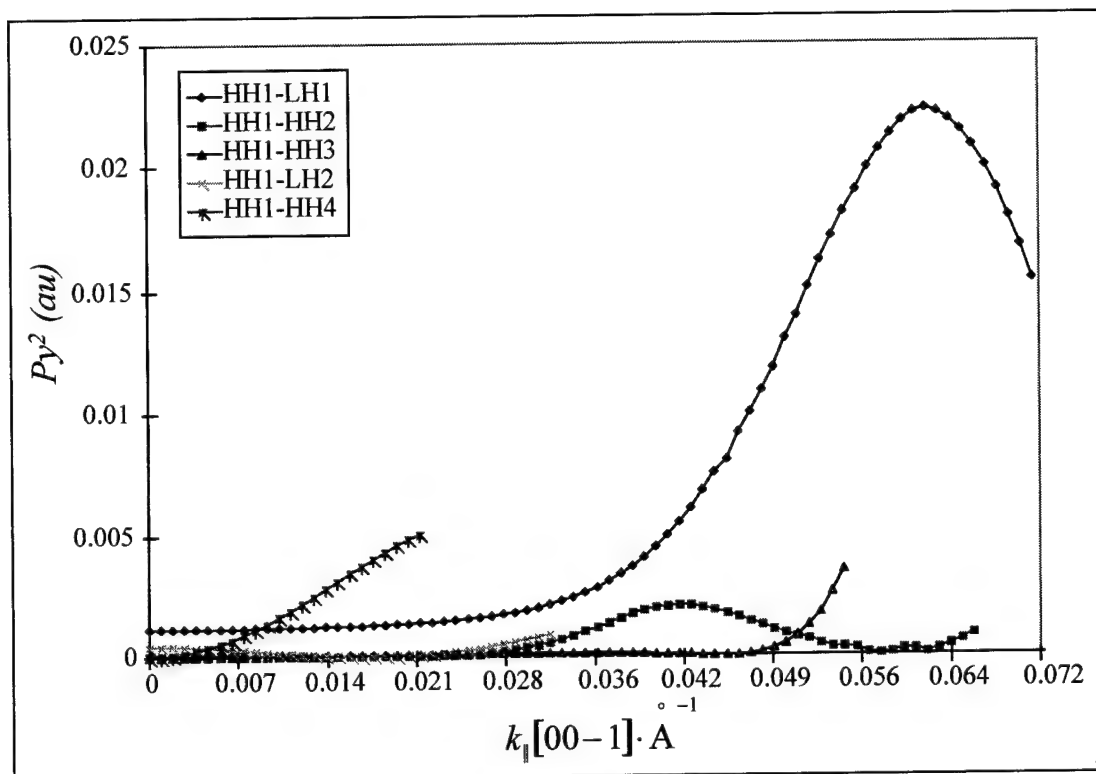


Figure III-4. P_y^2 vs k_{\parallel} for transitions from the HH1 band.

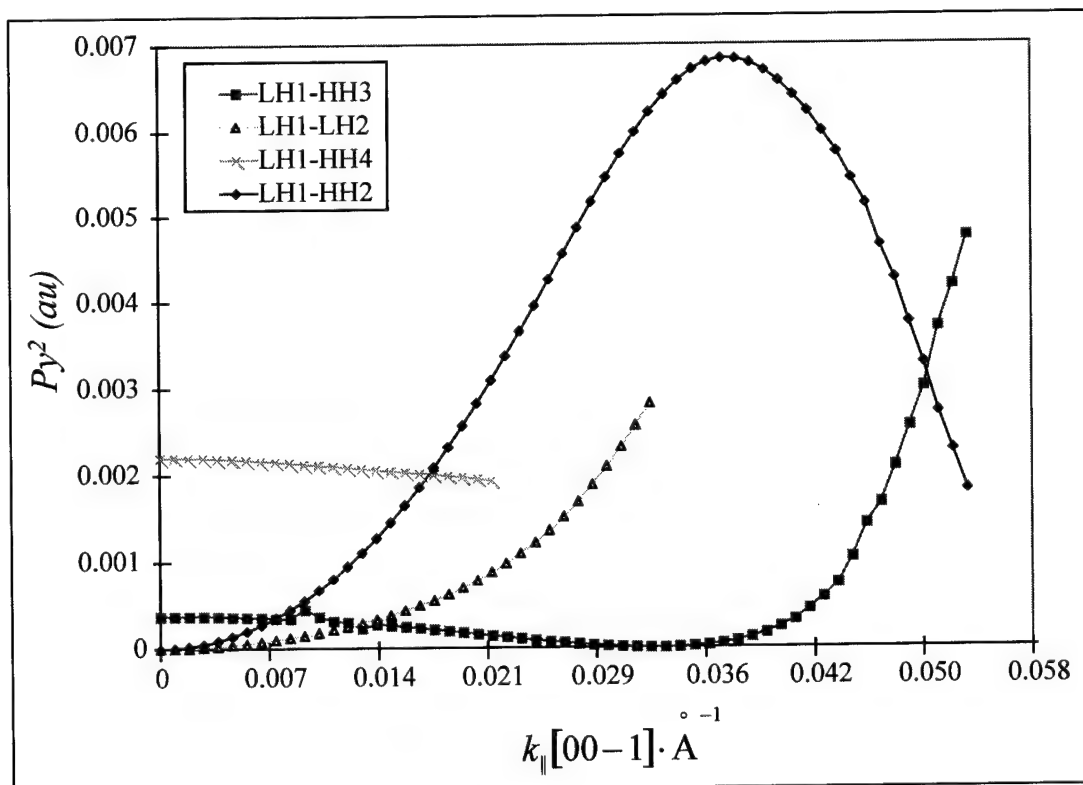


Figure III-5. P_y^2 vs k_{\parallel} for transitions from the LH1 band.

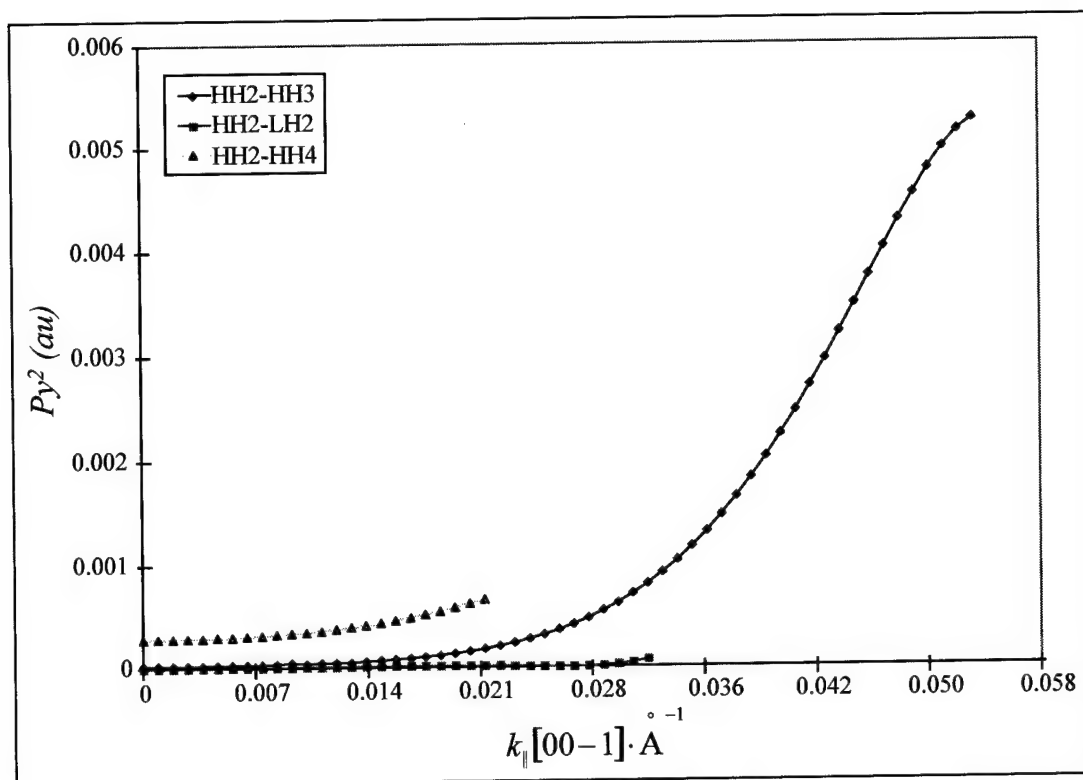


Figure III-6. P_y^2 vs k_{\parallel} for transitions from the HH2 band.

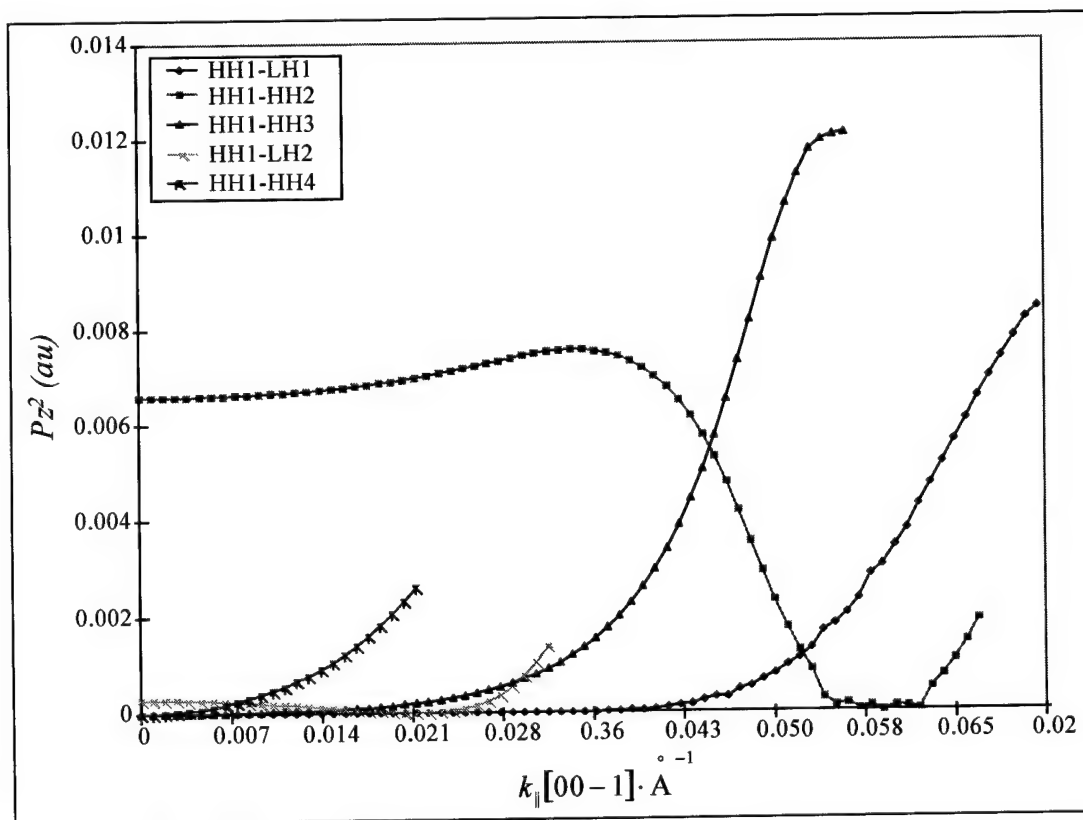


Figure III-7. P_z^2 vs k_{\parallel} for transitions from the HH1 band.

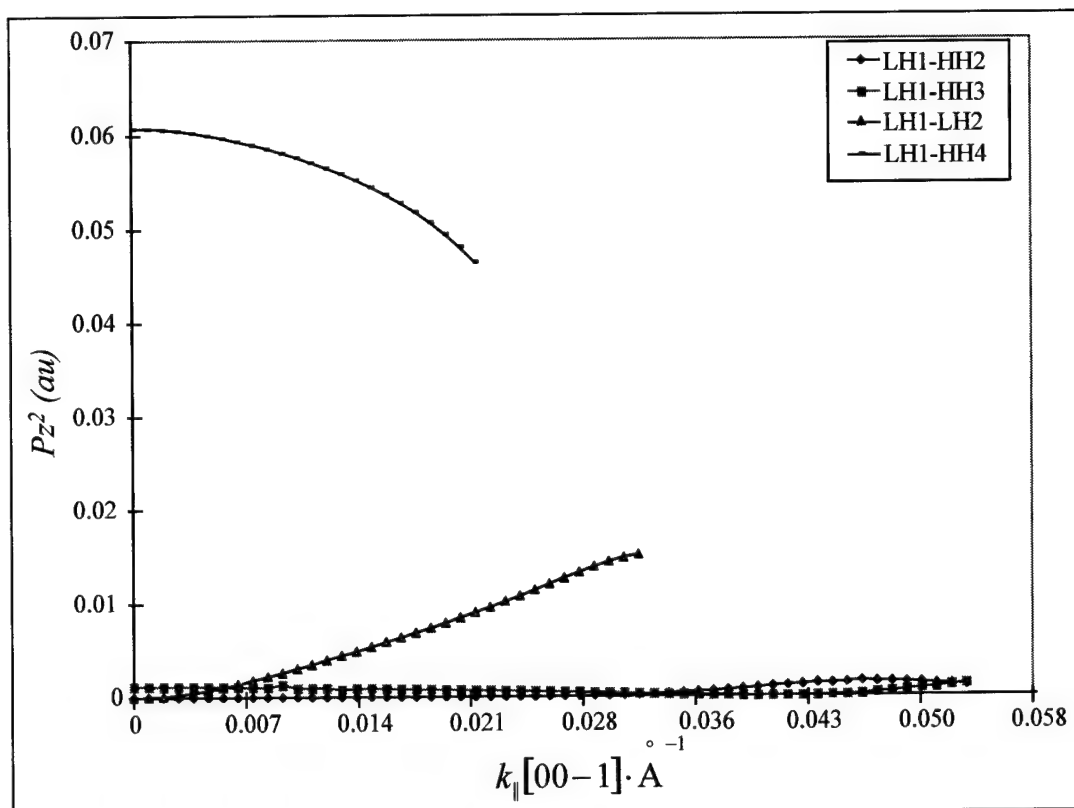


Figure III-8. P_z^2 vs k_{\parallel} for transitions from the LH1 band.

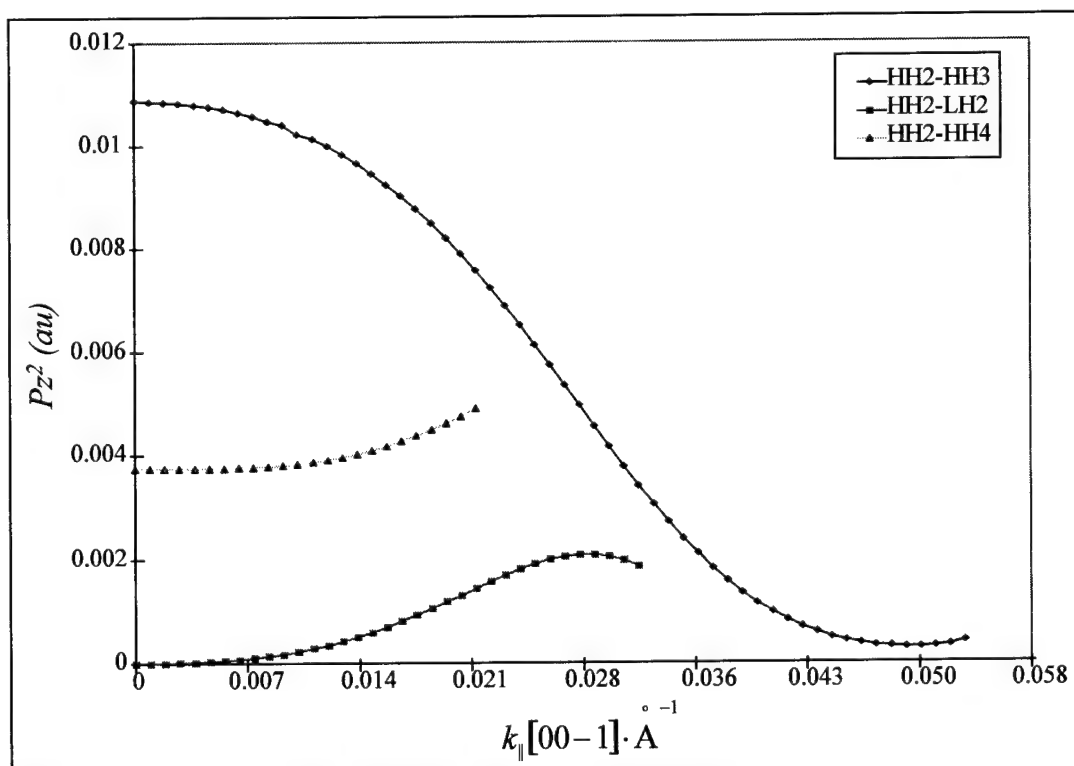


Figure III-9. P_z^2 vs k_{\parallel} for transitions from the HH2 band.

It is apparent from figures III-1 through III-9 that normal incidence absorption should be possible for the well geometry and substrate orientation examined. The magnitudes of the P_x and P_y elements are comparable to the magnitudes of the P_z elements, so it is expected that normal incidence absorption coefficients should be of the same order of magnitude as of those for parallel incidence.

Section B. Linear Absorption Coefficients Derived via the Delta Function

Approximation

The linear absorption coefficients obtained via equation 79 are presented in this section. When the form of $\nabla(E_N - E_M)$, found in the denominator of equation 79, is considered it is seen to pass through zero for many of the band pairs. Since $\nabla(E_N - E_M)$ appears in the denominator of equation 79, this behavior will lead to singularities in $\alpha(E)$ throughout the energy spectrum. This behavior is not unexpected and is present in the calculations performed by Szmulowicz³ for the GaAs/ $Al_xGa_{1-x}As$ system.

The principal problem with the singularities that occur in the absorption coefficients is that an estimation of the true magnitude of the absorption coefficient is impossible. The magnitudes of the various peaks are, in theory, infinite. In practice, the magnitudes of the peaks depend heavily upon how close the finite sized steps that the program takes in energy space come to the location of the singularity. The magnitude of the square of the momentum matrix element affects the height of the peak, but has

become a secondary factor. This behavior should be borne in mind while considering figures III-10 through III-20 which show the absorption peaks calculated using the delta function approach.

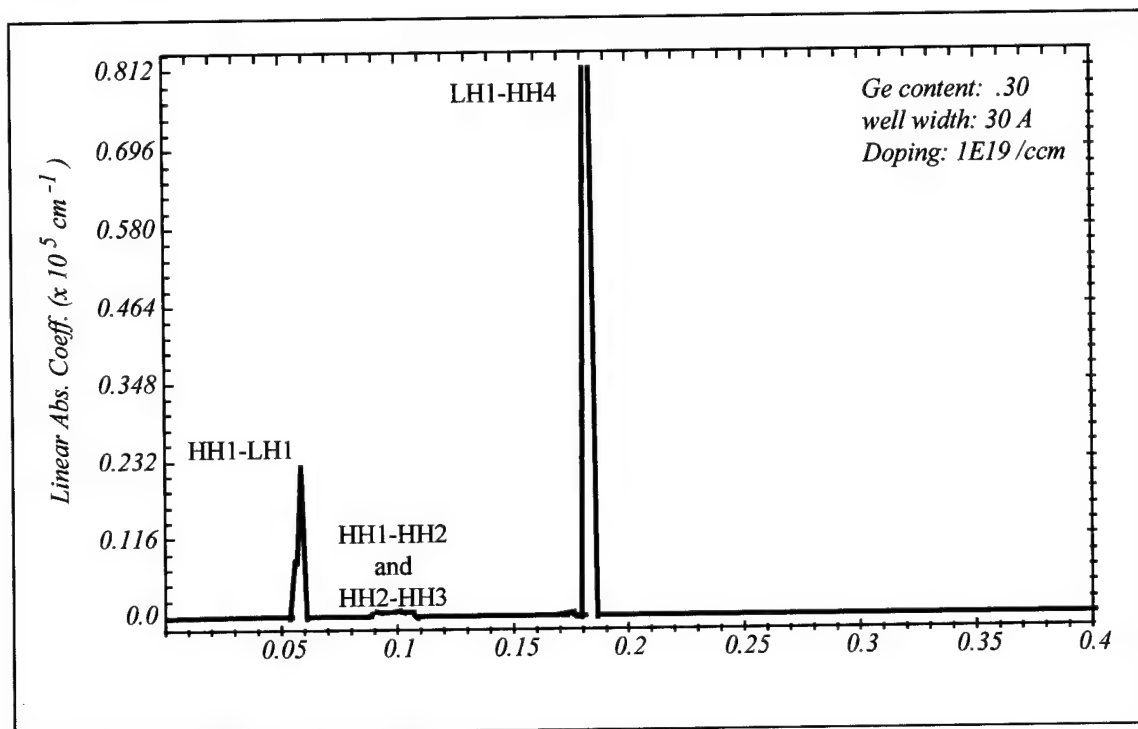


Figure III-10. Absorption coefficient peaks for \hat{z} polarization component, present in non-normally incident radiation. In practice, this spectrum will also be accompanied by \hat{x} or \hat{y} contributions.

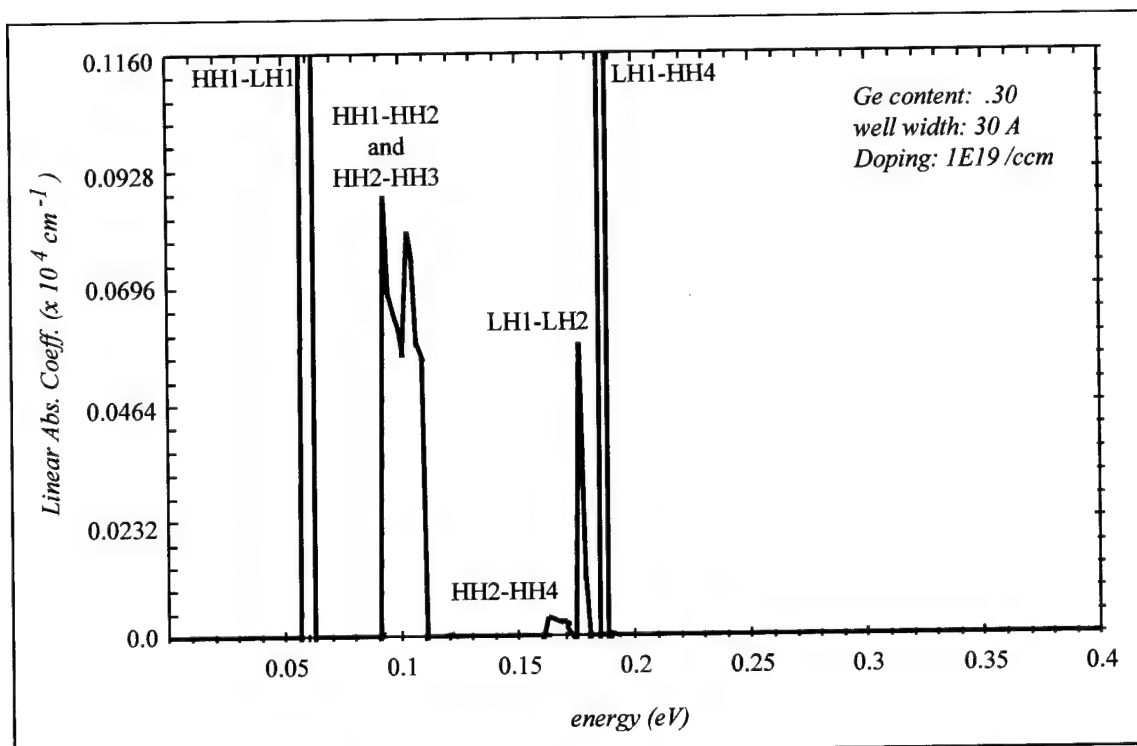


Figure III-11. Absorption coefficient peaks for the \hat{z} polarization component, present in non-normally incident radiation, scale expanded to show more details of the lower magnitude peaks.

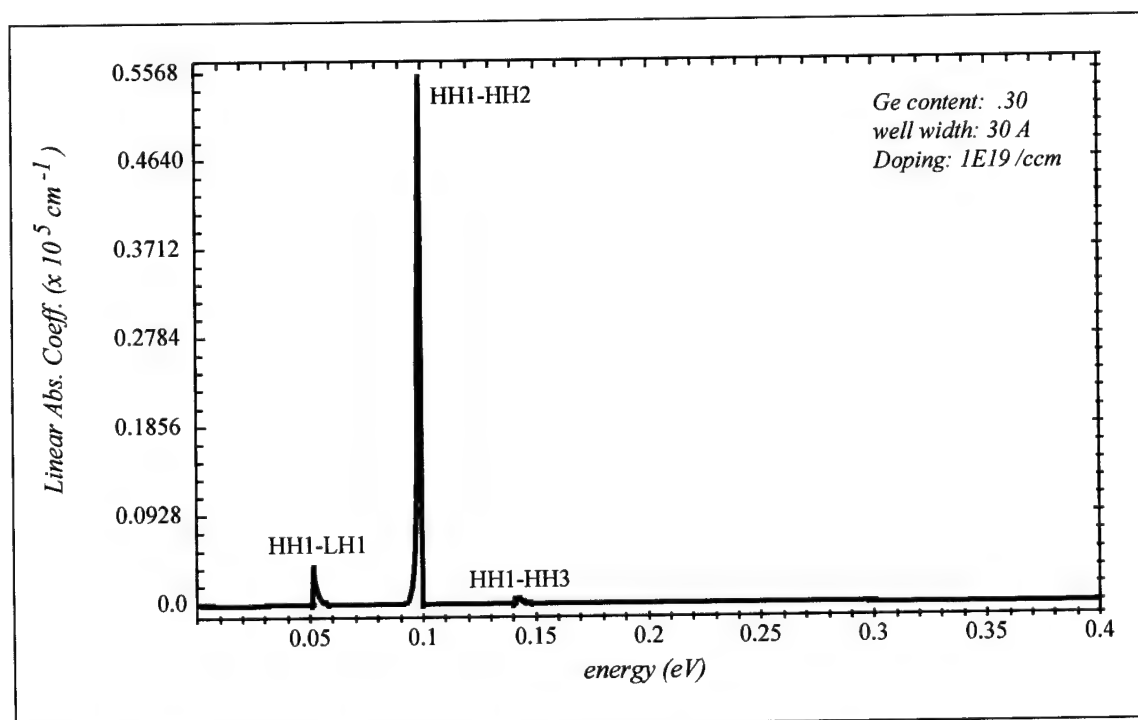


Figure III-12. Absorption coefficient peaks for the \hat{x} component of incident radiation.

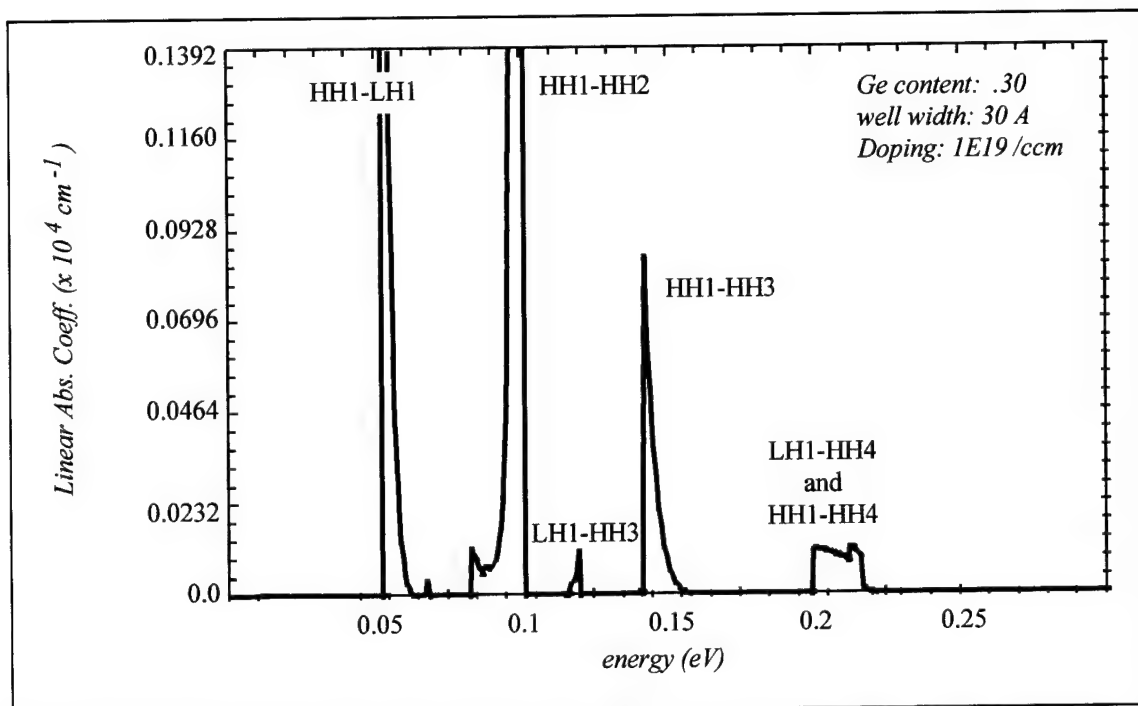


Figure III-13. Absorption coefficient peaks for the \hat{x} component of incident radiation, scale expanded to show details of lower magnitude peaks.

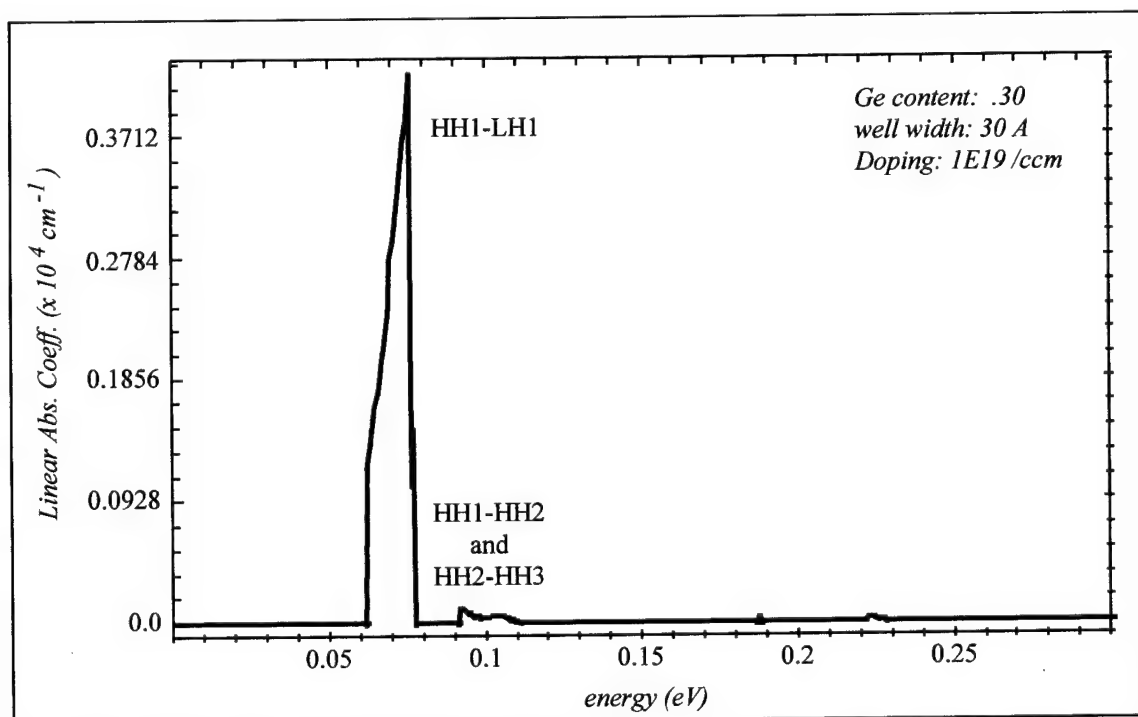


Figure III-14. Absorption coefficient peaks for the \hat{y} component of incident radiation.

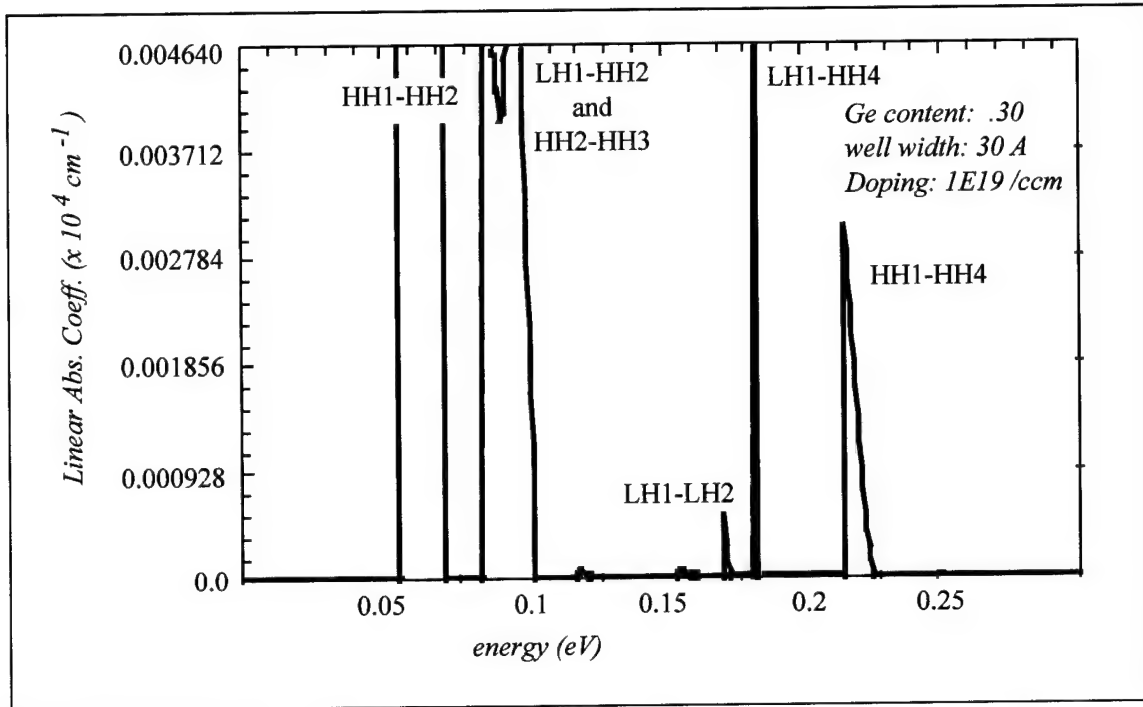


Figure III-15. Absorption coefficient peaks for the \hat{y} component of incident radiation, scale expanded to show detail of lower magnitude peaks.

Despite the difficulties in determining magnitudes of absorption coefficients based on this approach, the method does verify the locations of absorption peaks. These peaks do not match perfectly with experimental data, but lie within the observed absorption peak region. The magnitudes of the peaks, as well as locations of the peaks, are similar in magnitude to theoretical predictions presented by Szmulowicz for the GaAs/AlGaAs system.³ Figures III-23 through III-24 show the relative locations of the calculated peaks and experimental data for the Si[110] / Si_{0.70}Ge_{0.30}, 30 Å well for suitably summed P_x^2 , P_y^2 , and P_z^2 elements to produce normal and parallel incidence radiation.

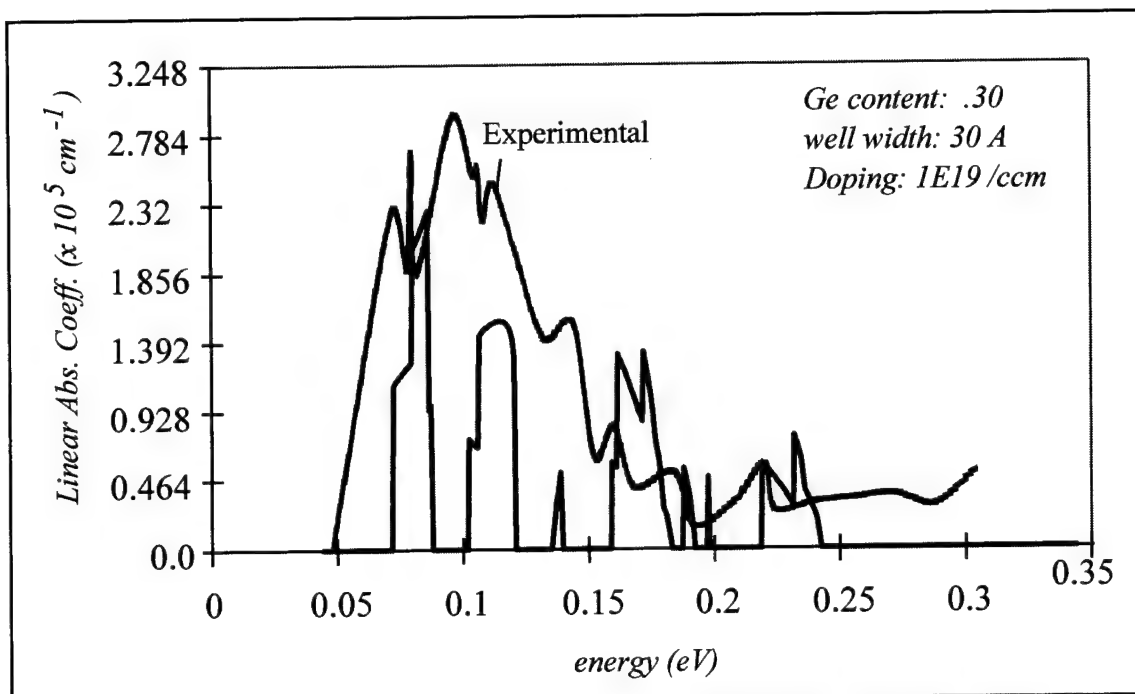


Figure III-16. Absorption coefficient ($\alpha(E)$) for normal incidence compared with experimental data.

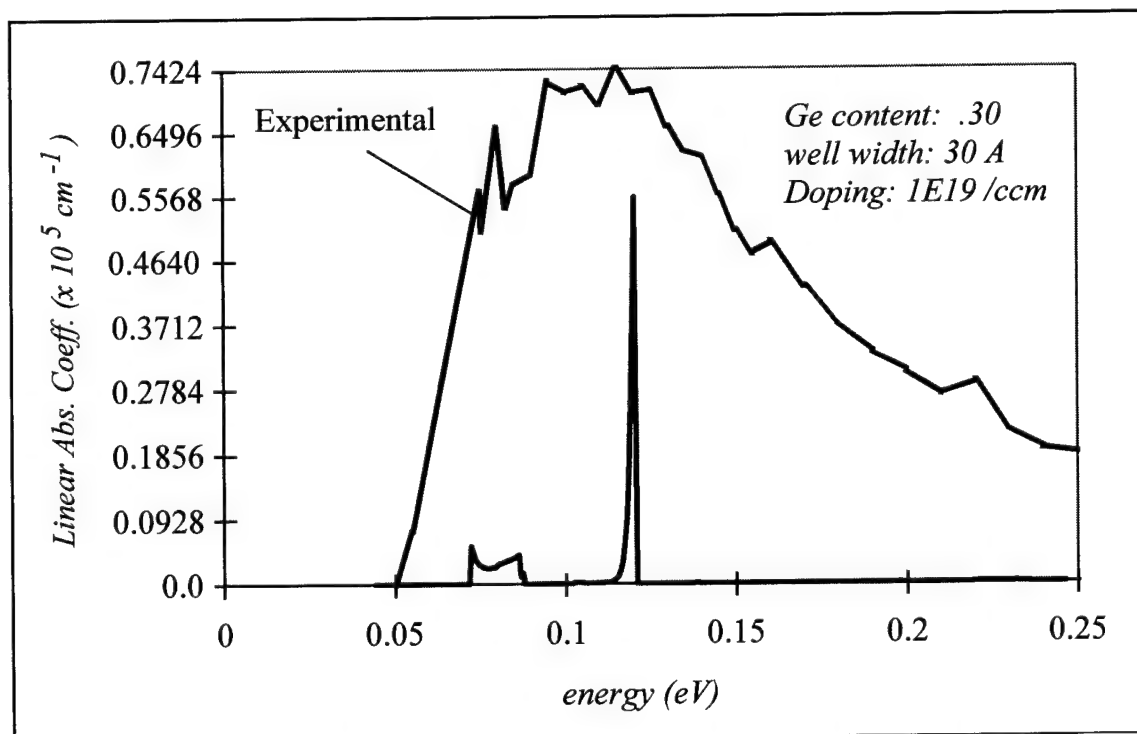


Figure III-17. Absorption coefficient ($\alpha(E)$) for normal incidence compared with experimental data.

Figures III-21 through III-22 show that the locations of the calculated peaks approximate the locations of the experimental peaks. Unfortunately, the lack of information about the magnitude of the absorption coefficients is an inherent feature of the model. In order to remedy this lack of information, the absorption coefficients are next computed using a Lorentzian line broadened technique.

Section C. Linear Absorption Coefficients Derived via the Lorentzian Approximation

The standard broadening mechanism for homogeneous line broadening in atomic transitions has the form of the Lorentzian discussed in chapter II. However, the form of the Lorentzian distribution used in this model differs from the commonly used Lorentzian in that the bands have some internal structure themselves instead of being a constant energy. This means that the neither the final nor initial energy values are constant, so the energy difference is constantly shifting over the range $k_{||}$ values that correspond to the allowed ΔE values. The form of a representative Lorentzian for this calculation is shown in figure III-24. The Lorentzian of figure III-24 corresponds to a fixed value of the incident photon energy ($\Delta E = .04$ eV) applied to the energy band difference HH1-LH1 shown in figure III-23.

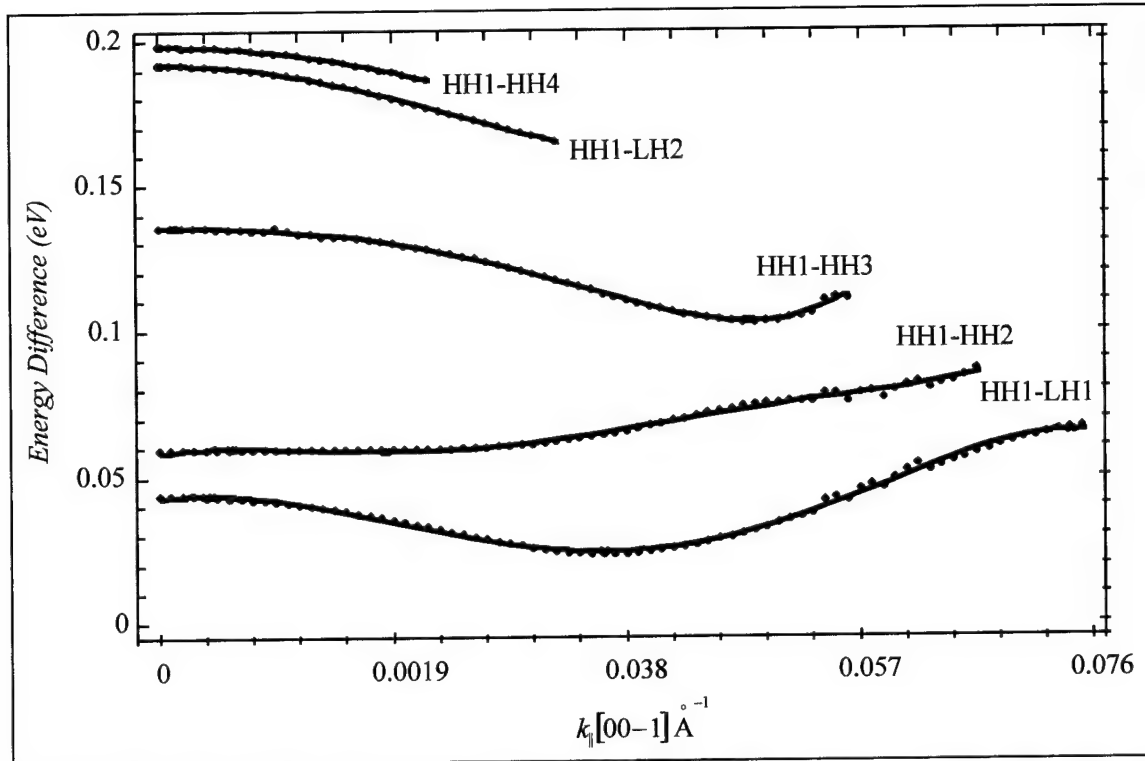


Figure III-18. Energy band differences between HH1 and higher lying bands. Note that locations where $\Delta E = \hbar\omega$ are not unique in many of the bands so that transitions may occur for several values of k_{\parallel} .

For a given value of incident photon energy ($\hbar\omega$), the Lorentzian has peaks wherever the inter-subband energy difference, ΔE , is equal to $\hbar\omega$. This behavior will weight more heavily the points in the band structure where a band transition is available that is “tuned” to the incident radiation. This weighting factor will be integrated along with the P_{NM}^2 terms in equation 82.

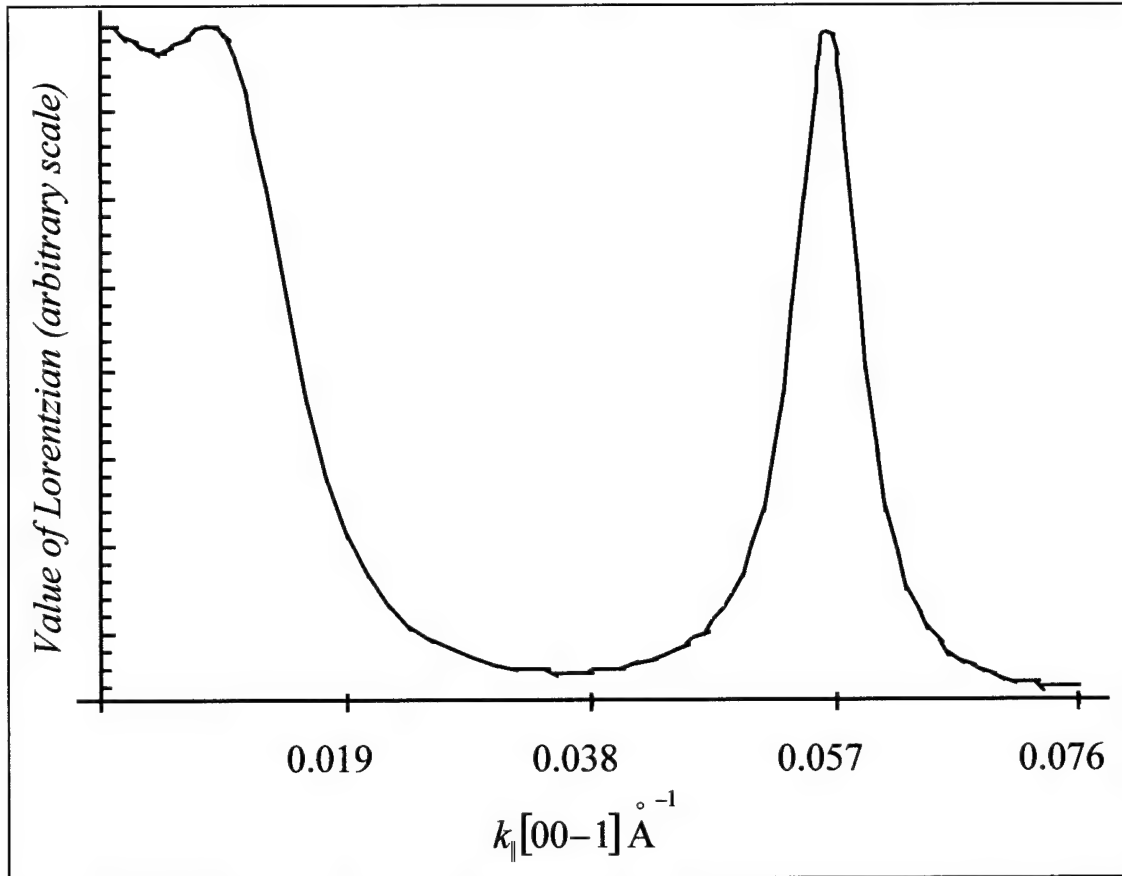


Figure III-19. Lorentzian function for a value of $\hbar\omega = 0.04$ eV for the HH1-LH1 band transition shown in figure III-24.

Figures III-26 Through III-28 show the absorption coefficients due to the effects of radiation polarized in the \hat{x} , \hat{y} , and \hat{z} directions respectively. These polarization states are not directly applicable to the experimental values, but when suitably added and averaged as shown in chapter II, will form the polarization vectors that correspond to normal and parallel incidence. It is for this reason that they are of interest.

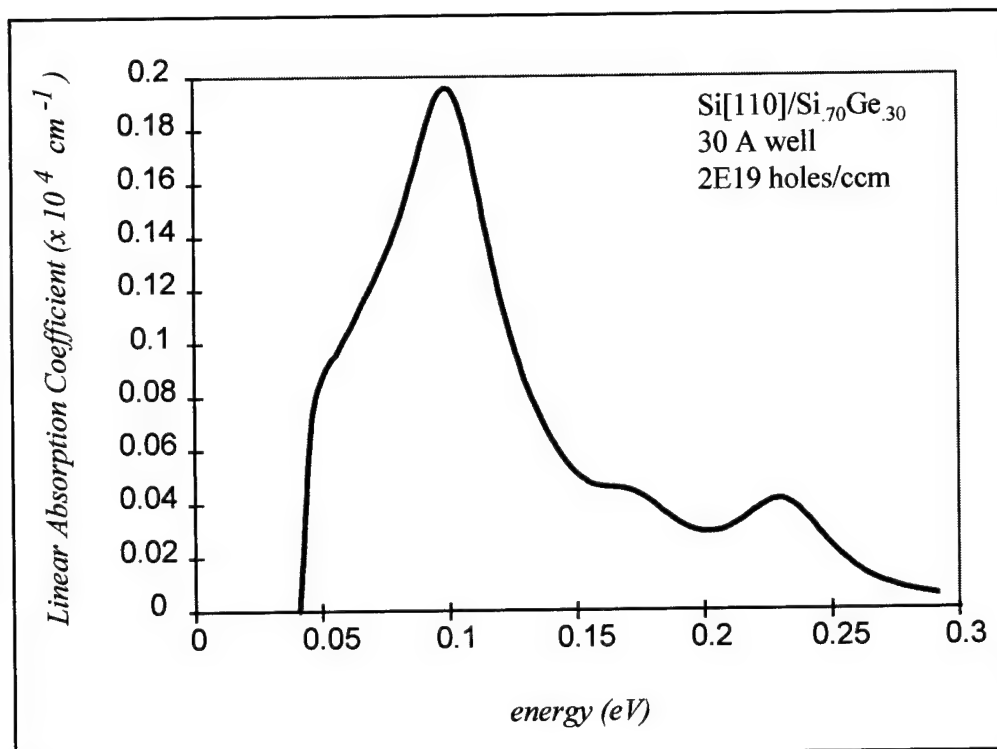


Figure III-20. Linear absorption coefficient for pure x polarization.

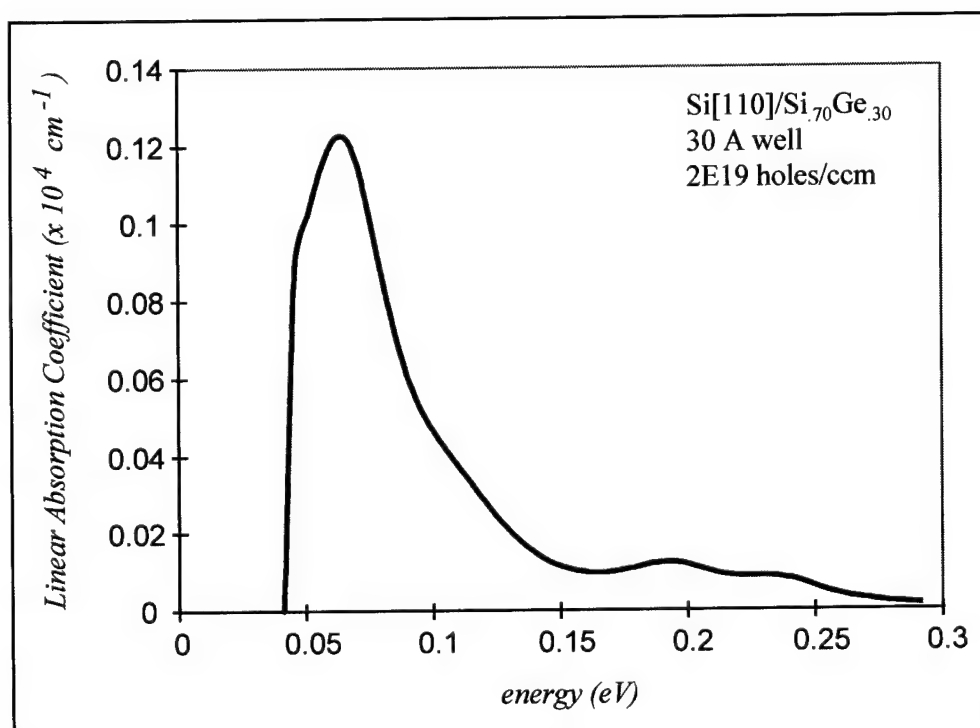


Figure III-21. Linear absorption coefficient for pure y polarization.

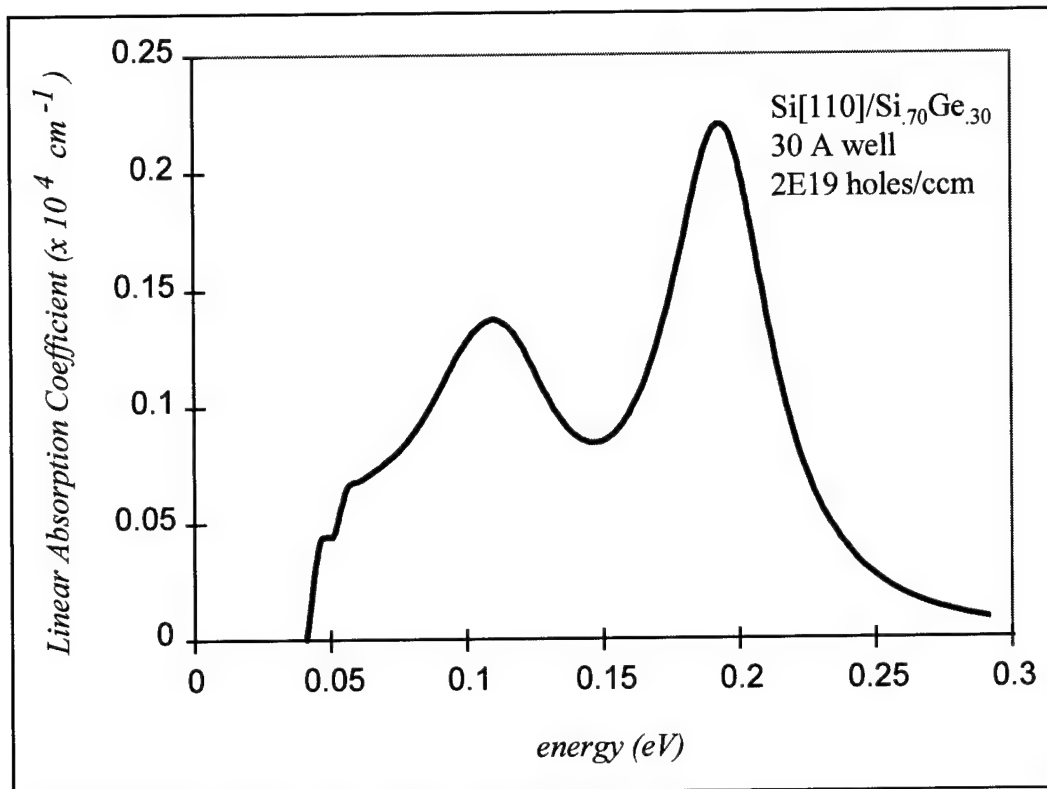


Figure III-22. Linear absorption coefficient for pure z polarization.

Figures III-23 through III-26 will show the calculated values of the absorption coefficients and the experimental values for suitably averaged normal and parallel incidence radiation. The magnitudes of the calculated values are shown by the vertical scale, but the values of the experimental values are not represented in the plot. The magnitudes of the experimental values are not shown since the absorptance depends upon both the value of the absorption coefficients and the total pathlength of the beam in the well regions, which is not known (multiple internal reflections occur within the sample). This uncertainty in the pathlength makes a determination of the absorptance from the calculated absorption coefficients difficult to carry out with any degree of accuracy.

Given these facts, the form of the absorption coefficients are compared to the observed values of the absorptance in order to judge the accuracy of the calculations.

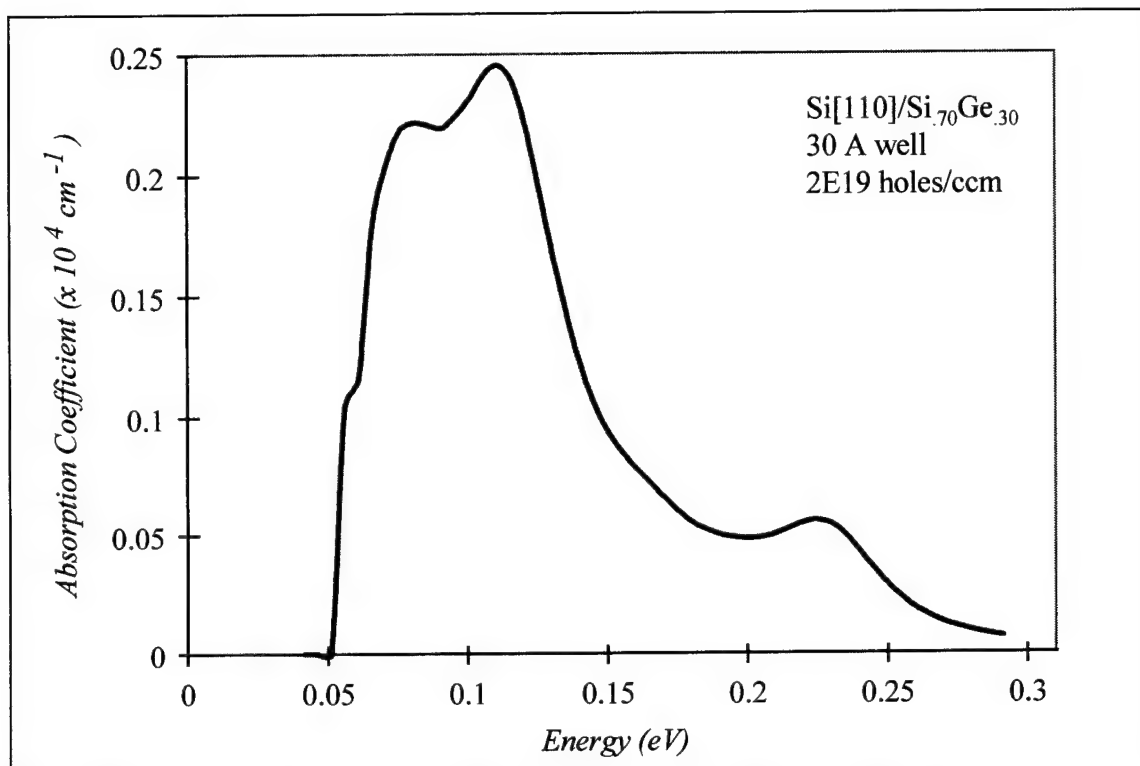


Figure III-23. Linear absorption coefficient for parallel incident radiation.

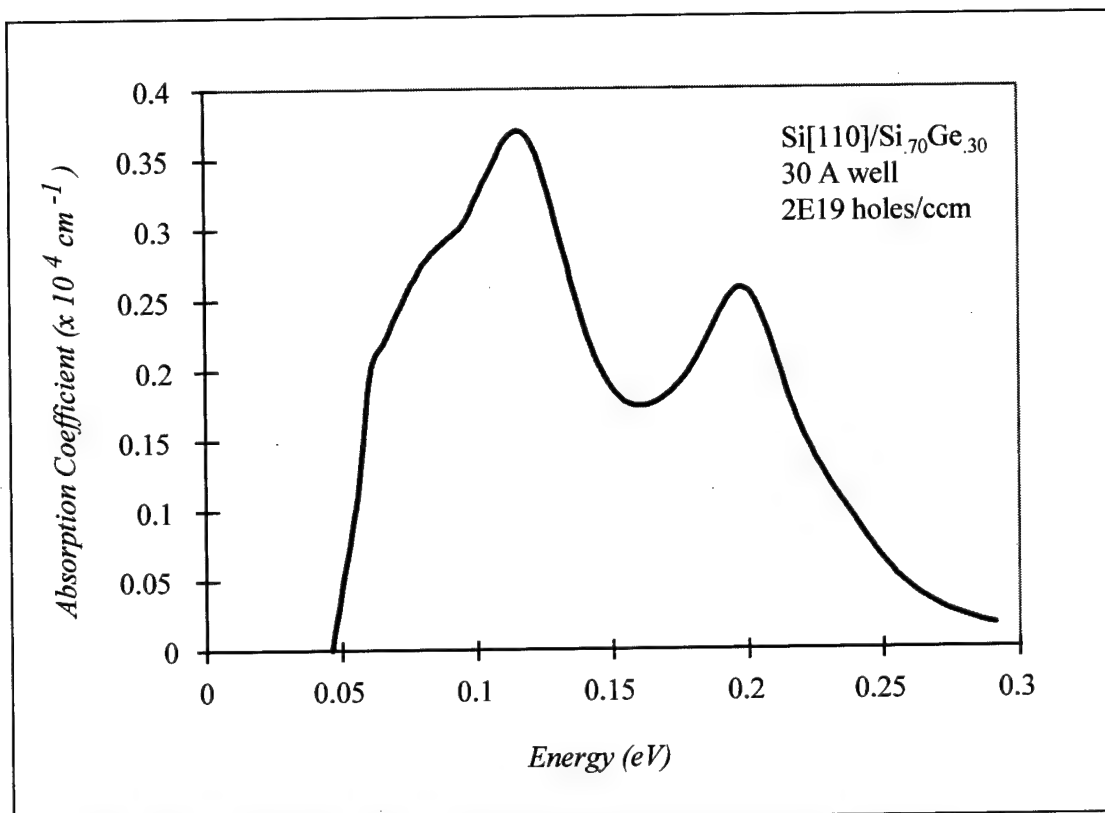


Figure III-24. Linear absorption coefficient for normally incident radiation.

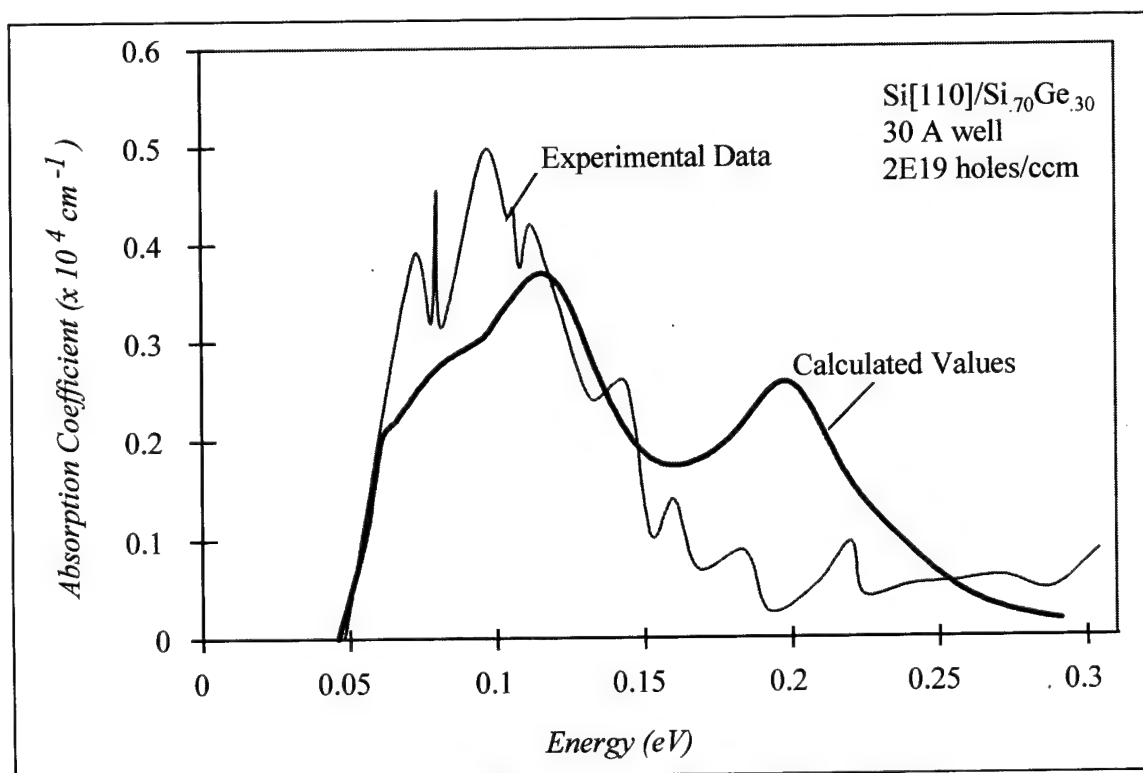


Figure III-25. Linear absorption coefficient for parallel incident radiation,

absorption coefficient scale applies only to the experimental absorbance values.

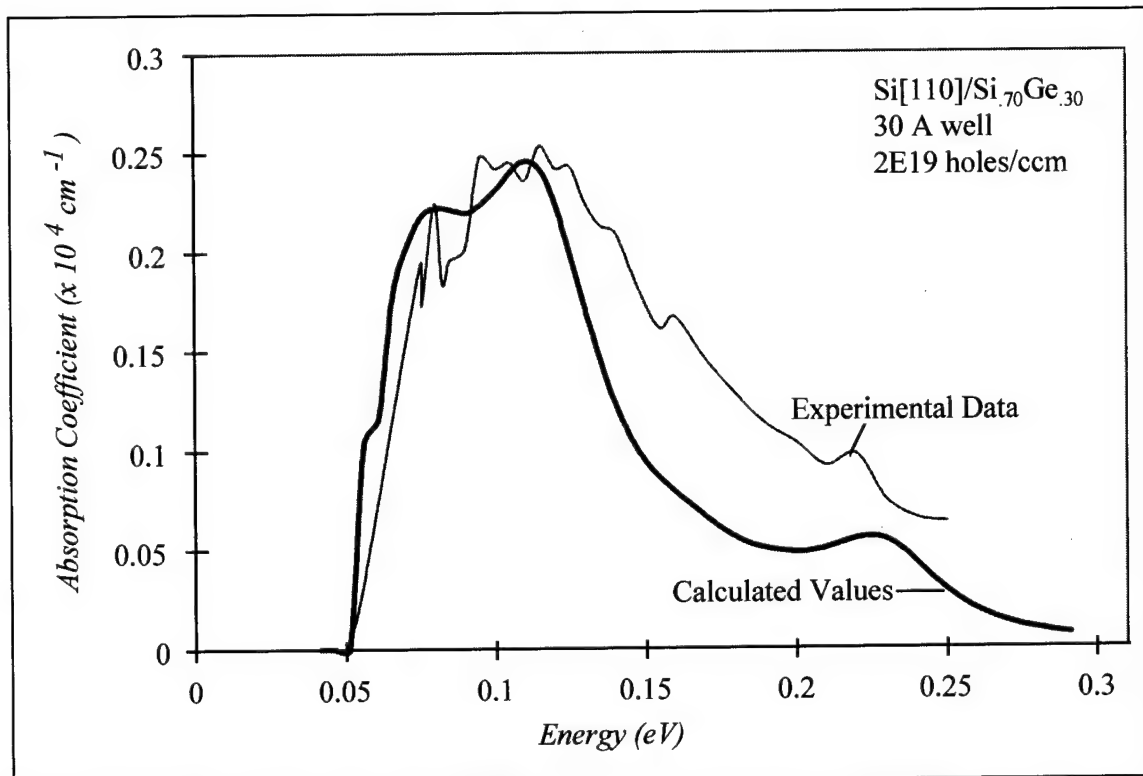


Figure III-26. Linear absorption coefficient for normally incident radiation, absorption coefficient scale applies only to the experimental absorbance values.

The locations of absorption peaks and the shapes of the absorption profiles have been approximated effectively by the model developed in chapter II. Unfortunately, the absolute magnitudes of the absorption coefficients are not verifiable with the available experimental data. The agreement with experimental values shown in figures 25 and 26 is perhaps better than expected, considering the number of approximations that are made to make the problem tractable. The calculated absorption coefficients and experimental data are shown as functions of wavelength in figures 27 and 28.

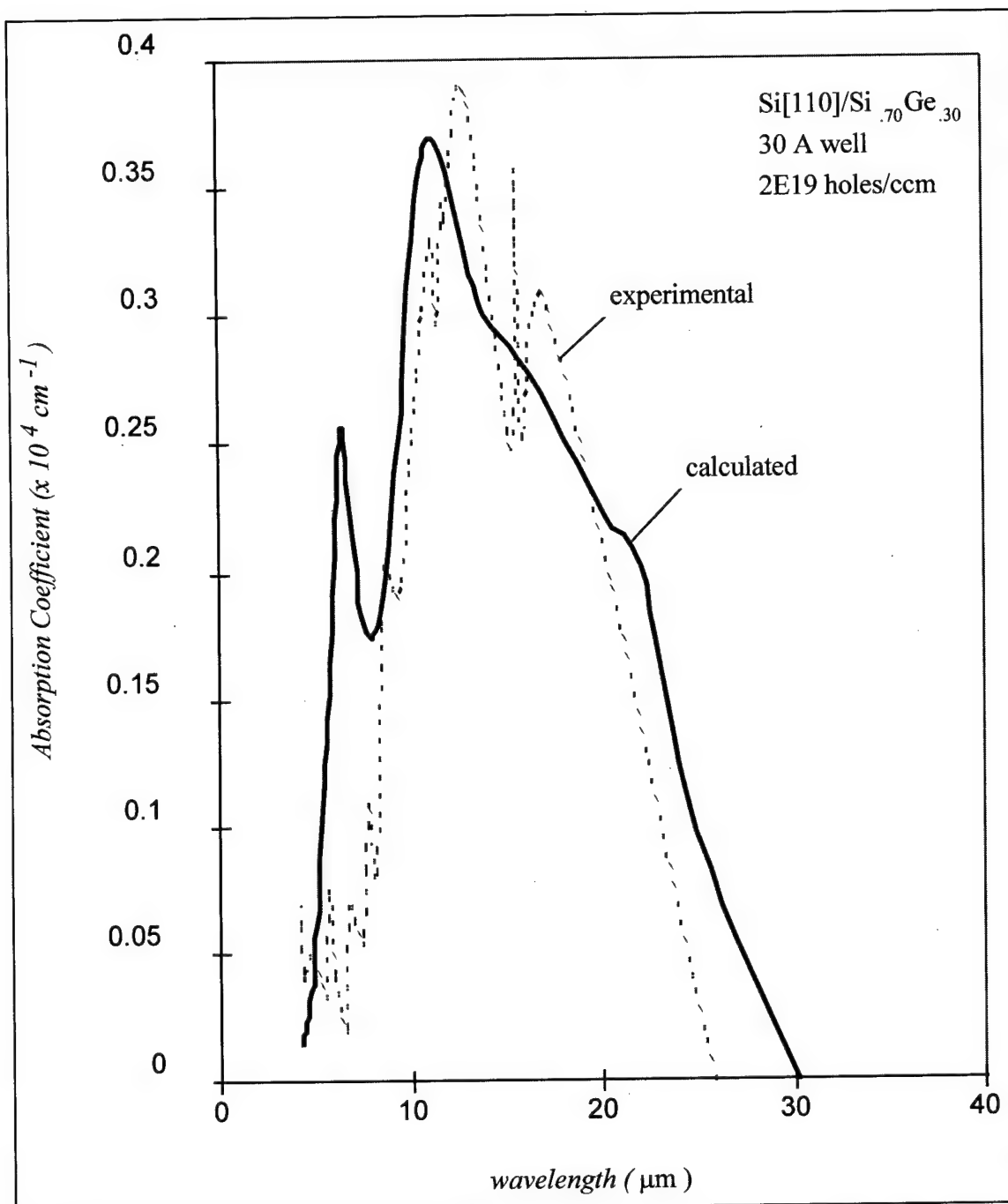


Figure III-27. Calculated absorption coefficients and experimental absorption data versus wavelength. Values are shown for parallel incident radiation.

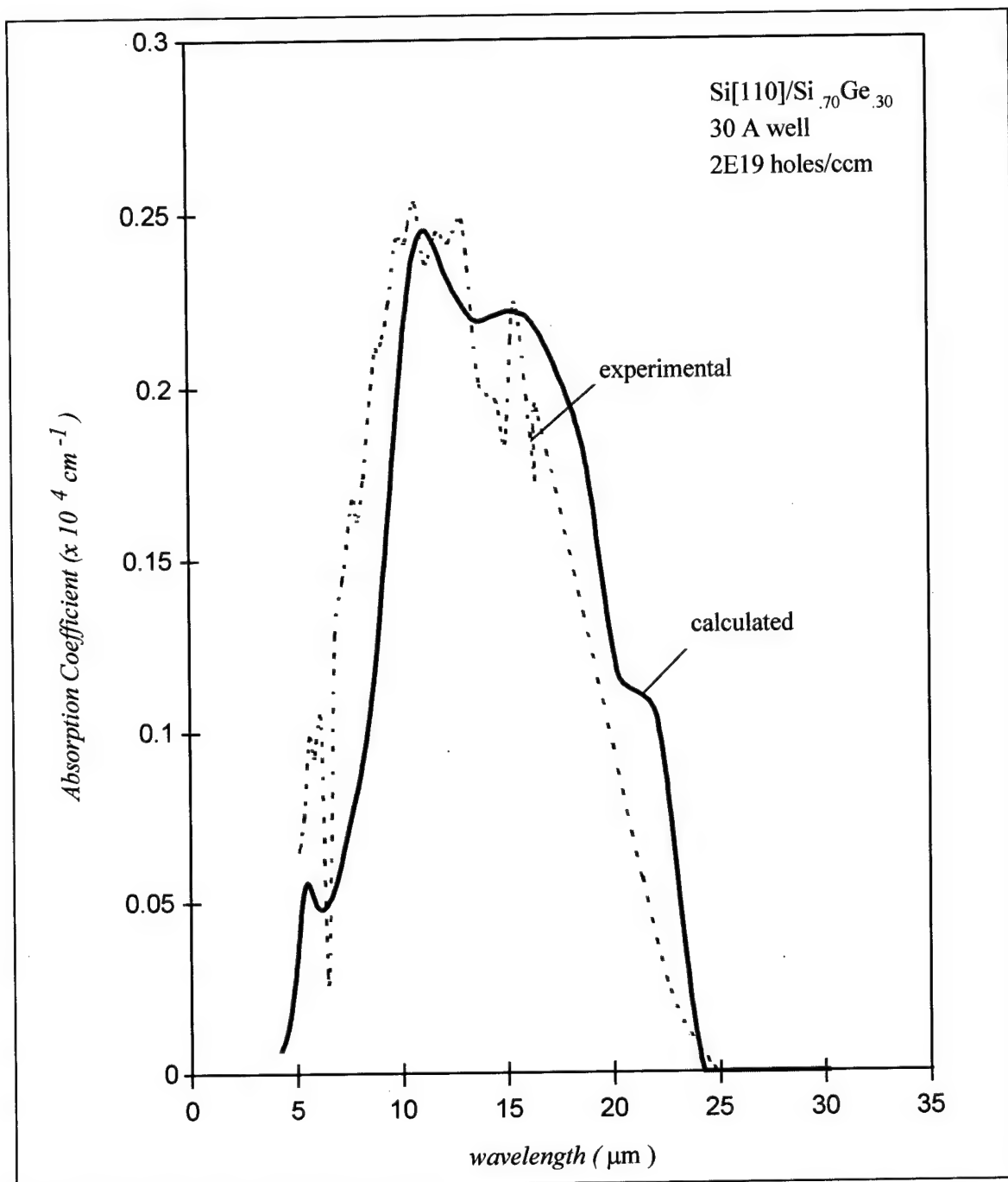


Figure III-28. Calculated absorption coefficients and experimental absorption data versus wavelength. Values are shown for normally incident radiation.

In a system as complex as the one under discussion several approximations must be used in order to render the problem theoretically comprehensible and computationally feasible and some aspects of the problem must be left unexplored. These approximations in many cases are areas in which further investigation may prove fruitful. Some of the major approximations and omissions in this project include the following:

- 1) conduction band coupling to the valence bands has been treated as unimportant,
- 2) the integration performed over the azimuthal rotation in $k_{||}$ space in order to calculate absorption coefficients was assumed to be over a constant function as a first approximation,
- 3) energy band structures are treated as being isotropic through azimuthal rotation in \mathbf{k} space and no sort of averaging is attempted,
- 4) the values of the line broadening parameter Γ_{NM} are chosen as a parameter in the computation, and a value of 45 meV was chosen based on figures found in the literature³⁰,
- 5) physical constants for $\text{Si}_{1-x}\text{Ge}_x$ alloy are approximated by linear interpolation from the equivalent Si and Ge constants, as no reliable data is available on this material,
- 6) phonon assisted, or indirect, transitions are not discussed as direct transitions provide the dominant mode for intersubband transitions², and
- 7) only the [110] substrate orientation is treated.

Section D. Recommendations and Summary

The results from this model match well with the observed absorption data for the system for the case studied. It will not be a difficult extension to the Si[001] substrate orientation and to other well geometries. These systems were not studied due to time constraints, but offer additional areas for investigation.

The model used for this project did not include the effects of conduction band coupling and did not calculate the conduction band wavefunctions. A treatment of these topics will allow computation of photoresponse behavior. The addition of conduction band coupling terms will improve the accuracy of the model with regard to the calculation of the absorption coefficients as well as photoresponse behavior.

The absorption coefficients were calculated by considering only the energy band structure in the $k_{||}$ [00-1] direction. It is known that the energy band structure is not symmetric with respect to azimuthal rotations in the (k_x, k_y) plane. This means that some form of integration over the azimuthal variations or an averaging process involving several $k_{||}$ directions should be applied to improve the accuracy of the model. This was not accomplished due to the numerical instabilities mentioned in chapter II and due to time constraints. This process is an area where further refinement will be beneficial.

A determination of the processes which produce the line broadening for the various subbands will provide an important clue to the nature of the line broadening

mechanism. If this were incorporated into the model the line broadening value would no longer be a parameter of the model.

An approximation is made by using the squared momentum matrix elements instead of using momentum matrix elements and then squaring. The cross terms produced by squaring terms that are complex in nature are therefore not included in the present calculations.

This project not only provides a theoretical characterization of the behavior of this system, but also can be extended to use in future problems and new systems. The programs developed to perform SiGe based calculations are easily modified to work with MQW structures developed with other materials by the modification of a few physical constants and parameters. The development of wavefunctions, absorption spectra, and other quantities of interest can be used as a basis for further theoretical studies on this system.

The linear absorption coefficient calculations performed in this thesis were shown to match in form with the experimental data available, to the limits of the model. The magnitude of the absorption coefficients were shown to be consistent with the published values for similar systems and well geometries.

Appendix A: Derivation of Finite-Depth Quantum Well Energy Levels

The problem of finding bound state energy levels in a potential well of finite depth is solved graphically in many elementary quantum mechanics texts. The solution of this problem is of utility, as it serves to illustrate the means of determining energy levels in the quantum well structure given the wave functions determined via the **k•p** method.

The quantum well is formed from a region of reduced potential embedded in a region of constant, higher potential. For the purposes of this derivation we will assume a sharp discontinuity in the potential at the well edges. The well structure and coordinates adopted are shown graphically in figure A.1.

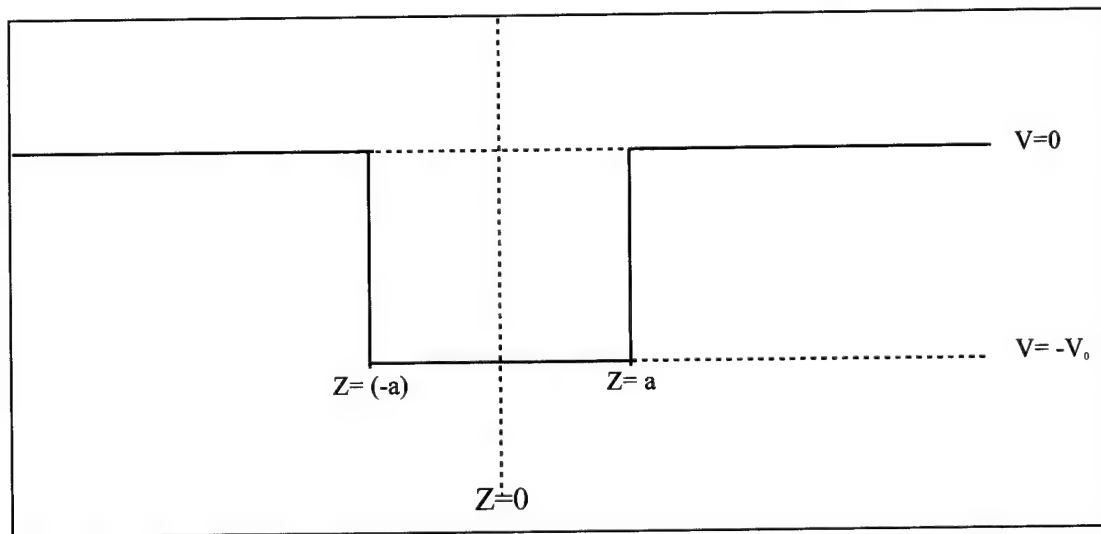


Figure A.1. Potential well coordinate system and geometry.

The wave function of a particle in this potential structure must obey Schrodinger's equation (in one dimension), given in equation (A.1).

$$-\frac{\hbar^2}{2m} \frac{\partial^2 \Psi(Z)}{\partial^2 Z} + V(Z) \cdot \Psi(Z) = E \cdot \Psi(Z) \quad (\text{A.1})$$

The form of the wave function will be defined in each of the three regions $\{Z < (-a), (-a) < Z < a, Z > a\}$ as a combination of plane waves travelling in the positive and negative Z directions, with coefficients initially assumed to be independent, as shown in equation (A.2). The use of these simplified wave functions in solving the problem is the major difference between the illustrative case developed in this appendix and the calculations performed in the formulation of the MQW problem.

$$\begin{aligned}\Psi_1 &= A \cdot e^{ik_1 Z} + B \cdot e^{-ik_1 Z} \\ \Psi_2 &= C \cdot e^{ik_2 Z} + D \cdot e^{-ik_2 Z} \\ \Psi_3 &= E \cdot e^{ik_1 Z} + F \cdot e^{-ik_1 Z}\end{aligned}\tag{A.2}$$

$$k_1 = \frac{\sqrt{2m(E - V_0)}}{\hbar} \quad k_2 = \frac{\sqrt{2mE}}{\hbar}$$

These wave functions are subject to 6 boundary conditions: Ψ_1 must be finite as $Z \rightarrow (-\infty)$, Ψ_3 must be finite as $Z \rightarrow (+\infty)$, the wavefunctions must be equal at the “walls” of the well, and the derivatives of the wave functions must be equal at the well edges. These conditions force B and E to zero to produce bounded wave functions at positive and negative infinity. These conditions produce a finite valued, continuous, smooth wave function over all ranges of Z .

These boundary conditions result in four equations, which are shown below in equations A.3 through A.6:

$$\Psi_1(-a) = \Psi_2(-a) \quad Ae^{-ik_1 a} = Ce^{-ik_2 a} + De^{ik_2 a} \tag{A-3}$$

$$\Psi_3(a) = \Psi_2(a) \quad Fe^{-ik_1 a} = Ce^{ik_2 a} + De^{-ik_2 a} \tag{A-4}$$

$$\frac{\partial \Psi_1(-a)}{\partial Z} = \frac{\partial \Psi_2(-a)}{\partial Z} \quad ik_1 Ae^{-ik_1 a} = ik_2 \cdot (Ce^{-ik_2 a} - De^{ik_2 a}) \tag{A-5}$$

$$\frac{\partial \Psi_2(a)}{\partial Z} = \frac{\partial \Psi_3(a)}{\partial Z} \quad -ik_1 F e^{-ik_1 a} = ik_2 \cdot (C e^{ik_2 a} - D e^{-ik_2 a}) \quad (A-6)$$

and these four equations can be recast in matrix form as in eqn A.7:

$$\begin{pmatrix} e^{-ik_1 a} & -e^{-ik_2 a} & -e^{ik_2 a} & 0 \\ k_1 e^{-ik_1 a} & -k_2 e^{-ik_2 a} & k_2 e^{ik_2 a} & 0 \\ 0 & -e^{ik_2 a} & -e^{-ik_2 a} & e^{-ik_1 a} \\ 0 & -k_2 e^{ik_2 a} & k_2 e^{-ik_2 a} & -k_1 e^{-ik_1 a} \end{pmatrix} \cdot \begin{pmatrix} A \\ C \\ D \\ F \end{pmatrix} = \bar{0} \quad (A.7)$$

$$\text{or} \quad \mathbf{M} \cdot \begin{pmatrix} A \\ C \\ D \\ F \end{pmatrix} = \bar{0}$$

There exists a non-trivial solution to this set of equations only if the determinant of \mathbf{M} is 0. This matrix is comprised only of known quantities and functions of E , the energy of the particle (via k_1 and k_2) and thus, the values of E for which the determinant goes to zero are the only values of E which satisfy Schroedinger's equation. This is a quick method to find the energy eigenstates of the system which will be used to construct the eigenfunctions.

The determinant of \mathbf{M} is a complicated function of E and the zeros are found via the use of a numerical root solving routine (available in Mathematica). This is the standard method (graphical solution) found in most elementary quantum mechanics texts.

^{1,2} These zeros of the determinant correspond to values of the energy that satisfy Schrodinger's equation for the system. In the 1-D, symmetric, square-well some assumptions and simplifications may be made to make the problem more easily visualizable and to make finding the roots of the determinant simpler, but the method

outlined above is the most general method and corresponds most closely with the method used in matching boundary conditions using the envelope function approximation (EFA) later in the problem. In the simple symmetric, 1-D well the wave functions are easily shown to be either symmetric or anti-symmetric about well center, and thus the constants are related as shown in equations (A.8-9) and (A.10-11).

Symmetric Case

$$A = F \quad (A.8)$$

$$C = D \quad \{\Psi_2 = C \cos (k_2 Z)\} \quad (A.9)$$

Anti-symmetric Case

$$A = -F \quad (A.10)$$

$$C = -D \quad \{\Psi_2 = C \sin (k_2 Z)\} \quad (A.11)$$

The plots of these functions are shown along with the plots of the unsimplified determinants to emphasize that the same answer is obtained in the general case as in these cases. The determinant function for a quantum well of depth of 5 au and width of 3 au is shown in fig. A.2, and the same determinant is shown greatly magnified (multiplied by 10^{14}) along with the cos and sin terms from the simplified case in fig. A.3. Fig. A.3 shows that the intercepts are the same for both methods.

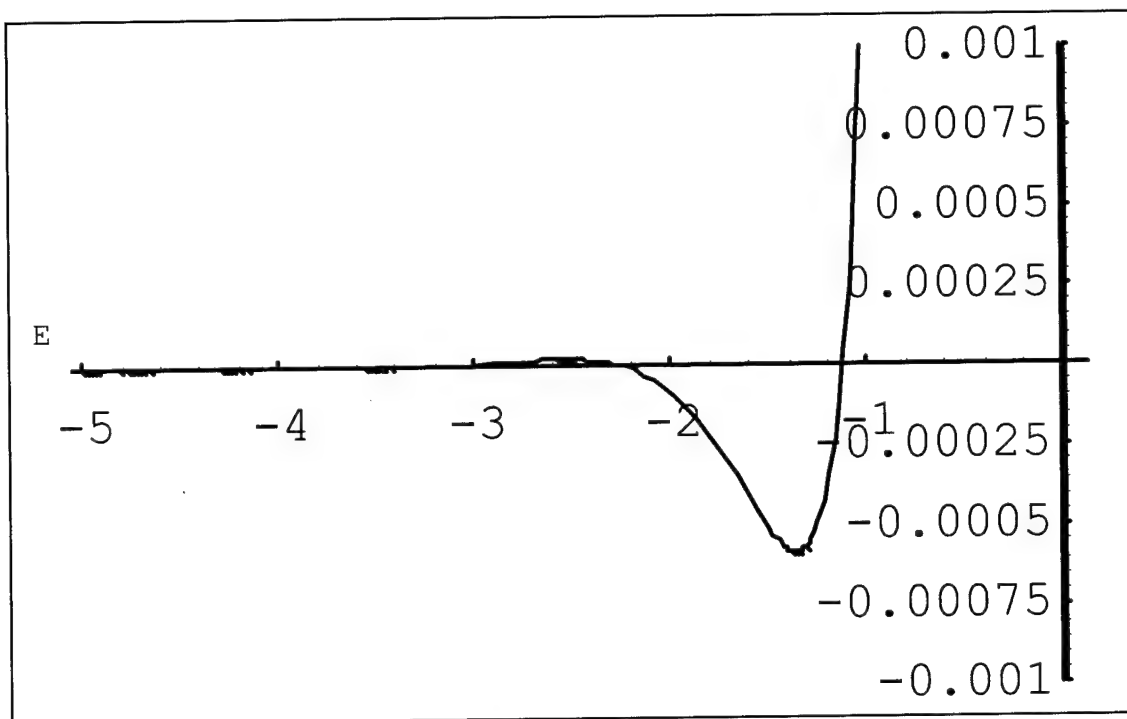


Fig A.2. Plot of the determinant of \mathbf{M} for a square well of depth 5 au and width of 3 au. The function is oscillating in the region between $E=-5$ and $E=-3$, and rapidly grows in magnitude.

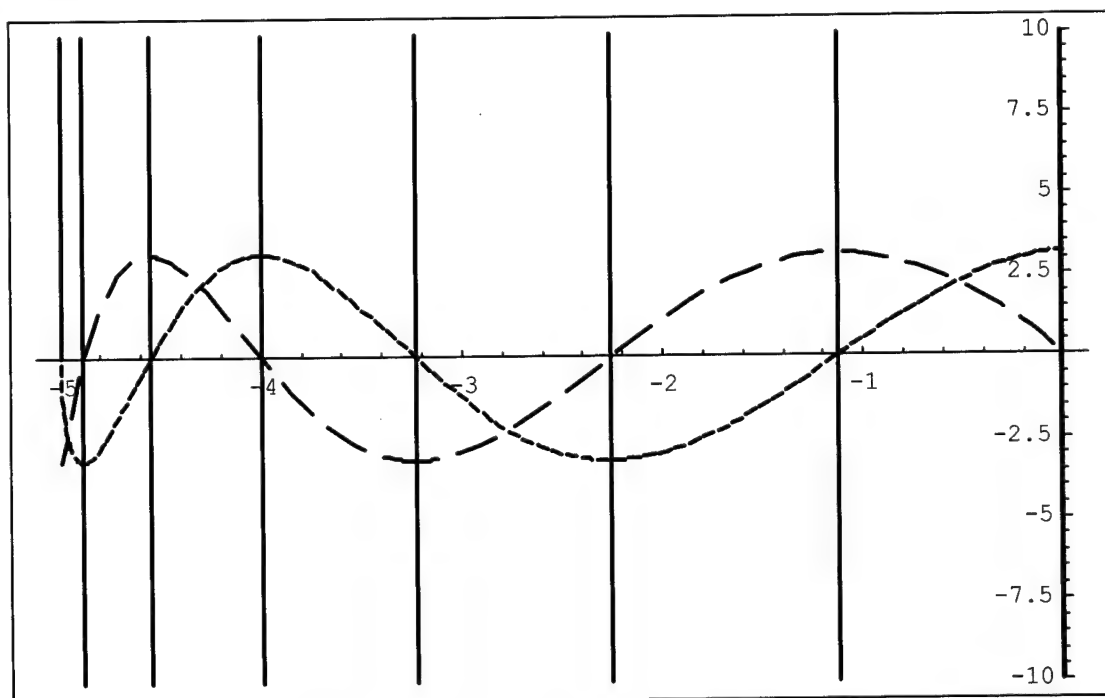


Fig A.3. Plot of the determinant of \mathbf{M} for the unsimplified and simplified cases. The vertical lines represent the unsimplified case (magnified by 1014) and the sinusoidal plots are the even and odd symmetry cases of the simplified matrix. Again the well depth is 5 au and the width is 3 au.

The energy levels of the bound states are thus found rather simply and the bound state eigenfunctions can be reconstructed by solving the eqn. A.7 for the constants A, C, D, and F. Enough information is contained within the constraints levied to determine all of the constants in terms of a single constant of our choosing. The constraint required to determine the value of this last constant is the normalization condition of eqn (A.12).

$$\begin{aligned} \int_{-\infty}^{\infty} \Psi^* \Psi dZ &= 1 \\ \int_{-\infty}^{-a} B\Psi_1^* B\Psi_1 dZ + \int_{-a}^a B\Psi_2^* B\Psi_2 dZ + \int_a^{\infty} B\Psi_3^* B\Psi_3 dZ &= 1 \quad (\text{A.12}) \\ B^2 &= \frac{1}{\int_{-\infty}^{-a} \Psi_1^* \Psi_1 dZ + \int_{-a}^a \Psi_2^* \Psi_2 dZ + \int_a^{\infty} \Psi_3^* \Psi_3 dZ} \end{aligned}$$

Given these constants, the wavefunctions are easily reconstructed and are shown in fig. A.5 for a well of depth 2 au, and a width of 1 au. Fig A.4 shows the plots of the determinant of **M** versus energy for the same case.

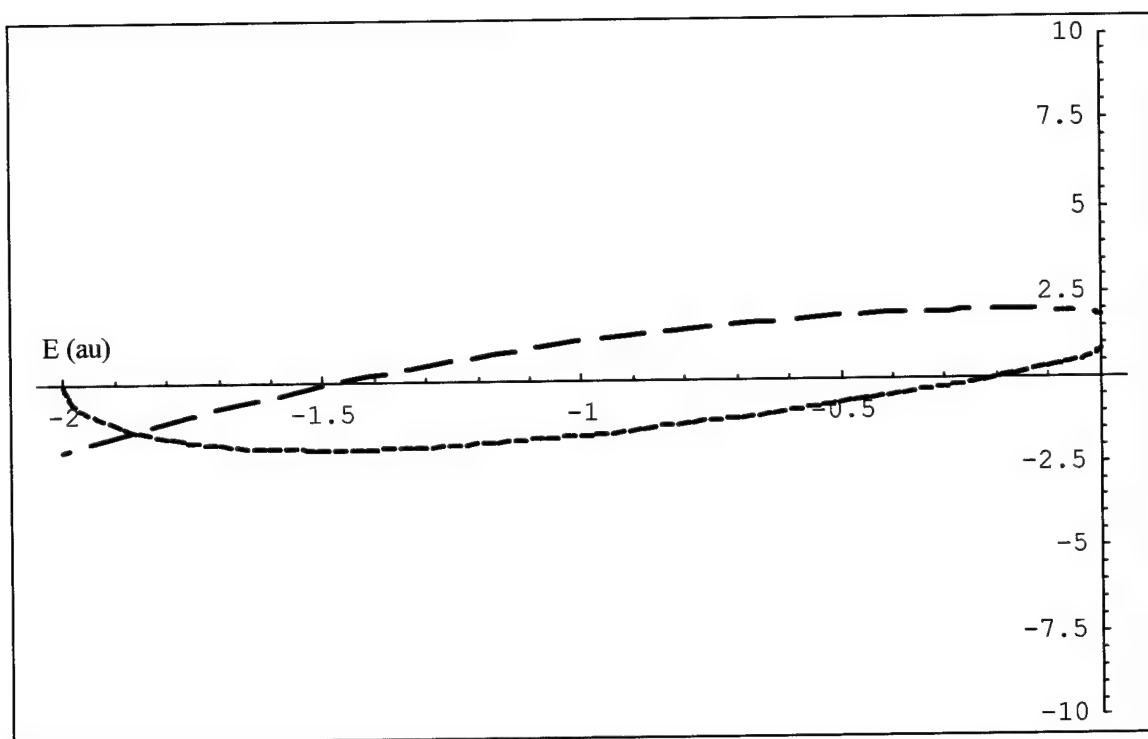


Fig. A.4. Plot of the $\det(\mathbf{M})$ for the case of a square well of depth 2 au and width 1 au. One even and one odd state is shown, at energies of approximately -1.47 au and -0.20 au respectively.

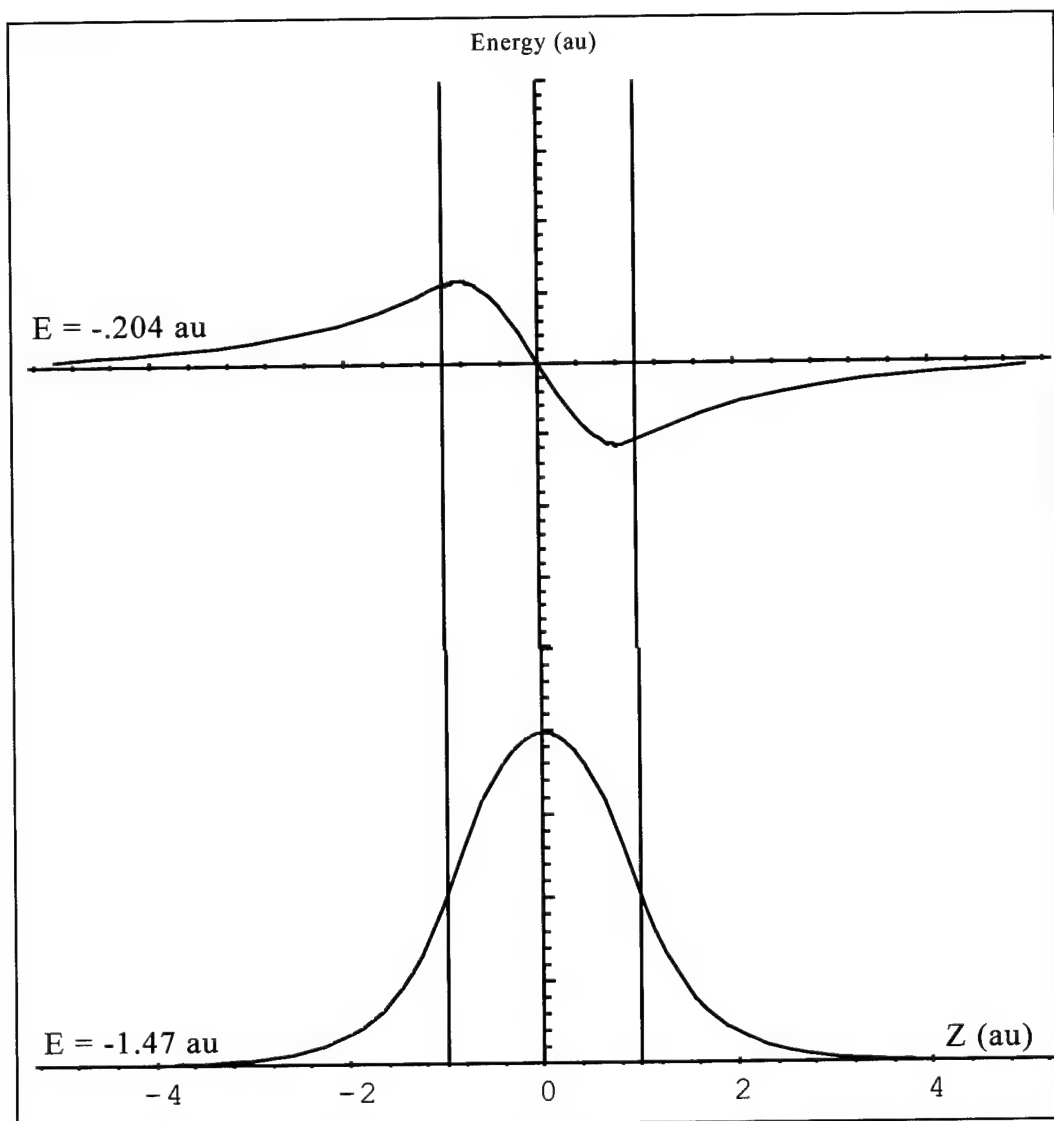


Fig A.5. Bound state wave functions for a well of depth 2 au and width 2 au.

Appendix B: Coordinate Systems

There are two important coordinate systems that will be defined in order to describe the MQW problem: the coordinate system describing the growth of the quantum well, and the coordinate system used to describe the MQWs interaction with electromagnetic radiation.

The growth direction of the MQW structure and the corresponding coordinate axes are shown in figure B-1.

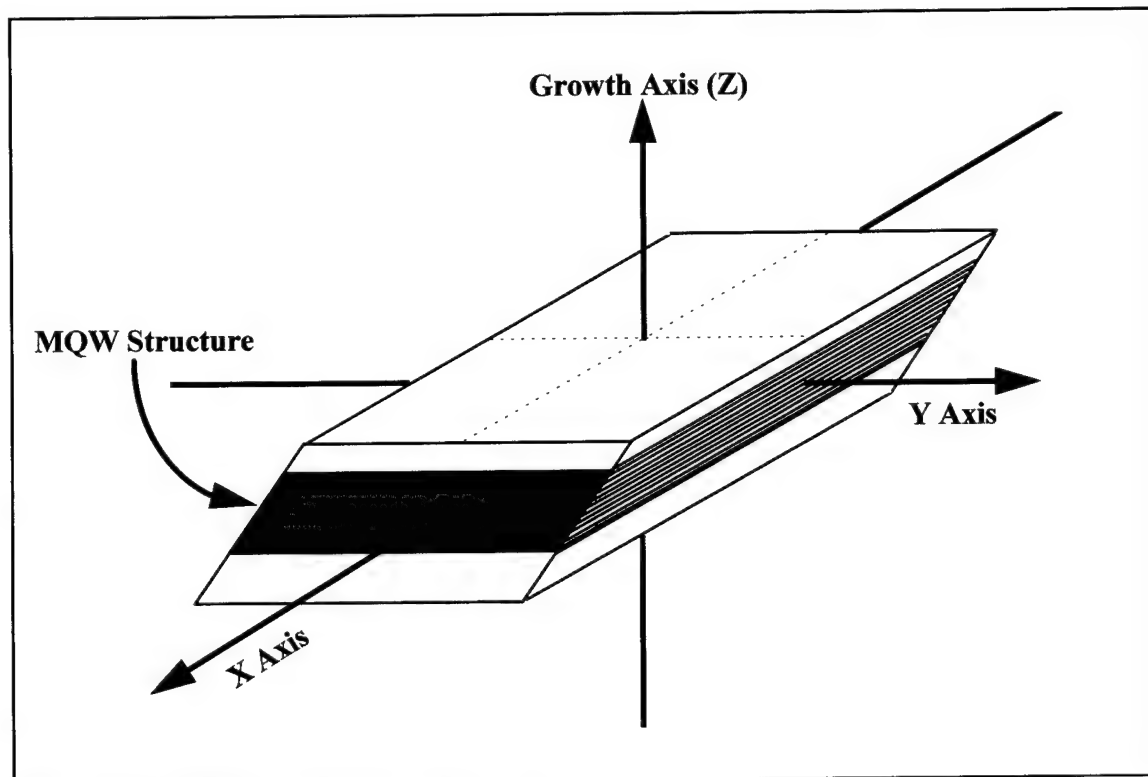


Figure B-1. MQW coordinate axes.

A discussion of the interaction of electromagnetic radiation with the MQW structure requires a definition of normal and parallel incidence. The normal incidence case means that the polarization vector of the radiation is normal to the plane of

incidence, and for the parallel incidence the polarization vector lies within the plane of incidence. These definitions will require that for normal incidence the polarization vector will lie completely within the x-y plane of the wells, and for parallel incidence the polarization vector will have a component in the z direction relative to the well in addition to a component in the x-y plane. In both cases the plane of incidence is defined as the plane containing the \mathbf{k} vector of the radiation and the vector normal to the incident surface. These two cases are shown in figures B-2 and B-3.

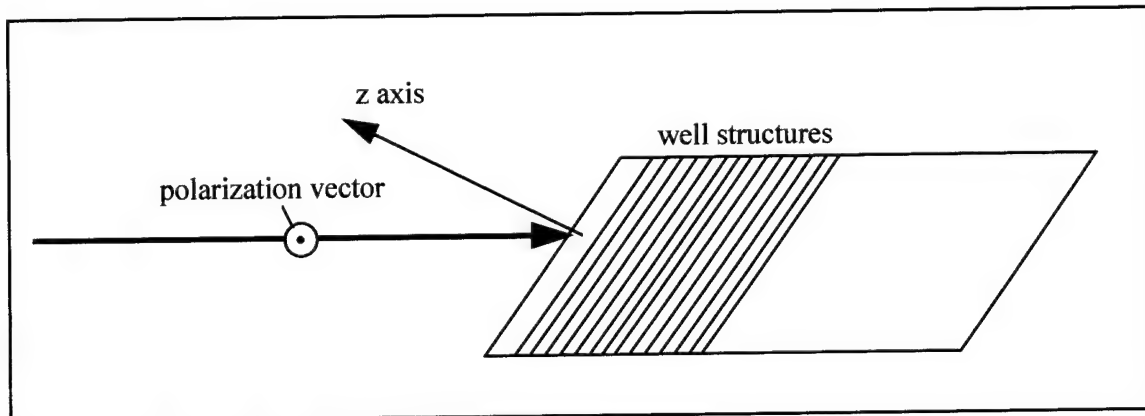


Figure B-2. Normal Incidence.

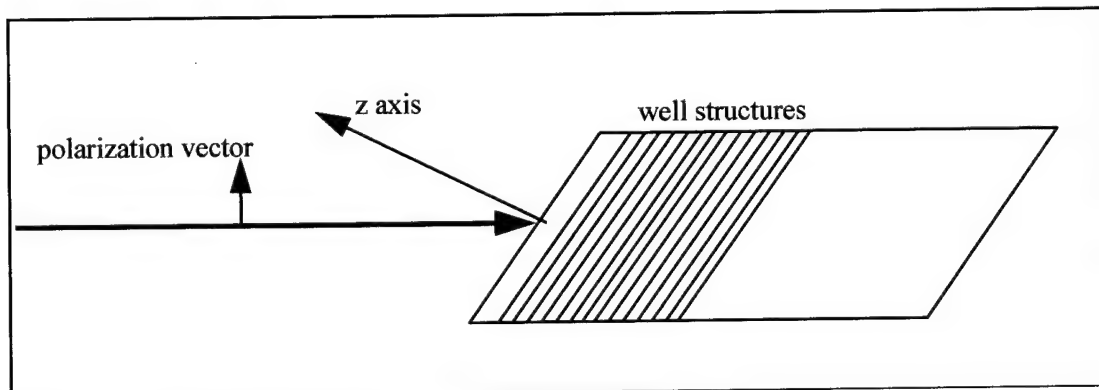


Figure B-3. Parallel Incidence.

Bibliography

1. Rogalski, Antoni. "New trends in semiconductor infrared detectors," Optical Engineering, 33, 1395 (May 1994).
2. Chang, Yia-Chung and R.B. James. "Saturation of intersubband transitions in *p*-type semiconductor quantum wells," Phys Rev B, 39, 12672 (June 1989).
3. Szmulowicz, Frank and Gail Brown. "Calculation and photoresponse measurements of the bound-to-continuum infrared absorption in *p*-type GaAs/Al_xGa_{1-x}As quantum wells," Phys. Rev. B, 51, 13203 (May 1995).
4. Kittel, Charles. Introduction to Solid State Physics. New York: John Wiley and Sons, Inc., 1966. pp 316-317.
5. Kittel, Charles. Introduction to Solid State Physics. New York: John Wiley and Sons, Inc., 1966. pg 303.
6. Walker, William, Josef Parrington, and Frank Feiner. Nuclides and Isotopes: Fourteenth Edition. San Jose, CA: General Electric Company, 1989. pp 16-17.
7. Ma, Q.M., K.L. Wang, and J.N. Schulman. "Band structure and symmetry analysis of coherently grown Si_{1-x}Ge_x alloys on oriented substrates," Phys Rev B, 47, 1936 (January 1993).
8. McKelvey, John. Solid State Physics for Engineering and Materials Science. Malabar, FL: Krieger Publishing Company, 1993. pg 25.
9. Kittel, Charles. Introduction to Solid State Physics. New York: John Wiley and Sons, Inc., 1966. pp 302-308.
10. Gregg, Micheal. Optical Detection Properties of Silicon-Germanium Quantum Well Structures. Air Force Institute of Technology (AU), Wright-Patterson AFB, OH, September 1996. pg 2-16.
11. Infrared Information and Analysis Center. The Infrared Handbook. Ann Arbor, MI: Environmental Research Institute of Michigan for the Office of Naval Research, Washington D.C., 1989. pg 11-20.
12. Rogalski, Antoni. "Semiconductor Infrared Detectors," Optical Engineering, 33, 1392, (May 1994).
13. Infrared Information and Analysis Center. The Infrared Handbook. Ann Arbor, MI: Environmental Research Institute of Michigan for the Office of Naval Research, Washington D.C., 1989. pg 11-88.

14. Kittel, Charles. Introduction to Solid State Physics. New York: John Wiley and Sons, Inc., 1966. pg 312.
15. Gregg, Micheal. Optical Detection Properties of Silicon-Germanium Quantum Well Structures. Air Force Institute of Technology (AU), Wright-Patterson AFB, OH, September 1996. pg 2-4.
16. Shepherd, Freeman. "Infrared internal emission detectors," SPIE Vol 1735, 250 (1992).
17. Saleh, Bahaa and Malvin Teich. Fundamentals of Photonics. New York: John Wiley and Sons, Inc., 1991. pg 572.
18. Tsang, W.T. "Quantum Confinement Heterostructure Semiconductor Lasers," in Semiconductors and Semimetals, Vol 24. Ed. Raymond Dingle. New York: Academic Press, 1987.
19. People, R., J.C. Bean, C. Bethea, and L. Peticolas. "Broadband (8-14 μm), normal incidence, pseudomorphic $\text{Ge}_x\text{Si}_{1-x}/\text{Si}$ strained-layer infrared photodetector operating between 20 and 77 K," Appl Phys Lett, 61, 1122 (August 1992).
20. Gregg, Micheal. Optical Detection Properties of Silicon-Germanium Quantum Well Structures. Air Force Institute of Technology (AU), Wright-Patterson AFB, OH, September 1996.
21. Luttinger, J.M. and W. Kohn. "Motion of Electrons and Holes in Perturbed Periodic Fields," Phys. Rev. 97, 869 (October 1954).
22. Luttinger, J.M. "Quantum Theory of Cyclotron Resonance in Semiconductors: General Theory," Phys Rev, 102, 1030 (May 1956).
23. Hasegawa, Hiroshi. "Theory of Cyclotron Resonance in Strained Silicon Crystals," Phys. Rev. 129, 1029 (February 1963).
24. Hensel, J.C. and G. Fehrer. "Cyclotron Resonance Experiments in Uniaxially Stressed Silicon: Valence Band Inverse Mass Parameters and Deformation Potentials," Phys Rev, 129, 1041 (February 1963).
25. Phillips, James. "Energy-Band Interpolation Scheme Based on a Pseudopotential," Phys Rev, 112, 685 (November 1958).
26. Kleiner, W.H. and L.M. Roth. "Deformation Potential in Germanium from Optical Absorption Lines for Exciton Formation," Phys Rev Lett, 2, 334 (April 1959).

27. Bandara, K., D.D. Coon, and Byungsung O. "Exchange interactions in quantum well subbands," Appl Phys Lett, **53**, 1931 (November 1988).
28. Coon, D.D. and R. Karunasiri. "New mode of IR detection using quantum wells," Appl Phys Lett, **45**, 649 (September 1984).
29. Kahan, A. , M. Chi, and L. Friedman. "Infrared transitions in strained-layer $\text{Ge}_x\text{Si}_{1-x}/\text{Si}$," J Appl Phys, **75**, 8012 (June 1994).
30. Liou, Tsyr-Shyang, Tahui Wang, and Chun-Yen Chang. "Calculation of the structural dependence of infrared absorption in p-type strained layer SiGe/Si quantum wells," J. Appl. Phys. **77**, 6646 (June 1995).
31. Bransden, B.H. and C.J. Joachain. Physics of atoms and molecules. New York: Longman, 1984. pp 155-162.
32. Bastard, Gerald. Wave Mechanics Applied to Semiconductor Heterostructures. New York: Halstead, 1988.

REPORT DOCUMENTATION PAGE			Form Approved OMB No. 0704-0188	
Public reporting burden for this collection of information is estimated to average 1 hour per response, including the time for reviewing instructions, searching existing data sources, gathering and maintaining the data needed, and completing and reviewing the collection of information. Send comments regarding this burden estimate or any other aspect of this collection of information, including suggestions for reducing this burden, to Washington Headquarters Services, Directorate for Information Operations and Reports, 1215 Jefferson Davis Highway, Suite 1204, Arlington, VA 22202-4302, and to the Office of Management and Budget, Paperwork Reduction Project (0704-0188), Washington, DC 20503.				
1. AGENCY USE ONLY (Leave blank)	2. REPORT DATE December 1996	3. REPORT TYPE AND DATES COVERED Masters Thesis		
4. TITLE AND SUBTITLE Theoretical Modeling of Linear Absorption Coefficients in Si/Si _{1-x} Ge _x Multiple Quantum Well Photodetectors			5. FUNDING NUMBERS	
6. AUTHOR(S) Kevin D. Greene, Capt, USAF				
7. PERFORMING ORGANIZATION NAME(S) AND ADDRESS(ES) Air Force Institute of Technology, WPAFB OH 45433-6583			8. PERFORMING ORGANIZATION REPORT NUMBER	
9. SPONSORING/MONITORING AGENCY NAME(S) AND ADDRESS(ES) Rome Laboratory Mr. Paul Pellegrini (RL/ERE) 25 Electronic Pkwy Griffiss AFB NY 13441-4515			10. SPONSORING/MONITORING AGENCY REPORT NUMBER	
11. SUPPLEMENTARY NOTES				
12a. DISTRIBUTION/AVAILABILITY STATEMENT Approved for public release; distribution unlimited			12b. DISTRIBUTION CODE	
13. ABSTRACT (Maximum 200 words) Si/Si _{1-x} Ge _x MQW Infrared Photodetectors offer the promise of normal incidence photodetection tunable over the range of 3-12 μ m wavelength range at temperatures above 40 K. This system is attractive because the Si _{1-x} Ge _x offers greater compatibility with existing Si based signal processing circuitry. Band structures, momentum matrix elements and linear absorption coefficients are computed using a Luttinger-Kohn k•p analysis for Si/ Si _{1-x} Ge _x quantum wells grown in the [110] direction. The absorption coefficient as a function of energy and wavelength is calculated by two methods: a delta function fit to intersubband transitions, and a Lorentzian fit to intersubband transitions. Calculations were performed for parallel as well as normally incident radiation and the resulting absorption spectra are in good agreement with experimental observations.				
14. SUBJECT TERMS Si/Si _{1-x} Ge _x , the linear absorption coefficients, infrared photodetectors, multiple quantum wells			15. NUMBER OF PAGES 118	
			16. PRICE CODE	
17. SECURITY CLASSIFICATION OF REPORT Unclassified	18. SECURITY CLASSIFICATION OF THIS PAGE Unclassified	19. SECURITY CLASSIFICATION OF ABSTRACT Unclassified	20. LIMITATION OF ABSTRACT UL	

GENERAL INSTRUCTIONS FOR COMPLETING SF 298

The Report Documentation Page (RDP) is used in announcing and cataloging reports. It is important that this information be consistent with the rest of the report, particularly the cover and title page. Instructions for filling in each block of the form follow. It is important to *stay within the lines* to meet *optical scanning requirements*.

Block 1. Agency Use Only (Leave blank).

Block 2. Report Date. Full publication date including day, month, and year, if available (e.g. 1 Jan 88). Must cite at least the year.

Block 3. Type of Report and Dates Covered. State whether report is interim, final, etc. If applicable, enter inclusive report dates (e.g. 10 Jun 87 - 30 Jun 88).

Block 4. Title and Subtitle. A title is taken from the part of the report that provides the most meaningful and complete information. When a report is prepared in more than one volume, repeat the primary title, add volume number, and include subtitle for the specific volume. On classified documents enter the title classification in parentheses.

Block 5. Funding Numbers. To include contract and grant numbers; may include program element number(s), project number(s), task number(s), and work unit number(s). Use the following labels:

C - Contract	PR - Project
G - Grant	TA - Task
PE - Program Element	WU - Work Unit Accession No.

Block 6. Author(s). Name(s) of person(s) responsible for writing the report, performing the research, or credited with the content of the report. If editor or compiler, this should follow the name(s).

Block 7. Performing Organization Name(s) and Address(es). Self-explanatory.

Block 8. Performing Organization Report Number. Enter the unique alphanumeric report number(s) assigned by the organization performing the report.

Block 9. Sponsoring/Monitoring Agency Name(s) and Address(es). Self-explanatory.

Block 10. Sponsoring/Monitoring Agency Report Number. (If known)

Block 11. Supplementary Notes. Enter information not included elsewhere such as: Prepared in cooperation with...; Trans. of...; To be published in.... When a report is revised, include a statement whether the new report supersedes or supplements the older report.

Block 12a. Distribution/Availability Statement. Denotes public availability or limitations. Cite any availability to the public. Enter additional limitations or special markings in all capitals (e.g. NOFORN, REL, ITAR).

DOD - See DoDD 5230.24, "Distribution Statements on Technical Documents."

DOE - See authorities.

NASA - See Handbook NHB 2200.2.

NTIS - Leave blank.

Block 12b. Distribution Code.

DOD - Leave blank.

DOE - Enter DOE distribution categories from the Standard Distribution for Unclassified Scientific and Technical Reports.

NASA - Leave blank.

NTIS - Leave blank.

Block 13. Abstract. Include a brief (*Maximum 200 words*) factual summary of the most significant information contained in the report.

Block 14. Subject Terms. Keywords or phrases identifying major subjects in the report.

Block 15. Number of Pages. Enter the total number of pages.

Block 16. Price Code. Enter appropriate price code (*NTIS only*).

Blocks 17. - 19. Security Classifications. Self-explanatory. Enter U.S. Security Classification in accordance with U.S. Security Regulations (i.e., UNCLASSIFIED). If form contains classified information, stamp classification on the top and bottom of the page.

Block 20. Limitation of Abstract. This block must be completed to assign a limitation to the abstract. Enter either UL (unlimited) or SAR (same as report). An entry in this block is necessary if the abstract is to be limited. If blank, the abstract is assumed to be unlimited.